Characterisation of Textured Insulators for Overhead Lines and Substations

By

Panagiotis Charalampidis

A thesis submitted to Cardiff University

in candidature for the degree of

DOCTOR OF PHILOSOPHY

High Voltage Energy Systems Group (HIVES)

School of Engineering

Cardiff University

2012

DECLARATION

This work has not previously been accepted in substance for any degree and is not being concurrently submitted in candidature for any degree.

Signed ..... (candidate)

Date .....

STATEMENT 1

This thesis is being submitted in partial fulfillment of the requirements for the degree of PhD.

Signed …….. (candidate)

Date ……..

STATEMENT 2

This thesis is the result of my own investigations, except where otherwise stated. Other sources are acknowledged by footnotes giving explicit references. A bibliography is appended.

Signed ..... (candidate)

Date .....

STATEMENT 3

I hereby give consent for my thesis, if accepted, to be available for photocopying and for inter-library loan, and for the title and summary to be made available to outside organisations.

Signed ..... (candidate)

Date .....

Acknowledgements

I would like to express my gratitude to my supervisors Prof. A. Haddad and Dr. H. Griffiths for their guidance, support and invaluable advice throughout this research project. Deepest gratitude is also due to Emeritus Professor R.T. Waters, without whose extensive knowledge and experience and constant guidance, this study would not have been successful.

I would like to thank Dr. N. Harid, Dr. P. Sarkar and Dr. M. Albano for their assistance and contributing work to this research project and the Engineering and Physical Sciences Research Council (EPSRC) for the financial support.

Many thanks go to all my colleagues and staff at the High Voltage Laboratory for their help and co-operation during the laboratory experiments. In particular, I would like to thank Mr. A. Nekeb and Mr. J. Snow for their encouragement and friendship.

I would also like to thank the technicians and administrative staff of Cardiff School of Engineering for their assistance and support. In particular I would like to convey special thanks to Mr. P. Faruggia and Mr. S. P. Mead for their precious assistance in building, modifying and maintaining experimental apparatus for this research project.

I would like to express my love and gratitude to my family and friends for their support and to my partner for her encouragement and understanding through the duration of this work.

Summary

Pollution flashover constitutes the predominant parameter for the design, specification and dimensioning of high voltage outdoor insulation [1-2]. For over a quarter of a century, polymeric insulators have been used for overhead lines and substations due to their enhanced performance in highly polluted environments. This is mainly attributed to the hydrophobic properties of polymeric surfaces that lead to a reduction of surface wetting and, thus, to a reduction of leakage current and discharge activity that could result to a flashover. However, under severe ambient conditions, discharge activity is not totally eliminated

The present investigations have demonstrated the development of dry bands and partial arcs on polymeric insulators (Chapter 3). While 'cap and pin' ceramic insulators - e.g. porcelain and glass - employ special anti-fog designs of increased leakage path introduced by the presence of deeper ribs, such profiles cannot be used for polymeric insulators due to moulding restrictions [1-1]. Yet, these moulding properties allow the fine texturing of the polymeric surface [1-7]. Textured insulators are a novel approach for the improvement of polymeric insulators using a surface design consisting of an array of hemispherical protuberances of various configurations and range of diameters. The objective is to reduce power dissipation ($P = EJ$) on the insulator surface by reducing the electric field gradient E and current density J (Chapter 2). Moreover, an increase of the longitudinal creepage path can be achieved without the need of increasing the overall length of the insulator. Where discharges do occur, the formation of parallel current paths could lead to less harmful discharges hence mitigating damage due to thermal stresses.

An initial theoretical classification of the textured designs resulted to a shortlist of textured patterns that could be employed for the development of a full insulator prototype. At the next stage, these patterns were experimentally evaluated in a series of material tests in accordance to IEC-60587 inclined-plane test procedure [Chapter 5]. Rectangular silicone rubber samples with a plane surface were tested along with samples with a textured finish to assess the performance against erosion and tracking. The improvement introduced by these textured patterns in comparison with conventional non-textured samples was outstanding [2-48, 49]. The intersecting square pattern showed the best performance, hence it was chosen for the development of a full textured insulator.

Conventional 11 kV silicone rubber insulators and textured insulators with the same shed profile were cast in-house using vacuum injection casting techniques. There are no international standards for the artificial testing of polymeric insulators. In this work, a proposed test procedure for non-ceramic insulators is described (Chapter 3). Clean-fog tests of conventional (Chapter 4) and textured insulators (Chapter 6), for a range of wetting and pollution severity conditions, showed that textured insulators showed an improved flashover performance that in some cases reached 26 %. Surface texturing seems to be more effective under severe conditions of wetting and pollution and when hydrophobicity is reduced, like the temporary loss of hydrophobicity observed for silicone rubber insulators in service.

Publications - Awards

Publications

Haddad, A., Waters, R., Griffiths, H., Chrzan, K., Harid, N., Sarkar, P., and Charalampidis, P., 'A new approach to anti-fog design for polymeric insulators', IEEE Trans. Dielectr. Electr. Insul., Vol. 17, (2): pp. 343-350, 2010

Sarkar, P., Haddad, A., Waters, R.T., Griffiths, H., Harid, N., and Charalampidis, P., 'Inclined-plane tests of textured silicone rubber Samples', International Conference on High Voltage Engineering and Application (ICHVE), pp. 532-535, New Orleans, U.S.A., 2010

Charalampidis, P., Haddad, A., Waters, R.T., Griffiths, H., Harid, N., and Sarkar, P., 'Five-electrode inclined-plane tests of textured silicone rubber samples', 45th Universities Power Engineering Conference (UPEC), pp. 1-5, Cardiff, UK, 2010

Charalampidis, P., Albano, M., Waters, R.T., Haddad, A., Griffiths, H., and Harid, N., 'Dry-band discharges on silicone rubber insulation', XVII International Conference on High Voltage Engineering (ISH), Hannover, Germany, 2011

Charalampidis, P., Waters, R.T., Haddad, A., Griffiths, H., Harid, N., and Sarkar, P., *Material tests for textured silicone rubber samples*. XVII International Conference on High Voltage Engineering (ISH), Hannover, Germany, 2011.

Waters, R.T., Haddad, A., Griffiths, H., Harid, N., Charalampidis, P., and Sarkar, P., 'Dry-band discharges on polluted silicone rubber insulation: control and characterization', IEEE Trans. Dielectr. Electr. Insul., Vol:18, (6): pp. 1995-2003, 2011.

Awards

The research paper "Textured insulators for overhead lines and substations" received the 2011 John Neal Award at the European competition held by the European Electrical Insulation Manufacturers (EEIM, www.eeim.org).

Table of Contents

Chapter 3. Pollution Flashover of Silicone Rubber Insulator: Experimental Techniques and Test Protocols

Chapter 4. Laboratory classification of dry-band formation and flashover mechanism

Chapter 5. Comparative performance of insulation samples with different textures

Chapter 6. Performance of textured silicone rubber insulators under polluted conditions

Chapter 7. General Discussion – Conclusions – Future Work

Chapter 1. Introduction

1.1 Outdoor insulation: role and problems

Outdoor high voltage insulation constitutes a crucial element for the design and performance of large high voltage power systems. Due to the critical importance of a reliable and efficient power transmission, outdoor insulation has inevitably been at the epicentre of research interest in an endeavour to eliminate or alleviate the problems associated with insulation failure.

The main functions of insulators are to withstand the mechanical stress of supporting electrical conductors and to electrically isolate equipment of different potential and inhibit flashover events from occurring. Flashover performance of insulators is mostly dictated by their ability to deal with the complications introduced by the accretion of contaminants on the insulating surface.

An insulator in service is susceptible to pollution by air-borne contaminants that are deposited on the insulation surface. When this pollution layer is wet, it conducts a leakage current with a non-uniform density. Local heating at regions of high current density is accompanied by the formation of dry zones, called dry-bands. When the voltage gradient across these dry-bands reaches a critical value, they are spanned by surface discharges. The latter have a decisive impact on the insulator performance as it makes it vulnerable to degradation and to the electrical bridging of the energised conductors in the form of a hot flashover arc [1.1].

Two main categories of insulators have been employed for overhead lines (OHL) and substations depending on the material used: Ceramic and polymeric insulators. Ceramic insulators have been in service since the early 20th century with an excellent service record. The mechanisms leading to a pollution flashover event are fairly understood. However, over the last 30 years, polymeric materials have gained extensive acceptance, mainly due to their superior

performance at severe ambient conditions compared with their ceramic counterparts.

The key advantage of polymeric insulators is the hydrophobicity of the insulating surface. This water repellent property forces water to be deposited in a form of discrete beads unlike the hydrophilic case for ceramics, which form a thin spread layer on their surface. The reduction of surface wetting consequently leads to a reduction of discharge activity on polymeric surfaces and to an enhanced anti-pollution performance.

Silicone rubber is a polymer widely adopted for outdoor insulation. Unlike other polymers, like EPDM (ethylene propylene diene monomer), it retains its hydrophobic status throughout service life and, in addition, has the ability to transfer this hydrophobicity to the adhering pollutants. However, like all polymers, it is vulnerable to long-term degradation due to aging and weathering.

Pollution flashover constitutes the predominant parameter for the design, specification and dimensioning of high voltage insulators [1.2]. An extensive review work by CIGRE [1.3,1.4] , adapted by the recently revised international standard [1.5] , overturned the traditional approach where the shortest distance between the insulation terminals, called creepage distance, determined the selection process for polluted environments. It is now accepted that other factors strongly influence the pollution performance as well. These are related to the electrical system requirements, the type of environment and pollution, and the insulator design.

There are two types of pollution [1.5]:

- *Type A*: this solid layer pollution consists of a soluble and non-soluble component that is deposited on the insulator surface. Under conditions of slow humidification (dew, drizzle, mist, fog etc.), this layer becomes conductive. This type of pollution is mostly associated with inland, industrial and desert areas. The non-soluble component acts as a binder between the soluble component and the insulator surface, and for polymeric insulators, it masks the hydrophobic layer. The soluble component consists of low and high solubility salts.

- *Type B*: this type has no or little non-soluble component and comes in the form of salt spray of conductive fog. It simulates the pollution found at coastal areas. Within this category, crop sprays at agricultural areas, acid rain and chemical mists are included.

The IEC-60507 [1.6] recommends tests to simulate the conditions of pollution that insulators are subjected to in the field. These tests are:

a. The Salt-Fog method: the insulator is subjected to fog produced by a salt (NaCl) solution. This test best simulates contamination by pollution type B.
b. The Solid-Layer method: also referred as Clean-Fog method, this procedure suggests the direct application of solid pollution on the insulator surface and represents best pollution type A.

The IEC 60507 standard is specifically concerned for ceramic insulators. Its applicability to polymeric insulators is limited. Due to the dynamic nature of the polymeric material and its wetting properties, it has been difficult to establish a commonly accepted method. One of the approaches followed is the use of existing methods employed for the testing of ceramic insulators [1.6] or modified versions of these conventional methods [1.4].

1.2 Textured Insulators and scope of research work

The hydrophobic surface of polymeric insulators offers a significant advantage compared with glass or ceramic units used in overhead transmission and distribution systems in coastal or industrial environments. However, under severe ambient conditions, dry band formation is not totally eliminated, especially before hydrophobic recovery can occur in the overlaying pollution layer.

A critical region is the recessed area below the shed of the insulator, where washing is least effective and deposits may accumulate. The geometry of the insulator shows that the density of surface discharge currents flowing from one end of the insulator to the other is highest at the shank of the insulator. As a consequence, the surface electric field strength is also at a maximum in this

region, and there is a heightened risk of surface heating, which may cause dry bands, partial arcs on the surface and consequential thermal damage. This action is limited in the case of glass and ceramic cap and pin insulators by 'anti-fog' designs having additional rims on the underside of the sheds which lengthen the creepage distance and reduce the magnitude of the leakage current [1.7]. However, because of the nature of the moulding process, this is not possible in multi-shed polymeric insulators. A patented design programme aims to deal with these challenges and improve the pollution properties of a silicone rubber surface by employing a textured finish [1.8].

Textured patterns consist of intersecting or contiguous hemispherical protuberances [1.9]. This raised geometry does not impede the removal of the insulator from the mould during casting. The main aim of surface texturing is to lower power dissipation on the insulator surface by reducing both leakage current density and the electric field gradient. An increase of surface area can reduce the leakage current density in the vulnerable shank region, and a substantial increase in the longitudinal creepage distance could reduce the electric field stress. Moreover, the texture pattern can have paths of preferential contamination and conduction, which can lead to several parallel current paths.

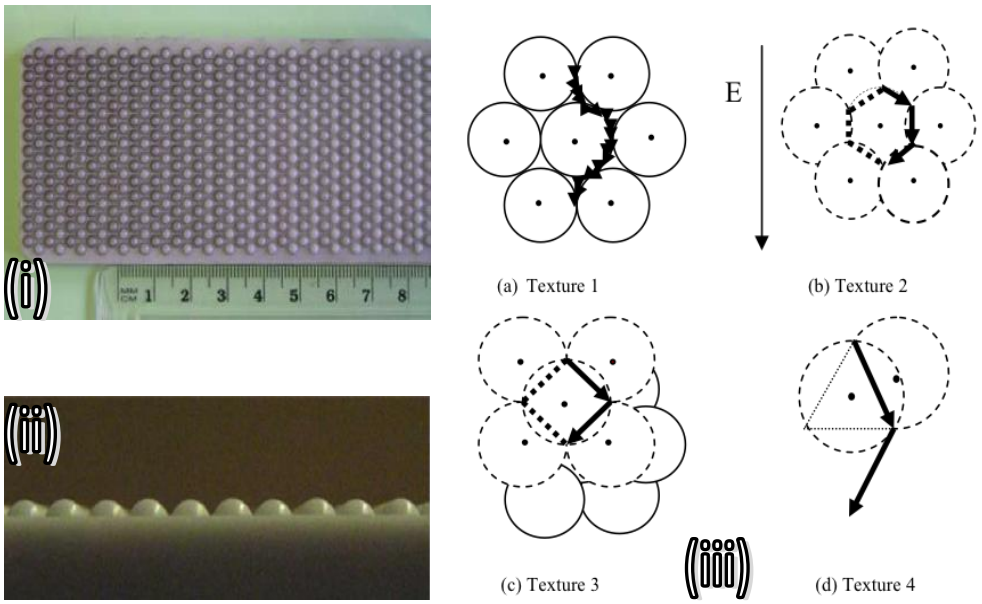

Figure 1-1: Example of texturing, i) top view ii) side view iii) texture designs [1.8]

As soon as a path is conducting, the resulting heat and drying will increase the resistance of that path. Nevertheless, an adjacent current path of higher conductance will be available, thus switching the conduction path from the original path before the insulation surface sustains thermal damage.

This design concept aspires to reduce tracking and erosion on the insulator surface and to improve the flashover strength under conditions of heavy pollution. This research programme set out to complete a series of laboratory investigations to assess the performance of such textures and to investigate the predicted advantages introduced compared with conventional silicone rubber insulation.

1.3 Aims of research work

The research programme was diverse with tasks ranging from insulation design and vacuum injection casting to high voltage testing and software programming. The main aims of this research work are as follows:

(a) To prove the effectiveness of textured surfaces in reducing the thermal damage on silicone rubber insulation due to surface heating induced by surface discharges.

(b) To identify and demonstrate the optimum textured designs that show the maximum reduction of surface erosion and that could be employed for the development of a full shedded insulator.

(c) To establish a comprehensive test procedure for the testing of full silicone rubber insulators in clean-fog that would incorporate ancillary current measurements and infrared photography. Include the testing of conventional silicone rubber insulators to investigate their pre-flashover behaviour and the possible formation of dry-bands during artificial pollution testing.

(d) To design and manufacture full textured silicone rubber insulators that would employ the textured patterns explored in step (b)

(e) To test and assess the flashover performance of textured silicone rubber insulators prototypes in clean-fog tests and compare with the

performance of conventional insulators of the same profile and material but with a smooth surface.

(f) To develop a high-resolution data acquisition system that would monitor the test voltage and leakage current and also store these data into files for post-processing analysis. For the inclined-plane programme, the software would need to control the accelerated ageing unit.

1.4 Thesis outline

In the present work, a test procedure based on the Solid-Layer method has been developed for the testing of full insulator prototypes. Conventional silicone rubber (SiR) insulators were developed in-house, using vacuum injection casting techniques. These composite insulators consist of a silicone rubber housing made of commercially available silicones and moulded over a reinforced glassfibre core. Full insulator prototypes of the same dimensions and material like the conventional, but employing fine texturing, were also manufactured and tested. The test results showed a substantial improvement of the flashover voltage for some textured prototypes compared with the conventional, smooth-surface design. Ancillary measurements and photography at the visual and infrared spectrum provided a comprehensive insight on the phenomena and mechanisms surrounding dry-band pollution flashover for silicone rubber insulation.

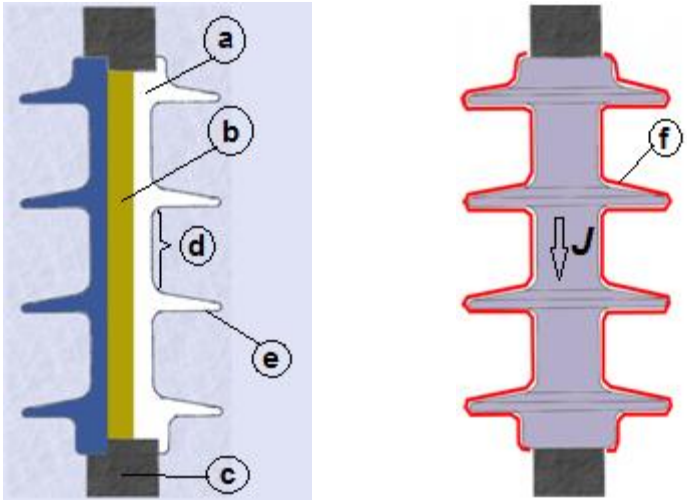

Figure 1-2. The composite insulator (a) housing (b) reinforced glass fibre core (c) metal fittings (d) shank section (e) shed (f) pollution layer on the insulator surface conducting a leakage current of density J.

Materials assigned for the manufacturing of high voltage outdoor insulation should be assessed for their ability to prevent erosion and tracking. The gradual degradation of the insulation surface to form conductive paths called tracks or the loss of insulation material due to leakage current or surface discharging is most unwanted for outdoor insulators. Extensive tracking and erosion severely undermines the insulating effectiveness and the mechanical robustness when eroded rubber exposes the fibreglass core to partial discharge attack.

Silicone rubber for composite insulators includes special flame retardant fillers to increase the resistance against erosion and tracking by absorbing heat from surface discharges and releasing water vapor.

The inclined-plane test (IPT) is a well-established material test for the assessment of the resistance of insulating materials against erosion and tracking and is described in the IEC 60587 international standard [1.10]. Rectangular standard size samples are mounted at a 45^{o} angle and subjected to high voltage stress. A salt contaminant solution is fed from the top of the sample and traverses the test surface. The test is designed to encourage the formation of dry-bands and surface discharges in order to monitor surface erosion and tracking.

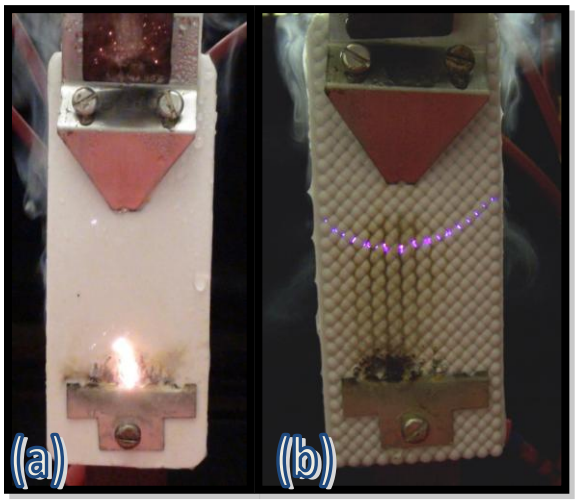

Figure 1-3: Examples of silicone rubber samples during an inclined-plane test: (a) conventional plain surface sample and (b) sample with fine surface texturing.

For the purpose of this project, rectangular silicone rubber samples were prepared with dimensions as per the standard (120mm x 50mm x 6mm). Samples with a plain surface and samples employing fine texturing were tested to compare the performance against surface erosion and tracking. Infrared recordings and, in some cases, high-speed photography provided useful information for the interpretation of the test results.

Textured samples showed significantly different discharge behaviour, which is accounted for the substantial improvement introduced by these textures in terms of resistance against erosion and tracking, compared with conventional samples.

For both the clean-fog tests and the inclined-plane tests, dedicated data acquisition programmes were developed based on the National Instruments LabVIEW platform. These high-resolution programmes monitored and stored in files the waveforms of voltage and current. In the case of the data acquisition system built for the inclined-plane tests, the software also performed the automated digital operation of the accelerated ageing unit to comply with the requirements and guidelines of the relevant international standard.

The structure of this thesis is as follows:

Chapter 2 – Research background

Pollution flashover of outdoor insulators remains a tantalizing problem for researchers. The novel design for polymeric insulators described in this work is an attempt to alleviate the problems arising from the use of polymeric insulators under severe ambient conditions. In this chapter, a review of the research work on pollution flashover and flashover mechanisms for both ceramic and polymeric insulators are presented. Moreover, the research work and design principles of textured patterns that preceded this work are also described.

Chapter 3 - Pollution flashover of silicone rubber insulator: experimental techniques and test protocols

The difficulties related with the laboratory testing of polymeric insulators required for the establishment of a comprehensive test procedure for silicone

rubber insulators in clean fog are described. Moreover, the assessment of the flashover performance of textured insulators required the casting and testing of conventional silicone rubber insulators to investigate the pre-flashover mechanisms taking place in artificial pollution testing. In this chapter, the test protocols followed for the laboratory testing of silicone rubber insulators is presented along with the employment of ancillary current measurements and infrared photography. The development of the fog chamber data acquisition system and the vacuum casting techniques for the in-house manufacturing of silicone rubber insulators are also described.

Chapter 4 – Laboratory classification of dry-band formation and flashover mechanism

Conventional silicone rubber insulators made of two different silicone materials are tested according to the test procedures described in Chapter 3. The flashover performance is assessed under different conditions of pollution severity and rate of wetting from the fog in the experimental chamber. Camera recordings at the visible and infrared spectrum are also presented to reveal the pre-flashover phenomena on the insulator surface. The acquired waveforms of voltage and current are processed and correlated with the camera recordings to unfold the mechanisms leading to pollution flashover of a polymeric insulator.

Chapter 5- Comparative performance of insulation samples with different textures

The theoretical exploration of textured patterns that could be employed for the development of a full textured insulator prototype has resulted in a shortlist of candidate textures. The inclined-plane test (IPT) is a well-established IEC test to assess the resistance against erosion and tracking of insulation materials. In this chapter, the shortlist of candidate textures is presented. In accordance with the IEC guidelines, rectangular silicone rubber samples were manufactured: conventional plain-surface samples and samples made of the same material but with a textured finish. These samples were tested using the IPT to investigate further improvement of the performance against thermal damage introduced by textured patterns compared with the non-textured samples. The formation of a

stable dry-band along with ancillary current measurements and infrared photography provided significant information for the interpretation of the test results and the dynamics of dry-band formation in silicone rubber insulation. The test results concluded that two textured patterns could be employed for the development of full insulator prototypes.

Chapter 6 – Performance of textured silicone rubber insulators under polluted conditions

In the previous chapter, two geometrical configurations were chosen for the development of full textured prototypes. In this chapter, the design, manufacturing and testing of textured insulators are presented. The design principles are described along with the process of the vacuum casting techniques. Unlike conventional insulators that were manufactured using metal moulds, the textured prototypes were cast using silicone rubber moulds that were also built in-house. Four prototypes were built and then tested in the fog chamber following the same test protocols described in Chapter 3 for the clean-fog tests of conventional insulators. Estimations of the flashover performance of each design were performed and compared with the flashover performance of conventional insulators.

The main contributions of the present work could be summarized:

- The effectiveness of textured designs was demonstrated.
- The optimum texture for the development of full textured insulators was identified in a series of IEC-60587 inclined-plane tests.
- A test procedure for the testing of polymeric insulators that would include ancillary measurements of pre-flashover phenomena was established.
- Full textured insulators were designed and manufactured in-house.
- Comparison clean-fog tests between conventional insulators and textured insulators were performed showing that textured prototypes can increase the flashover voltage up to 26%.
- A high resolution data acquisition system and data analysis programme were developed for acquiring and processing test data.

Chapter 2. Research background

Introduction

The energy sector is facing multiple challenges. The retirement of old power units, the integration of systems that generate power from renewable sources, the environmental goals for reducing the carbon dioxide emissions, legislative issues in the privatised energy market are just a few examples of these concerns that will shape the future energy map. However, there are also problems that, though they have been identified since the early days of high voltage power systems, have not been resolved. The performance of outdoor high voltage insulation under conditions of environmental pollution is still a puzzling problem, even well over a century after the initial employment of the cap-and-pin ceramic insulator.

Pollution flashover of outdoor insulators still attracts the interest of many researchers worldwide and that is reflected in the large number of research papers presented in international conferences on this subject [1.2]. The use of polymeric insulators has been extensive over the last 30 years mainly for their superior flashover performance for polluted environments compared with their ceramic counterparts. However, under severe ambient conditions, surface discharge activity and pollution flashover is not totally eliminated.

Textured insulators are a patented design programme that aims to enhance the pollution performance of polymeric insulators by employing a fine textured finish on the insulator surface [1.8]. These textures consist of an array of hemispherical protuberances that are contiguous or overlap to form various configurations. Surface texturing aims to reduce power dissipation on the insulator surface by reducing both the electric field and the current density, which is highest at the insulator shank sections [1.9].

While the mechanisms leading to flashover are well documented and fairly well-understood for ceramic insulators, the pre-flashover conditions for polymeric

insulators are not fully clarified yet [1.2][2.1]. Currently, no internationally accepted method exists for the testing of polymeric insulators as the dynamic hydrophobic surface of the polymeric housing introduces various implications for the adoption of the standard tests applied for ceramic insulators [1.4].

This chapter describes previous research work on insulation pollution flashover and the commonly adopted design approaches adopted for polymeric insulators. Also, a review of the methods proposed for the laboratory testing of polymeric insulators is presented. Finally, a description of the concept and design principles of textured patterns is explained.

2.1 Insulating materials

The main insulation materials used for outdoor insulation are glazed porcelain, toughened glass and polymers. The microscopic structure of each material affects directly its mechanical and electrical properties [1.1]. While ceramic insulators have been used from the mid-19th century for telecommunication networks, the polymers started gaining wide acceptance mainly since the 1970s. The cap-and-pin design for overhead lines is the most numerous design variation of ceramic insulators [1.2]. Composite insulators, made of a polymeric housing moulded over a reinforced glass fiber core, are a common design for polymeric materials. Looms, in his extensive work on high voltage insulators [1.1], provides a very detailed description of these materials.

2.1.1 Porcelain

The fundamental materials used for the manufacturing of porcelain insulators are clay, quartz and feldspar. In the wet process, the raw materials are first blended together in water, followed by the dehydration process. The resulting moist clay is then hot pressed to shape the insulator. The insulator is then glazed to form a smooth surface finish and it is then fired at approximately 1200^{o}C in special kilns. Due to the moulding restrictions introduced by the manufacturing method, no re-entrant or undercut profiles can be produced [1.1].

Due to the strong inter-molecular electrostatic bonds between the components that form the porcelain and glass materials, insulators with high melting points are produced, that are mechanically robust and have good resistance against

chemical attack. Moreover, the surface is characterised by a high surface free energy meaning that the insulator surface can be easily wetted in the form of a thin layer [1.1].

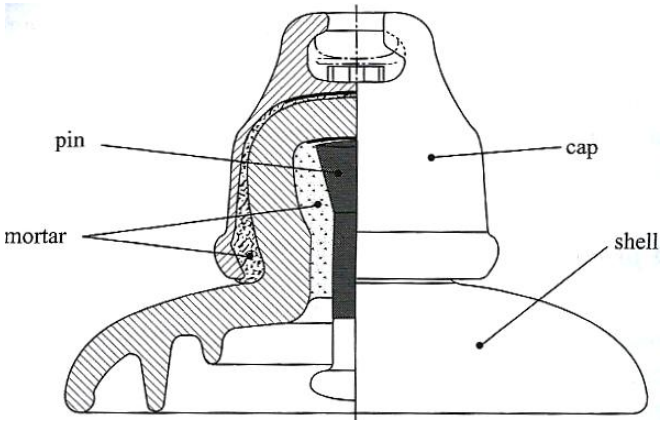

Figure 2-1. Standard cap-and-pin insulator (taken from [1.2]).

2.1.2 Glass

Silica, limestone, Dolomite, feldspar, soda ash and salt cake or sodium sulphate are mixed and melted at temperatures up to 1500°C. The molten glass is then poured in a mould to form the glass disc of the cap-and-pin insulator. After removing the disc from the mould, it is thermally toughened to enhance its mechanical properties. After a quality inspection, the flawed units are rejected and the metal fittings are attached. Toughened glass has increased mechanical properties compared with porcelain cap-and-pin insulators [1.1].

Glass has a lower melting point than porcelain, making it more vulnerable to surface erosion due to the heat produced by surface discharges [2.2]. Problems occur in polluted environments where channelling of the glass surface especially at the underside undermines the mechanical strength of the unit [1.1].

Cap-and-pin insulators, both porcelain and glass, can form chains to support large mechanical loads. They retain their structural integrity even if the dielectric of a unit is ruptured. However, ceramic insulators are brittle and thus susceptible to vandalism attacks or shooters.

For polluted conditions, the flashover performance of ceramic insulators is significantly reduced and larger creepage is required thus resulting in heavy and bulky insulator units. The need to reduce the size of high voltage electrical systems introduced the use of polymeric insulators that are lightweight and due to their water-repellent properties have superior performance in polluted environments [1.1].

2.1.3 Polymers

Polymers are mostly used for housing materials of composite insulators. The housing encases a fibrous composite core of high mechanical strength. The polymer housing should protect the core from any damage deriving from invasion of water and humidity or leakage current and discharges and also provide the insulator profile [1.1]. This profile should control the leakage current on its surface by providing the necessary creepage distance and minimize the catching of air borne contaminants on its surface [1.1].

The lightweight composite insulators provide a high strength to weight ratio and are more compact as they can provide a longer creepage for a given axial length compared with ceramic insulators [1.1,1.4][2.3]. Moreover, the non-brittle housing protects the unit from vandalism attacks. They also have a smaller overall diameter that tends to reduce leakage current and improves its performance in polluted environments [1.4].

Polymers consisting of silicone structure [2.4] show a superior contamination performance that is attributed to the water-repellent properties of their surfaces [1.1, 1.4]. Unlike ceramic materials, the surface free energy of these polymeric materials is low and as a result they do not allow water to settle on the surface in a form of a thin layer but forces it to form separate discrete beads [1.2]. The hydrophobic nature of such polymers constitutes a significant advantage compared with ceramic dielectrics [1.4].

While manufacturing cost of polymeric insulators has been a concern [1.1], it has now been argued that composite insulators for transmission lines are economically competitive to porcelain and glass insulators [2.1]

Unfortunately, all the benefits offered by polymers do not come without problems. While ceramic dielectrics are materials of strong inter-molecular bonds, this is not the case for polymers [1.1], hence, making them vulnerable to thermal damage. The degradation of polymeric insulators during service, referred to as ageing, has a negative impact on their performance and is caused by the different stresses sustained during service.

2.2 Ageing and hydrophobicity of polymeric insulators

Ageing of polymeric insulators in service can be caused by electrical processes such as surface discharges or corona, weathering such as UV radiation, temperature and humidity, mechanical stresses that affect the fibrous core and chemical attack [2.5]. Spellman *et* al. [2.6] reviewed the main ageing factors leading to polymeric insulators degradation.

Polymeric materials used for composite insulator housings do not consist purely of one polymer but could be made of a mix of different polymers with other additives like antioxidants, ultra-violet absorbers and fillers such as alumina trihydrate that absorbs heat produced by surface discharges for enhancing the resistance against erosion and tracking [1.1].

For the pollution performance, the damage induced by surface discharges is of critical importance. The temperature produced by surface discharges can decompose the organic polymer, leaving traces of carbon forming resistive paths, a procedure called tracking [1.1] [2.2]. Erosion is the thermal damage associated with the loss of material from the polymer surface, especially in regions of localised discharge activity. Both tracking and erosion effectively reduce the performance of the insulator, and polymeric materials used on outdoor insulators should be assessed for their ability to resist such degradation.

Hydrophobicity is the main attribute of polymeric insulators that results in their superior pollution performance. However, as a result of ageing, polymeric insulators in service might lose their water-repellent properties and revert to the hydrophilic state observed for ceramic insulators [1.4]. Therefore, hydrophobicity is a dynamic property of polymeric insulators that could be lost

during service but can also be recovered if enough relaxation time from excessive electrical stress is given [2.7].

Two common polymeric materials used for outdoor insulation are ethylene propylene diene monomer (EPDM) and silicone rubber (SiR). Recently, the latter has been preferred for employment of composite insulators in severe ambient conditions [1.2] because of its excellent hydrophobic properties and its ability to transfer hydrophobicity to its adhering pollutants [2.8].

While both EPDM and SiR in service show at the beginning a superior pollution performance due to their hydrophobic surfaces compared with ceramic insulators, during service and under the influence ageing, they lose their surface hydrophobicity [2.9]. However, silicone rubber preserves its hydrophobicity for a longer time and, in addition, it shows a higher hydrophobicity recovery rate than EPDM [2.10]. These excellent properties of silicone rubber have also led to the development of room-temperature-vulcanised silicone rubber coatings for the enhancement of the performance of ceramic insulators [2.11].

The hydrophobicity of silicone rubber is attributed "to the low molecular weight (LMW) silicone chains, comprising methyl groups attached to silicon atoms, that have diffused to the surface" [1.2]. When surface discharges occur on the polymer surface, these bonds can be broken resulting to a loss of hydrophobicity but a new layer of LMW covers the surface. Very important is also the process of transferring hydrophobicity to the pollutants residing on the surface of the silicone rubber insulator which is practically the attachment of LMW to the pollutants [2.12]. The way this transfer takes place is not totally clear but suggestions related it with diffusion, evaporation or the capillary effect [2.13]. In some cases the pollutants have a significant non-soluble component that impedes the process of hydrophobicity recovery by covering the silicone rubber layer [2.13].

2.3 Pollution Flashover

The pollution flashover mechanism depends on the nature of the dielectric material. In the hydrophilic case, where ceramic insulators belong, when the insulator surface is wetted, a thin film of electrolyte covers the surface whereas

in the hydrophobic case, e.g. silicone rubber, the water resides on the surface in the form of discrete beads without the whole surface being wetted.

2.3.1 Flashover mechanism for a hydrophilic case (ceramic insulators)

In the review compiled by CIGRE working group 33.04 [1.3], the process of pollution flashover is described as follows:

1. Contaminants like soluble salts or dilute acids or alkalis are deposited on the insulator surface and eventually form a pollution layer. There are two cases: the pollution layer can be in the form of a liquid electrolyte or the layer is non-conductive when is dry. In the first case, steps 3 to 6 might take place immediately whereas for the case of a dry non-conductive layer, a process of layer wetting described in step 2 is required.
2. Under conditions of slow humidification such as fog, mist light rain, sleet or melting snow or ice, the pollution layer becomes wet and conductive. A heavy rain could be either beneficial by washing off the pollution from the insulator surface or could lead directly to flashover due to bridging sheds together through water cascades.
3. Under energisation and with a wet conductive layer on its surface, the insulator conducts a surface leakage current which dries out parts of the wet layer due to the current heating effect.
4. The leakage current density is always non-uniform resulting in a non-uniform drying of the wet layer where some parts get dry faster than other, thus creating dry zones, called dry-bands, that interrupt the flow of current on the pollution layer.
5. The dry-bands have a width that may be only a few centimetres and they bear across them the insulator energisation voltage. This creates the conditions for the air breakdown, and the dry-bands are bridged by surface discharges that are electrically in series with the wet layer. Fast current pulses are associated with the spanning of dry-bands by discharges.
6. The resistance of the undried pollution layer is controlling the discharge current and, if it is low enough, the dry-band discharges remain active and gradually longer sections of the insulator are spanned. However, this

results in a further decrease of the wet layer resistance, elongation of the discharges and finally in the complete bridging of the insulator in the form of a flashover arc.

Figure 2-2 shows the main stages of pollution flashover for ceramic insulators.

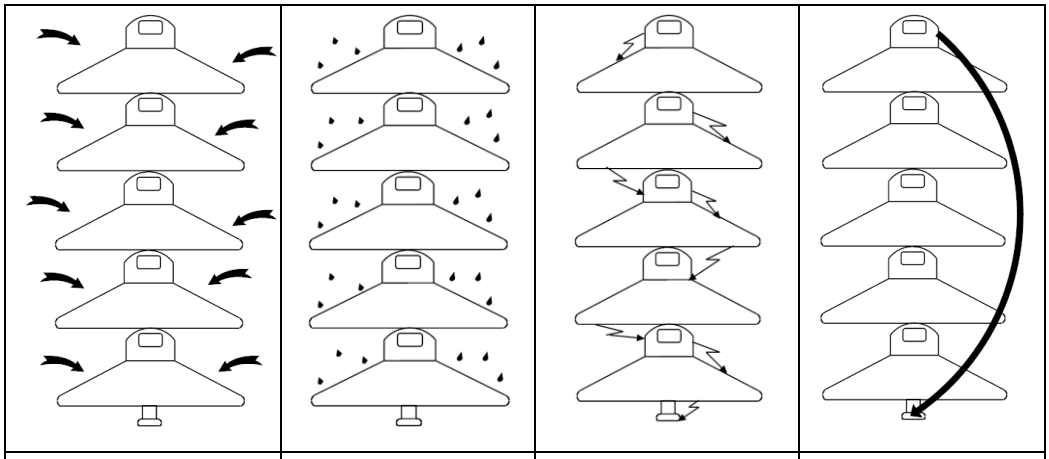

Figure 2-2. Pollution flashover process for the hydrophilic case. Schematic representation recreated from [1.3].

(a) Dry-bands

The reason for the pollution flashover failure of insulators is the formation of dry-bands [2.14]. The non-uniform surface leakage current and the resulting heat dissipation leads to the evaporation of the wet layer and the formation of dry zones that interrupt the flow of current. Power dissipation, and thus dry-band formation, is related with the surface electric field E and the surface current density J [2.15]:

$$E = \rho \cdot J \tag{2-1}$$

where E is the electric field, ρ is the surface resistivity of the layer and J is the surface current density. Power dissipation is given by

$$P = E \cdot J \tag{2-2}$$

that can be expressed as

$$P = \rho \cdot J^2 = \sigma \cdot E^2 \tag{2-3}$$

where σ is the conductivity of the pollution layer.

Hampton [2.16] measured the voltage distribution along a polluted flat insulation strip and described the process of dry-band formation. Salthouse [2.15] investigated the critical layer temperature and critical field strength necessary for the initiation of dry-band formation and confirmed the observations of Hampton related with the connection between the applied voltage and the dry-band resistance. In an extension of the previous work, Löberg and Salthouse [2.14] investigated the development of the dry-band width and the temperature profiles using a chromagram sheet polluted with a solution of cobalt chloride in methanol that indicated the formation and location of dry-bands. They concluded that the dry-band width and rate of growth are both controlled by the dissipated power per unit areas in the band. Moreover, they derived temperature profiles along the test specimen deduced by measurements of surface resistivity that showed that even a small increase of the temperature above ambient results in a non-uniform voltage distribution. These temperatures had good agreement with the measured values using an infrared microscope. The voltage necessary for the inception of a dry-band is lower for lower values of initial surface resistivity. Power dissipation in a dry-band and dry-band width have an inverse relation [2.14].

Texier *et* al. [2.17], also used a simple geometry of a rectangular sheet of blotting paper polluted with a solution of sodium chloride over a Perspex substrate, energised with a 0-5 kV test voltage at 50Hz across its ends. Infrared photography was employed to detect the location and formation of dry-bands and to plot temperature profiles. The abrupt fall of current associated with the formation of a dry-band was recorded and the dependence of the time delay, from energisation to dry-band formation, $t_{s,}$ on voltage for different pollution concentrations was described confirming that dry-band formation is initiated for lower voltages for layers of lower resistivity. Also, in the same work it was shown that there is an inverse relation between the time delay to dry-band formation and the average power dissipated in the dry-band [2.17].

Dry-bands have also been investigated during clean fog tests of cap-and-pin ceramic insulators [2.18] using a camera and a video system. The formation and development of dry-bands and their width was monitored by measuring the

length of the pre-flashover discharges for different voltage levels. Later these results were correlated with the available flashover models [2.19].

(b) Modelling of flashover mechanism

After the formation of the dry-band, the insulator voltage falls across this narrow zone, giving rise to the local electric field strength. Given that this electric field has a sufficient magnitude, air breakdown follows with the propagation of a discharge that spans the dry-band. The current of this discharge is controlled by the series resistance of the wet pollution layer. The surface current, preserving its continuity through the dry-band discharge, continues to further evaporate the wet layer, increasing the dry-band width.

In [2.18], three cases are described:

(a) In the first case, the voltage gradient is not sufficient to sustain the inception of dry-band discharges as the width of the band becomes wider. This scenario would normally apply when the wetting of the insulator surface has stopped thus the dry-band width constantly increases [2.18].

(b) When surface wetting is continuous, the discharge activity is intermittent as the dry-band width can be reduced allowing the propagation of discharges, that will in its turn increase the local power dissipation and fluid evaporation will increase the dry-band width again, ceasing the discharge activity. This procedure would resume again as soon as the electric field gradient is sufficient for the bridging of the dry-band. The gradual washing of the pollution layer or the end of surface wetting will eventually stop this reiteration [2.18].

(c) In the third case which leads to flashover, the dry-band width is increasing but dry-band activity is not eliminated. The surface discharges get more elongated and, after a point where the dry-band width reaches a critical width, surface discharges lead to a complete bridging of the insulator. The conditions under which dry-bands start to be spanned by discharges and the critical values that mark the transition from a dry-band discharge to a flashover have been the object of modelling and experimental research [2.18].

Williams *et* al. [2.19] provided a review of the flashover mechanism models for ceramic insulators for clean-fog tests. A newly proposed model has also been published recently for lightly polluted insulators [2.20].

Hampton's [2.16] criterion for the flashover breakdown is that the voltage gradient of the propagating arc should be less than the voltage gradient of the pollution layer, $E_a<E_p$.

Waters *et* al. [2.20] provided a summary of the review work of Hutzler, Rizk [2.21] and Claverie [2.22] on the mathematical models of dry-band flashover. According to the partial-arc model, the discharge bridging a dry-band follows an arc current-voltage characteristic. Therefore:

$$U_a = \frac{NL_a}{i^n} \tag{2-4}$$

where U_a is the necessary voltage for the maintenance of an arc carrying a current i and extending to a length L_a. N and n are empirical constants.

However, for the a.c. case, the voltage should be high enough to re-strike the arc during each cycle. Figure 2-3 shows a schematic representation of an insulator with a creepage length L with a pollution layer of layer resistance per unit length r, which has formed a dry-band. The dry-band is bridged by a partial-arc. The re-strike voltage should be able to maintain both the partial-arc and the voltage drop on the pollution layer:

$$U = U_a + ir(L - L_a) \tag{2-5}$$

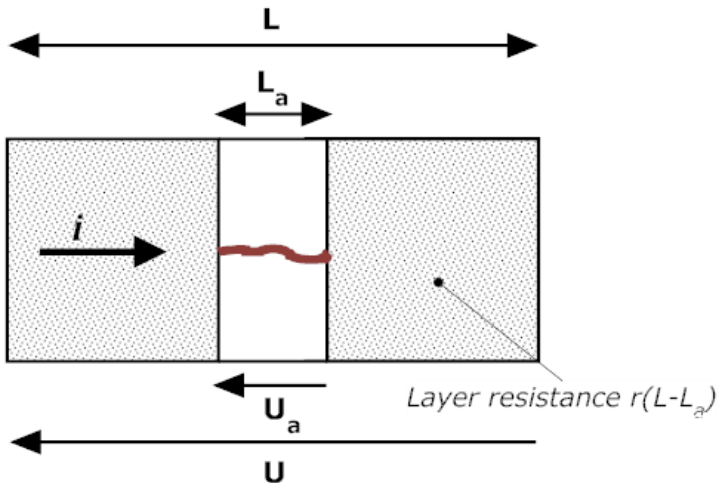

Figure 2-3. Schematic representation of the partial-arc, recreated from [2.20].

Further analysis concludes with the relationships for the arc length, voltage and current [2.20]:

$$L_a = \frac{rL}{r + \frac{A-N}{i^{m+1}}} \tag{2-6}$$

$$U = AL_a\left(\frac{r(L-L_a)}{(A-N)L_a}\right)^{\frac{m}{m+1}} \tag{2-7}$$

$$i = \left(\frac{(A-N)L_a}{r(L-L_a)}\right)^{\frac{1}{m+1}} \tag{2-8}$$

where A and m are constants.

The critical flashover conditions are derived for $dU/dL_a=0$:

$$U_F = Br^{\frac{m}{m+1}}L \tag{2-9}$$

where $B = \frac{A}{m+1}\left(\frac{m}{A-N}\right)^{\frac{m}{m+1}}$

$$L_{aF} = \frac{L}{m+1} \tag{2-10}$$

$$i_F = \left(\frac{A-N}{mr}\right)^{\frac{1}{m+1}} \tag{2-11}$$

The commonly assigned values for the constants are m=0.5, A=8x10^4 and N=10^4 V A$^{0.5}$m^{-1}. It is interesting to note that these partial-arc equations for the critical flashover voltage and arc length are both proportional to the insulator creepage length. For m=0.5 and from Equation (2-10), the critical arc length that will lead to flashover is 2L/3 [2.20].

The thermal ionization of the channel that carries the partial-arc requires a high current that will be accompanied by low voltage gradient values of the range 0.1to 1 kV/m. For polluted insulators, the voltage gradients involved are usually in the range of 150 to 20 kV/m [2.20]. Moreover, the electrode vaporisation is

very important for the maintenance of an arc channel. However, surface discharges on polluted insulators are very frequently observed in regions far from the electrodes, i.e, in the middle section where the discharge roots originate from the pollution layer.

Based on these observations, Waters *et* al. [2.20] proposed another approach for the modelling of dry-band discharges. The spark-model suggests that the conductivity of the spark leader is maintained by impact ionization that occurs at low temperatures, as opposed to thermal ionisation observed for arc channels at high temperatures. Figure 2-4 shows a schematic representation of the spark model. The spark leader channel of length C spans the dry-band. The dry-band might become larger as streamers of combined length S sprouting out the spark leader can penetrate the dry-band.

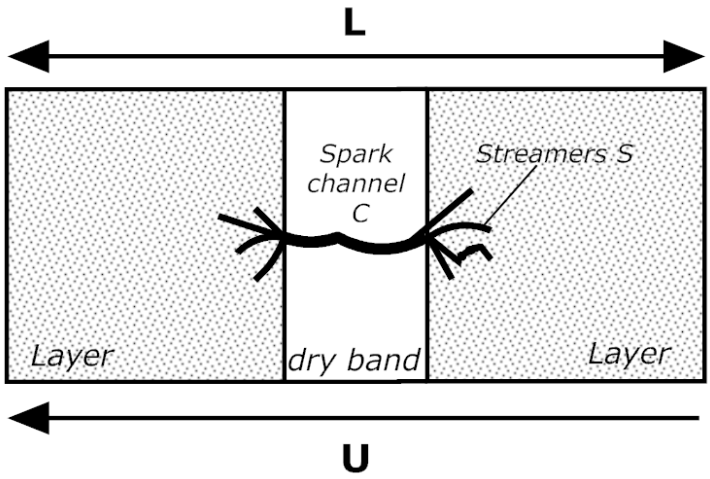

Figure 2-4. Schematic representation of the spark model, recreated from [2.20].

For figure 2-4, the voltage drop U will be

$$U = E_c C + E_s S + ir(L - C - S) \tag{2-12}$$

where E_c and E_s are the spark channel and streamer field respectively. The flashover conditions are

$$U_F = E_c L + \frac{1}{kr}\left(1 - \frac{E_c}{E_s}\right) \tag{2-13}$$

$$S_F = \frac{1}{krE_s} \quad (2\text{-}14)$$

$$i_F = \frac{E_c}{r} \quad (2\text{-}15)$$

where $k=2\pi\varepsilon_o\mu$ and μ the electron mobility [2.20]. This study also calculated the pre-flashover length of the spark channel and the streamers as

$$C = 1.80\, i \ \text{[m]} \quad (2\text{-}16)$$

$$S = 0.36\, i \ \text{[m]} \quad (2\text{-}17)$$

The spark model advocates that a transition to higher current arc discharges can occur in the case of heavily polluted insulators. During this research work, the study of a stable dry-band formed on silicone rubber insulation was possible and showed that the dry-band discharges follow streamer-like characteristics rather than those of an arc [2.23].

2.3.2 Flashover mechanism of a hydrophobic case (polymeric insulators)

Due to the dynamic nature of the hydrophobic surface of polymeric insulators, the flashover mechanism is substantially different from that of ceramic insulators and hydrophilic dielectrics [1.2]. Generally, non ceramic insulators show a better flashover performance than ceramic insulators of similar creepage length [2.24].

The higher permittivity of water droplets residing on the hydrophobic surface compared with the permittivity of air and the dielectric material acts as an electric field enhancer. Also, the air over the dry part of the insulator surface is shortened by the intervening gaps introduced by the droplets which tend to change shape under the influence of the electric field [2.25].

Karady and Shah [2.26,2.27] described a qualitative mechanism for the flashover initiated by water-drops rather than dry-bands of polluted silicone rubber insulators (Figure 2-5). The insulator surface gradually gets polluted during service. For both marine and inland pollution, the surface tends to accumulate a

uniform pollution layer. Due to diffusion of LMW chains from the bulk of the polymer, a thin oil-like layer forms on the insulator surface, covering the pollution. Wetting from fog, a morning mist, light rain or the condensation of the air humidity on the insulator, leads to the formation of water drops that reside on the hydrophobic surface (Figure 2-5A). At this stage, water by diffusion and through the thin polymeric layer, wets the dry contaminants resulting to highly resistive regions surrounding each droplet (Figure 2-5B). At the same time, salt from the pollution layer and through the oily layer is transferred and dissolved in the water beads increasing their conductivity. The droplets change shape and elongate under the influence of the electric field which become more flat and elongated. During this process, neighbouring droplets may merge to form conductive filaments with a highly resistive layer around them (Figure 2-5C).

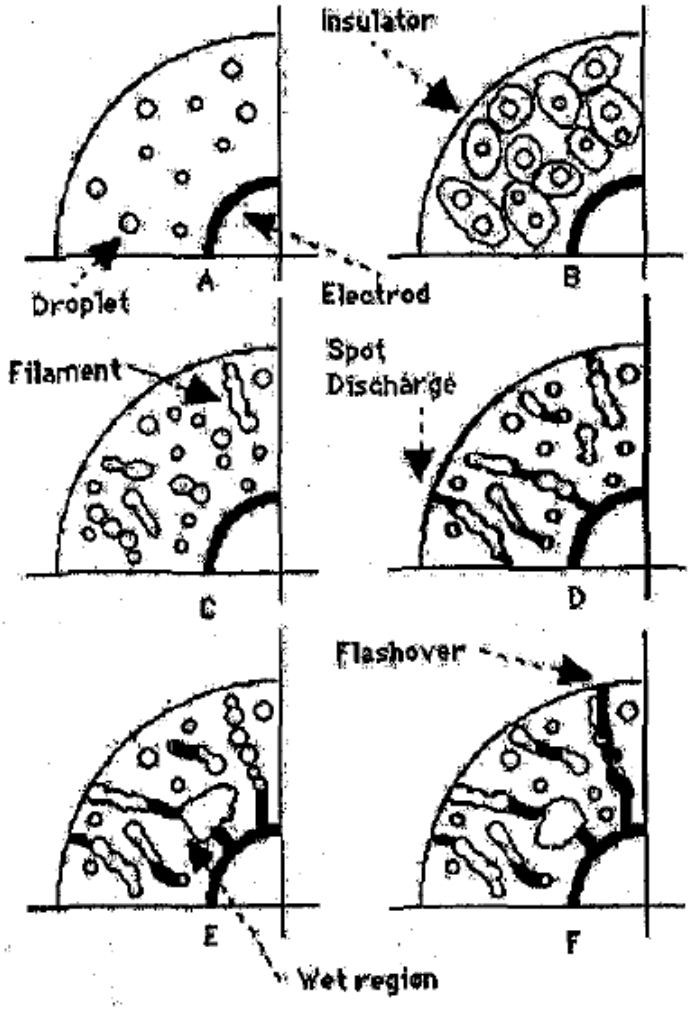

Figure 2-5. Flashover development for non-ceramic insulator. Figure taken from [2.26].

The elongated filaments shorten the distance between the electrodes thus giving rise to even higher values of electric field between them and other neighbouring filaments. Spot discharges are initiated between the filaments (Figure 2-5D). The discharge activity leads to a loss of hydrophobicity that favours further expansion of droplet filaments that form wet regions. Such wet regions may form also near the electrodes under the influence of corona and surface discharges. Unlike the uniform wet pollution film observed for ceramic dielectrics, the wet regions are patched on the insulator surface, and are surrounded by a high resistance layer with discrete droplets (Figure 2-5E). The growth of wet areas along with the further elongation of water filaments finally creates a conductive path capable of leading to a flashover when the arc voltage gradient is lower than that of the filament (Figure 2-5F) [2.26,2.27].

The mechanism described above is indicative of the challenges that are faced for establishing a commonly accepted test method for polymeric insulators due to the dynamic interaction of their surface with the environment.

It is generally agreed that the major cause for polluted insulator flashover is from dry-band formation.

2.4 Artificial pollution testing of non-ceramic insulators

Artificial testing of outdoor insulators in the laboratory shows advantages in terms of cost, time and variation of the pollution severity compared with pollution investigation under natural conditions [1.2]. The pollution performance is an essential element for the selection and dimensioning of insulators which gave rise to the need to establish a commonly accepted method for the testing of outdoor insulation.

The IEC-60507 [1.6] international standard describes two test methods for the assessment of insulation pollution performance: the Salt Fog test and the Solid Layer test which is also known as Clean-Fog test. The first test replicated better pollution type B found for marine environments while the Solid Layer method replicates contamination type A, containing a significant non-soluble material, common for industrial and inland environments. These tests have been developed for ceramic insulators with hydrophilic surfaces. Due to the dynamic

nature of hydrophobic surfaces, the direct adoption of the IEC-60507 methods for the testing of polymeric insulators is hindered by serious implications.

For the Solid Layer method, a pollution suspension, either Kieselghur or Kaolin, is applied directly on the insulator surface before the test and left to dry. The insulator is then tested in clean fog in a test chamber [1.6]. The highly hydrophobic surface of a new polymeric insulator causes serious problems for the application of a uniform pollution layer. For hydrophobicity transfer materials such as silicone rubber, the rate of this transfer to the adhering pollutants from the moment the pollution is applied until the test object is tested is an issue of serious consideration. Moreover, the temporary loss of hydrophobicity due to surface discharging can greatly affect the estimation of the flashover performance. All these issues have been raised and discussed in CIGRE publications [1.4][2.28].

A recent paper by Gutman and Dernfalk [2.29] reviewed the current status of polymeric insulators artificial testing. There have been two approaches from CIGRE for the testing of non-ceramic insulators: the one advocates the use of modified versions of the existing test methods for ceramic insulators and the other proposes the development of new testing procedures. The first approach seems to be opted more from researchers, and effort has been placed to apply changes on the standard methods in such way that the artificial testing can replicate service conditions more realistically.

The application of the pollution layer, as instructed by the Solid Layer method, on the water-repellent surface is a fiddly task. It has been deemed practically impossible to achieve a uniform pollution layer without a preconditioning of the polymeric surface [2.29]. The Arizona State University method [2.30] suggests the application of a thin layer of dry powder kaolin or kieselghur on the insulator surface, that will provide a hydrophilic interface on which the pollution slurry can be applied. Another method developed in Cardiff University [2.13] proposes the addition of a wetting agent Triton X-100, as used for the IEC-60587 inclined-plane test, in the kaolin/salt pollution suspension in order to achieve a uniform pollution layer. Both methods have been included in the recent CIGRE guidelines

[1.4]. The application of the pollution can be performed by spraying, dipping or using a brush [2.29,2.31], the second being preferred for smaller test objects.

The delay time from the application of the pollution layer until testing can be varied to achieve different grades of hydrophobicity recovery. The extremes are a hydrophilic surface for a recovery time less than 5h and a hydrophobic condition achieved after 7 days of recovery [2.29]. Any intermediate conditions can be explored.

The up-and-down method is usually used for the estimation of the withstand voltage. A recent joint research work [2.32] involving 13 high voltage laboratories for a round-robin test of polymeric insulators using the solid layer method with preconditioning and hydrophobicity recovery showed promising results for the development of a reproducible test procedure.

2.5 Testing of materials used for outdoor insulators

Polymers used for outdoor insulation should be evaluated for their ability to resist tracking and erosion [1.1]. The IEC-60587 [1.10] inclined-plane test is a well-established method used for testing housing materials of composite insulators. The test is characterised by extreme severity as high voltage gradients are applied that could exceed 1.2 kV/cm, a considerably higher value than the 0.2 to 0.3 kV/cm usually experienced for insulators in service [1.1].

The test is designed to encourage the formation of dry-bands and surface discharges. The test objects are rectangular with dimensions 120 mm x 50 mm with a preferred thickness of 6 mm, on which stainless steel electrodes are attached (Figure 2.6). The sample is mounted at an inclined position at 45^{o} to the horizontal with the test surface facing downwards. A water solution consisting of ammonium chloride and a non-ionic wetting agent is fed from the top electrode and traverses the test surface towards the lower electrode [1.10]. The test voltage can be varied during the test (stepwise tracking voltage) or could remain constant. The second method has been employed for the purpose of this research work. The preferred constant voltages are 2.5 kV, 3.5 kV or 4.5 k V and are applied for 6 hours.

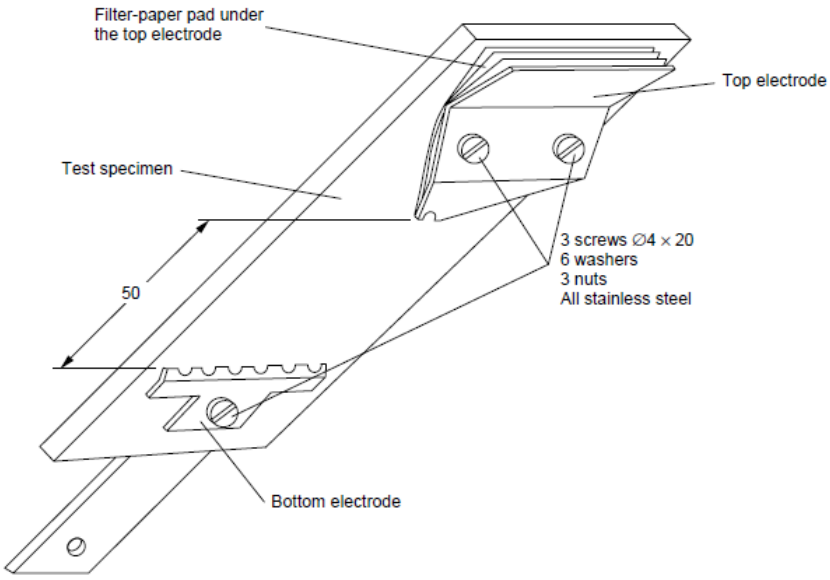

Figure 2-6. The IEC-60587 inclined-plane test sample with fitted stainless steel electrodes. Figure taken from [1.10].

The standard defines two end-point criteria that mark the end of the test. According to criterion A, the test is terminated if the leakage current exceeds 60 mA for a period over 2 seconds or a hole shows on the sample surface due to erosion or the sample ignites. Criterion B determines the end of the test when the surface track reaches a mark 25 mm from the lower electrode or when a hole shows due to erosion or when the sample ignites [1.10].

The damage suffered during the inclined-plane test on composite and silicone rubber samples has been monitored using ancillary tools such as infrared photography and current measurements [2.33,2.34] that have attempted to correlate sample surface temperature with the material loss due to erosion. The increasing use of direct current high voltage systems stimulated the interest regarding the resistance of polymeric materials under DC stress. Results showed [2.35,2.36] that DC stress leads to more extensive damage compared with AC stress, with the positive polarity causing the worst damage. Comparative tests under AC and DC stress for RTV, HTV silicone rubber samples and EPDM samples have been performed as well showing an advantage for RTV silicone rubber for AC stress [2.37]. A recent study at Cardiff University [2.38] that tested more than 50 silicone rubber samples at the inclined-plane test suggested that the rate of

increase of the accumulated energy could be used as an indicator for the imminent failure of test insulators.

It must be noted that suggestions for the improvement of the standard incline-plane test have been raised by laboratories with long experience in inclined-plane tests regarding the inspection of the steel electrodes, the proposed voltage levels and flow rates of the contaminant, the erosion depth measurement, the mounting of the sample on the test position and the number of tests required to assess the overall performance of a material [2.39,2.40].

Standard tests performed on full insulators to assess the performance of insulator materials and designs against tracking and erosion are described in IEC-62217 [2.41]. The 1000 h salt-fog test is performed in a fog chamber while the tracking wheel test requires special facilities [2.42] consisting of a rotating wheel that would during a cyclic procedure immerse the test insulator in a salt solution, allow it later to drip, then energize it for 40 seconds and finally allow it cool down and repeat the cycle again. Both tests have been designed to be very severe in order to accelerate the ageing caused mostly due to electrical discharges [2.41].

During the pollution testing of polymeric insulators, a number of diagnostic methods were used including voltage and current measurements, UV and thermal imaging in addition to visual observations. However, it must be noted that the use of thermography during insulator testing is relatively recent. Infrared recording could detect internal core defects, though not as sensitive as ultra-violet imaging. However, it has the ability to clearly manifest the presence of dry-band arcing, as reported in [2.43]. For the purpose of monitoring polymeric insulators in service, a more precise assessment can be achieved when thermography is employed in conjunction with UV recording [2.44,2.45]. Naturally aged polymeric insulators sprayed with a clean mist have been tested along with infrared imaging, and regions of intense dry-band arcing were correlated with hot regions detected by an infrared camera [2.46]. Investigation of the polymeric surface in the infrared spectrum have been reported for tracking wheel tests as well [2.47]. However, to author's knowledge, there has

not been an investigation of the formation, growth and dynamics of the dry-band itself during clean-fog tests by utilizing infrared photography. During the course of the present research work, infrared photography has been a very useful tool for the study of stable dry-bands during inclined-plane tests of silicone rubber samples [2.23,2.48,2.49] and during clean-fog tests of silicone rubber insulators [2.50], as it will be described later.

2.6 Insulator dimensioning and selection

2.6.1 Standards specifications

The design, selection and dimensioning of polymeric insulators is the subject of international standards [1.5]. The newly revised IEC standards adopted the guidelines suggested by CIGRE [1.3, 1.4] that overturned the traditional approach which was mainly based on controlling the creepage distance of the insulator for different classifications of environmental pollution severity. The revised guidelines acknowledge that other parameters must be taken into consideration for the selection and dimensioning process such as the type of application the insulator will be employed, the parameters of the system, environmental parameters (one of them the pollution severity) and other constraints such as the cost or the size of the insulator [1.5].

Due to the superior pollution performance of polymeric insulators, reduced creepage distances could be employed. However, the possibility of a temporary or permanent loss of hydrophobicity should also be taken into consideration. That is the reason why frequently polymeric insulators were over-designed by following the guidelines for ceramic insulators. However, under specific conditions, reduced creepage distances could be attempted [2.51]. Over-designing insulators with very long creepage distances for a given axial length could be problematic, and very high deviations from the suggested creepage factor result in very ‘cramped’ designs that are susceptible to surface discharging [2.51]. Therefore, achieving a long creepage distance per unit of axial length and remaining within the acceptable operation limits is no easy task.

The insulator characteristics that are explored for the selection of insulators for polluted environments are the type of the housing material, the length, the

diameter, the shed profile, the attitude and the presence of an internal voltage grading [1.4].

2.6.2 Site pollution levels

The site pollution severity (SPS) is classified in five categories [1.5]:

a. Very light
b. Light
c. Medium
d. Heavy
e. Very heavy

It must be noted that this classification is not directly related with the classification suggested by the older standard IEC 60815:1986. Pollution severity is expressed as the Equivalent Salt Deposit Density (ESDD) which is the "amount of sodium chloride (NaCl) that, when dissolved in demineralised water, gives the same volume conductivity as that of the natural deposit removed from a given surface of the same insulator divided by the area of this surface, generally expressed in mg/cm^{2}" [1.5]. The non-soluble component of the deposited pollution is expressed as the Non Soluble Deposit Density (NSDD) which is the "amount of non soluble residue removed from a given surface of the insulator divided by the area of this surface, generally expressed in mg/cm^{2}" [1.5].

Depending on the type of pollution (A or B) and insulators type, a site could be classified in one the above categories using tables available in the IEC standard (Figure 2-7). After the site pollution severity has been identified, the reference unified creepage distance can be calculated. Site pollution severity should not be adopted directly for artificial pollution tests as correction factors are applied [1.5].

2.6.3 Creepage length

While an increased creepage distance is associated with a better flashover performance, an increasing diameter can result in a reduction of the flashover voltage [1.1]. For this reason, correction factors apply for the calculation of the unified specific creepage distance to compensate for the influence of the average diameter in the insulator performance.

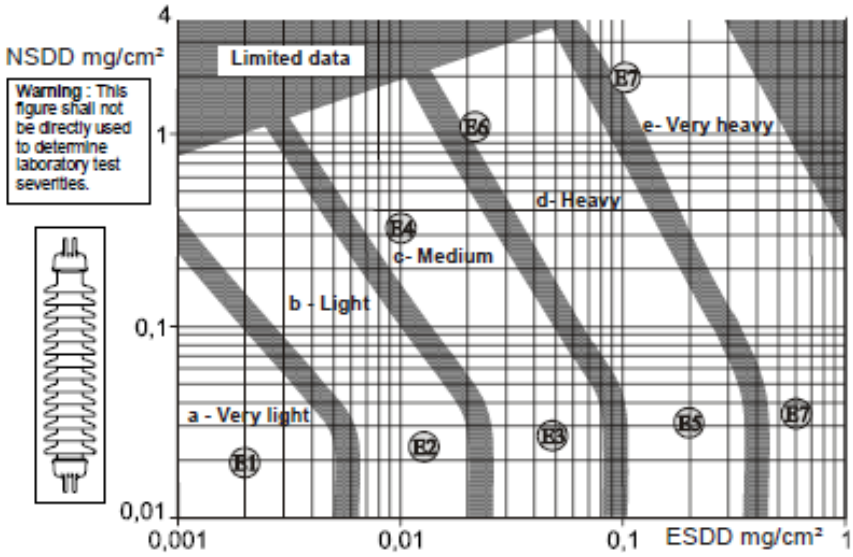

Figure 2-7. Relationship between ESDD and NSDD of pollution type A and the site pollution severity classes for long rod insulator. Figure adopted from [1.5].

The unified specific creepage distance (USCD), that replaced the specific creepage distance (SCD) of the older standard, is "the creepage distance of an insulator divided by the r.m.s. value of the highest operating voltage across the insulator" [2.51], and is expressed in mm/kV. The reference unified specific creepage distance (RUSCD) is the USCD without being corrected by correction factors for the influence of altitude and for diameters greater than 300 mm [2.51].

$$Corrected\ USCD = RUSCD \times K_a \times K_{ad} \quad (2\text{-}18)$$

where K_a and K_{ad} the correction factors for altitude and average diameter respectively.

In particular, the average diameter correction factor depends on the polymer material and the service conditions, as shown in Figure 2-9 which has been adopted from [2.51].

2.6.4 Shed profile

The shed profiles are also recommended in the standard. Complex profiles with deep under-ribs cannot be achieved due to the moulding restriction for polymeric insulators [1.1].

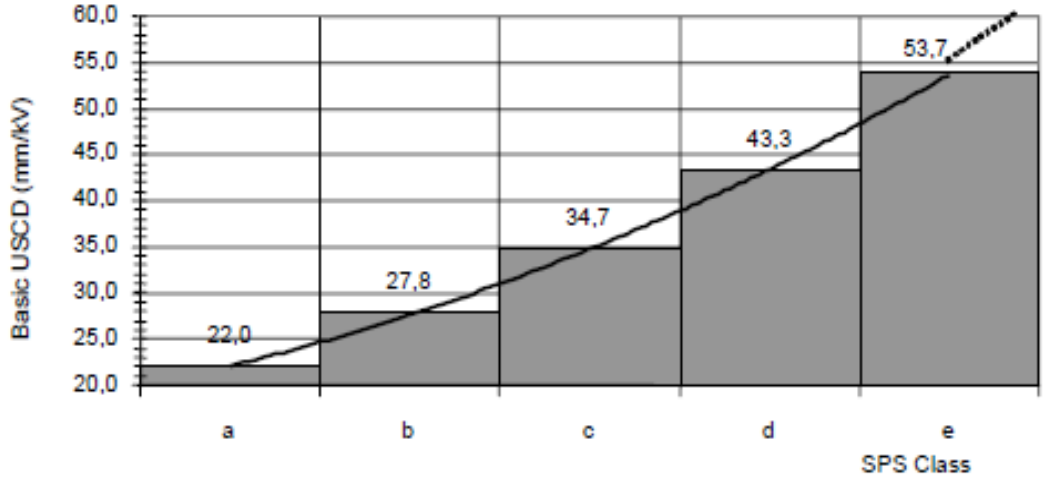

Figure 2-8. Relationship between the minimum reference specific creepage distance and the site pollution severity. Figure adopted from [2.50].

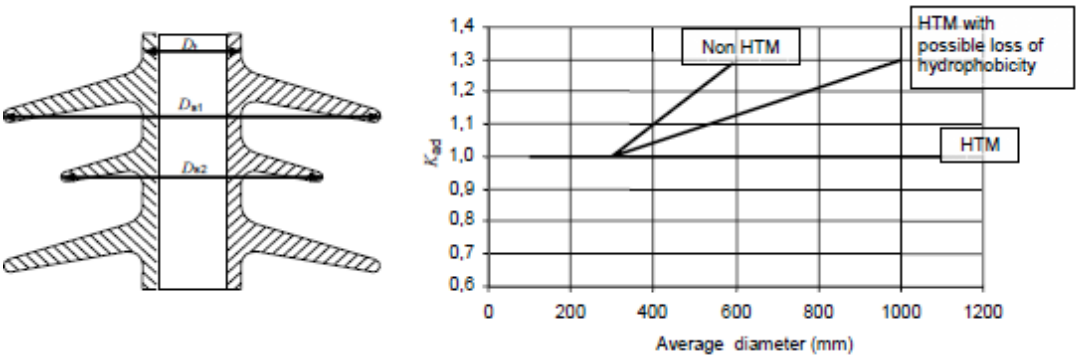

Figure 2-9. Average diameter correction factor K_{ad} where the average diameter is $(2D_t + D_{s1} + D_{s2})/4$. Figure adopted from [2.50].

Open profiles where the sheds do not have a steep top slopes (< 20°) have good self-cleaning properties and are usually suitable for all environmental conditions. Steeper slopes are more suitable for pollution with little or no non-soluble component as the ability to self-cleaning is restricted. The same applies for profiles employing shallow under-ribs. Alternating shed profiles are suitable in conditions of heavy wetting like heavy rain where increased shed spacing inhibits water cascades to bridge the sheds.

The insulator attitude could affect the insulator performance with increasing inclined angles resulting in increased flashover levels [1.1] for angles up to 20° after which further improvement for angles up to the horizontal is very small.

After a candidate insulator has been selected, artificial pollution tests that simulate the service conditions can be performed to confirm the aptness of the

solution. However, as already discussed, in the case of polymeric insulators, laboratory testing is not without its own challenges due to the implications introduced by the dynamics of polymeric surfaces.

2.7 Texturing of polymeric insulators

The extensive use of polymeric materials, and especially hydrophobicity transfer materials like silicone rubber for composite insulators, did not lead to the total elimination of pollution flashover. Severe ambient conditions would still result in partial discharging on the insulator surface and the design of polymeric insulators remains very simple mainly due to the moulding restrictions inhibiting the development of re-entrant profiles [1.9].

The surface leakage current on a polluted polymeric insulator has the highest density in the regions of the smallest contour perimeter which are the shank sections. Consequently, the surface electric field strength is also at its highest at these regions resulting in increased surface power dissipation. Heating is proportional to the power dissipation. Therefore, local heating leads to the formation of dry-bands and the damaging effect induced by the associated surface discharges.

Textured insulators are a novel approach [1.8] for the design of polymeric insulators that takes advantage of the moulding properties of silicone rubber. Fine texturing of the polymeric surface could be achieved by employing a pattern consisting of an array of contiguous or overlapping protuberances. The aim of this design is to reduce the surface power dissipation by reducing both the electric field and current density, as shown in Equation (2-2). This could be achieved by increasing both the surface area and the creepage distance of the insulator without increasing the overall longitudinal length of the insulator [1.9]. Moreover, textured patterns were expected to alleviate the damage induced on polymeric materials due to surface discharges, compared with non-textured samples of the same material, by introducing multiple paths for current conduction: as soon as one current path starts to dry as a result of Joule heating, its resistance will increase. However, the current flow will switch to an alternative path of lower resistance before severe thermal damage occurs [1.9].

2.7.1 Surface patterns

The geometry of such protuberances could be hyperboloidal, conical and pyramidal or other symmetrical shapes each resulting in a different variation of the surface area [1.9].

Figure 2-10 shows a side view of a protuberance that is formed as part of a sphere and has a height, c, and a base as a circle of radius, a. The radius of the sphere is b. Also, the top view of an array of contiguous part-spherical protuberances is shown (Figure 2-10b).

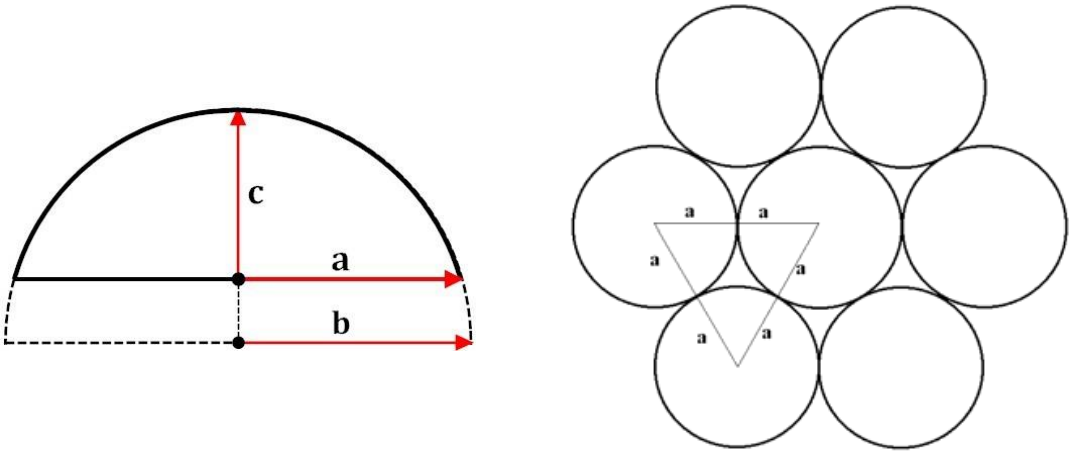

(a) (b)

Figure 2-10. Side view of part-spherical protuberance (a) and top view of an array of contiguous part-spherical protuberances (b) [1.8].

Therefore , we can write

$$a^2 = c\,(2b - c) \tag{2-19}$$

and the surface area of the spherical cap will be

$$A_p = 2\pi bc \tag{2-20}$$

From Figure 2-10b, the area of the triangular plane surface is

$$A_t = \sqrt{3}a^2 \tag{2-21}$$

The three neighbouring protuberance will increase this surface area to

$$A_{pt} = \frac{A_p}{2} + A_t - \frac{\pi a^2}{2}$$

$$A_{pt} = \mathrm{a}^2 \left[\frac{\pi b}{2\mathrm{b} - \mathrm{c}} + \sqrt{3} - \frac{\pi}{2}\right] \quad (2\text{-}22)$$

Therefore, the spherical protuberances will increase the surface area by a ratio

$$\frac{A_{pt}}{A_t} = 1 + \frac{\pi c}{2\sqrt{3}(2b - c)} \quad (2\text{-}23)$$

Equation (2-23) is suggesting that, for protuberances that are formed as part of spheres, the increase of the surface area is dependent on the height of the sphere cap and on the radius of the sphere. If the protuberance is a hemisphere (b=c) then the ratio for a contiguous hemispherical pattern will be

$$\left.\frac{A_{pt}}{A_t}\right|_{b=c} = 1 + \frac{\pi}{2\sqrt{3}} = 1.907 \quad (2\text{-}24)$$

which is independent of the hemisphere radius b. For a tightly arranged array of adjacent hemispherical protuberances, the surface will increase close to a limiting value of 2, which is the ratio of the hemisphere surface to the surface of the circular base. Ratios greater than 2 can be achieved by utilising other geometrical arrangements [1.9].

The typical approach for the design of outdoor insulators for polluted environments is the increase of the creepage distance per unit of axial length. The textured patterns aim to achieve both longer creepage and an increase of the surface area. For hemispherical protuberances, other patterns have been explored where the protuberances are overlapping forming intersections. Figure 2-11 shows such geometrical configurations along with the contiguous pattern (Figure 2-11A). The arrows indicate the circular arc paths formed by the intersections. Pattern B follows a hexagonal intersection of overlapping hemispherical protuberances while the intersections of patterns C and D have a square and triangular shape respectively [1.9].

Returning to the example of the contiguous hemispherical protuberances pattern (Figure 2-11A), the creepage distance per row in the direction of the electric field is 2.093a while the distance on the plane surface is $\sqrt{3}$a, marking an per unit increase of the creepage distance by a factor of 1.209, resulting in a substantial

decrease of both E and J [1.9]. The creepage factor is also independent of the hemisphere radius.

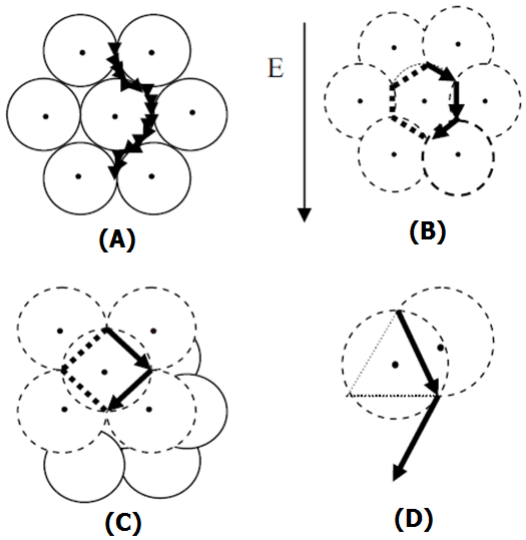

Figure 2-11. Textured patterns: contiguous hexagonal (A), intersecting hexagonal (B), intersecting square (C) and intersecting triangular (D) [1.8].

2.7.2 Power dissipation factor

Assuming that the plain and textured surfaces are covered by a pollution layer of same thickness t (metres) and conductivity σ (Siemens/metre), then the layer conductance is $k = t{\cdot}\sigma$ (Siemens) and is the same for both surfaces. For an insulator leakage current I, at position where the insulator circumference is C (metres) the current density inside the pollution layer is $J_{layer} = I/Ct$ (A·m^{-2}). As the thickness of layer t is constant, this can be expressed as a surface current density $J = J_{layer} \cdot t$ (A·m^{-1}).

For a given insulator region, if the surface area is increased by a factor α, consequently the current density J will be reduced by the same factor ($J_{\text{plain}}/J_{\text{textured}} = \alpha$). Similarly, if a textured pattern increases the creepage distance by a factor β, the electric field strength will be reduced by the same factor as well ($E_{\text{plain}}/E_{\text{textured}} = \beta$) Given that power dissipation is related with E and J according to the relationship given by Equation (2-2), a textured pattern would reduce the surface power dissipation per unit area of the insulator surface P (W·m^{-2}) by a combined factor $\alpha \times \beta$:

$$\frac{P_{plain}}{P_{textured}} = \frac{E_{plain} \cdot J_{plain}}{E_{textured} \cdot J_{textured}} = \alpha \times \beta \qquad (2\text{-}25)$$

While the well-established anti-fog designs increase only the creepage distance, thus affecting only factor β, textured patterns could control both the surface area (factor α) and the creepage distance (factor β) independently, thus achieving different combined power density factors $\alpha \times \beta$. This combined factor could function as a figure of merit for the ability of the textured design to inhibit the drying of the pollution layer by decreasing the surface power dissipation.

2.7.3 Theoretical classification of candidate textures

A theoretical classification of the candidate textures that would be assessed for the development of textured insulator prototypes was conducted based of the combined power density factor. Geometrical calculations on the patterns shown in Figure 2-11 are shown in Table 2-1.

Table 2-1. Theoretical classification of textured patterns. Table adopted from [1.9].

Texture	Area factor α	Creepage factor β	Power density factor αβ
1. Contiguous hexagonal	1.907	1.209	2.306
2. Intersecting hexagonal	1.446	2.356	3.407
3. Intersecting square	1.301	2.222	2.891
4. Intersecting triangular	1.209	1.814	2.193

The calculations presented in the above table suggested that based on the power density factor as a figure of merit for the anti-dry band performance, the contiguous hexagonal, the intersecting hexagonal and the intersecting square patterns were the most promising textures.

Early stage tests reported in [1.9] on non-textured silicone rubber samples and silicone rubber samples with a textured finish, similar to the contiguous configuration, showed some promising results. The present research work will describe the laboratory investigations of these textured patterns in a series of material tests and the development and testing of full textured insulators in clean-fog tests.

2.8 Conclusions

The problems arising from the pollution contamination are the leading factor that influences the design and selection process of outdoor insulators. Different profiles and materials have been employed to suppress the consequences of surface discharging and minimise the number of flashover events. The use of polymeric materials is currently the state-of-the-art technology for the improvement of the anti-pollution performance of insulators, mainly due to the water repellent properties of these materials. However, polymeric materials in service suffer from ageing degradation that could permanently or temporarily reduce their performance. Moreover, the laboratory evaluation of composite insulators is an intricate task due to the dynamic nature of polymeric materials.

The textured insulators research programme proposes a novel insulator design for polymeric insulators that aims to reduce the damage induced by surface discharges and improve the flashover performance. A theoretical classification of textured patterns consisting of an array of hemispherical protuberances showed that the creepage distance and the surface area can both increase without increasing the overall length of the insulator. The present work describes the experimental investigations of textured patterns using standard tests and novel test methods and ancillary diagnostic tools to assess whether the expected improvement can be achieved for textured insulators prototypes.

Chapter 3. Pollution Flashover of Silicone Rubber Insulator: Experimental Techniques and Test Protocols

Introduction

The selection and dimensioning of high voltage outdoor insulators for use in polluted environments and under severe ambient conditions should take into account the level of withstand voltage when compared with the performance of the same specimen in dry conditions or conditions with virtually no pollution contamination. These environmental adversities have resulted in designs that promoted an increased leakage path in order to maximise the unified specific creepage distance (USCD in mm/kV).

The use of polymeric materials, such as silicone rubber, has been the state-of-the-art solution for polluted environments mainly due to their hydrophobic properties and the ability to transfer this water repellent property to the adhering surface pollutants. However, pollution problems are only partly alleviated under harsh environmental conditions.

Dry-band formation on the wet pollution layer and its role in the process of insulator pollution flashover has long been well described and understood for ceramic insulators. Especially for polymeric materials, tracking and erosion caused by discharges and the subsequent material degradation, impels a close investigation of any dry-band that may be formed in these cases. It appears that dry-bands themselves during artificial fog tests have not been demonstrated.

Unlike ceramic insulators, there is no equivalent fog test for the artificial pollution of polymeric insulators. A good understanding of the behaviour of a conventional silicone rubber insulator during a clean fog test was considered a prerequisite for a reliable comparison with the textured insulator prototypes. Therefore, the adoption of a reproducible and meaningful test procedure was a high priority for this project.

In this chapter, a modified artificial pollution test on polymeric 11kV rated insulators is presented. This fog chamber test is based on the Solid-Layer method of IEC 60507 and suggests the application of a kaolin-salt pollution slurry directly on the insulator and using a wetting agent during the insulator pre-conditioning to secure a uniform pollution layer. The test silicone rubber insulators were prepared in the laboratory using vacuum casting techniques.

The test insulator was monitored by a visual and infrared camera in parallel to compare discharge activity in the visual spectrum and dry-band formation at the infrared spectrum. Correlation of visual and infrared records aimed to provide a more enhanced insight of the pre-flashover mechanisms leading to insulation failure during a clean-fog test.

A high-resolution data acquisition system was developed using the National Instruments LabVIEW platform to monitor and store the waveforms of the applied test voltage and leakage current throughout the tests.

3.1 Experimental setup

3.1.1 The fog chamber

The insulators were tested in the fog chamber of Cardiff University high voltage laboratory (Figure 3-1). The chamber is situated in one of the three high voltage cages subdividing the laboratory. The safe access to the cage is secured by an interlock system that interrupts high voltage supply until all precaution measures have been followed. The chamber shell is made of polypropylene and the dimensions are 2m x 2m x 3m. An earthed aluminum mesh covers the chamber floor and beneath is a collection sump for accumulated water due to condensation. The sump is drained with the help of a pump. Access to the fog chamber is possible through a transparent door made of polycarbonate. The door has a rectangular opening at approximately the height of the tested sample to allow the visual and infrared cameras to record during the test.

Three pairs of spray nozzles supply the chamber with uniform fog: two pairs are located at the opposite corners of the chamber and one pair is situated on the chamber floor. An external control panel situated outside the fog chamber cage

controls the fog supply. The panel consists of controls to adjust the air pressure, the water flow rate and the spray nozzles. Indicators of the air pressure and the water flow are also installed.

The high voltage supply enters the fog chamber from the chamber ceiling. A vertical aluminum tube with stress rings at both ends, serves as the high voltage conductor. Different types of insulator terminals (cap, pigtail) can be mounted by using the appropriate mounting extension. The test sample is earthed by connecting the lower terminal at the earthed mesh. Measurement coaxial cables also have access through the lower side of the chamber walls.

Figure 3-1. Cardiff University high voltage laboratory fog chamber.

3.1.2 The test circuit

(a) The source voltage

The test circuit diagram is presented in Figure 3-2. A Hipotronics AC Dielectrics Test Set supplied the test voltage through a 150kVA, 50Hz transformer that could supply a 2A load at 50kV. The maximum voltage output was 75kV. A PLC panel controlled the voltage supply by adjusting a motorised autotransformer that set the 0-960V primary voltage. The voltage could be adjusted manually or it could be programmed to follow a predetermined voltage pattern. An embedded circuit breaker interrupted the supply in case of a flashover event. The

overvoltage protection level and the trip current for the circuit breaker could be set by the PLC panel. The overvoltage level was configured at 65kV, and the current trip level at 1A. The voltage was measured with an embedded digital display on the control panel by tapping on the transformer and also externally with a North Star VD-100 RC compensated division high voltage probe of a standard divider ratio 10,000:1 and a <1% error specification. The divider is located inside the fog chamber cage area and next to the HV transformer.

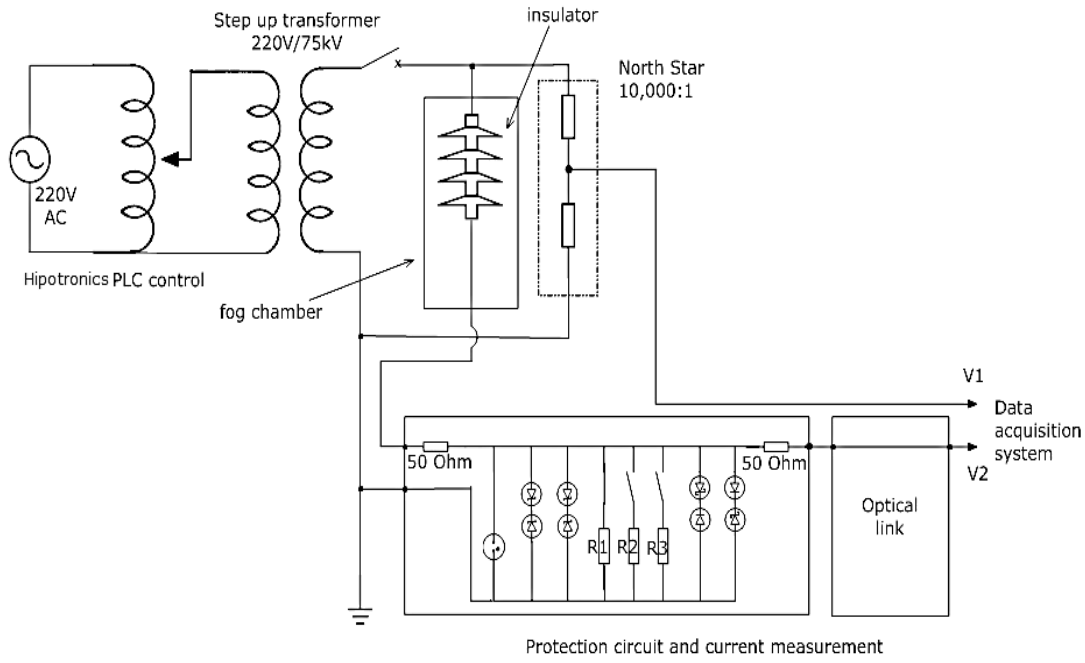

Figure 3-2. The test circuit diagram

(b) Current measurement and protection

Leakage current measurements required a circuit that could convert the current signal into a voltage signal for the data acquisition system and also protect the latter from high current events, i.e. flashover. The main aim was to acquire, along with the voltage, continuous current records from the start of the test until flashover without jeopardizing the data acquisition system electronic equipment.

For this purpose, a protection and measurement circuit was installed. The leakage current signal was produced by a measurement resistor that could be varied between the values of 4700, 1140 and 92 Ω. The resistor value could be controlled by switching in or out the resistors connected in parallel to a

permanently connected resistor of 4700 Ω (R1). Moreover, parallel branches of back-to-back high power zener diodes, branches with back-to-back schottky and fast switching diodes and a gas discharge tube were installed to suppress any fast rising voltage across the measurement resistor as a result of a high current peak or a flashover. The circuit was enclosed in an aluminium enclosure.

The output of the protection circuit was not connected directly to the data acquisition system but an optical link system intervened as a second level of protection. The voltage signal from the protection box was directed to the transmitter of a 0-15MHz Nicolet ISOBE 3000 fibre optic system which was located inside the fog chamber cage area. The receiver unit was placed outside the cage and was linked to the transmitter through the optical fibre cable. The transmitter was supplied by a rechargeable battery while a spare one could be charged the same time at the receiver unit. The voltage range could be controlled at the transmitter unit and was set to +/-10V with a DC coupling. This optical system attenuated the transmitter input signal 5 times or 10 times when the receiver output terminated at a 1 MΩ or a 50 Ω load respectively.

3.1.3 The data acquisition system

(a) The data acquisition interface

A data acquisition (DAQ) system that monitors and saves records of the applied voltage and leakage current waveforms was built. It was located adjacent to a workstation outside the fog chamber cage. The test voltage signal was acquired from the high voltage probe (North Star VD-100) and the leakage current signal from the current measurement transducer and protection system. These signals were monitored by an oscilloscope and a National Instruments PCI- 6251, 16bits, data acquisition board with the help of a SCB-68 connector block embedded in an aluminium enclosure for the physical cable connections. The board was installed at a personal computer. The connection between the connector block and the DAQ board was conducted with a SHC68-68-EPM shielded cable. The maximum sampling rate of the data acquisition board was 10^6 samples per second for multichannel acquisition that can be evenly distributed to the analogue input channels in use.

The DAQ board was controlled with a purpose-built data acquisition software programmed in LabVIEW (Figures 3-3 & 3-4).

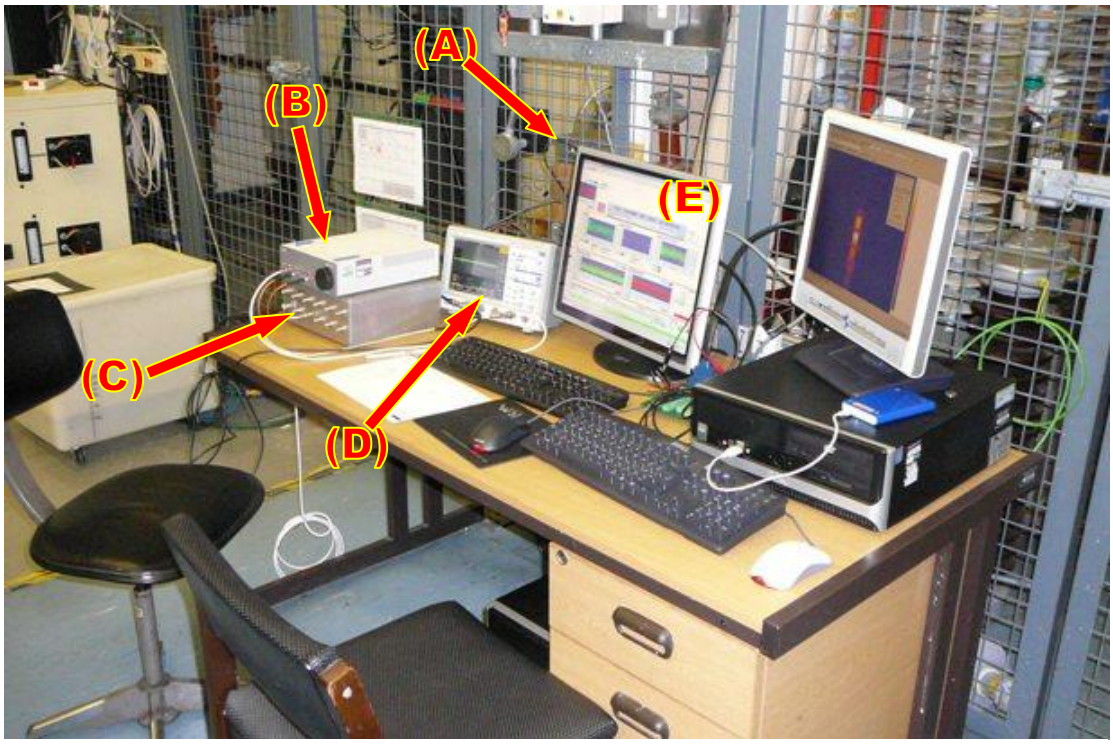

Figure 3-3. The data acquisition interface: the current measurement and protection box (A), the optical link receiver (B), the enclosed connector block (C), oscilloscope (D) and the PC (E).

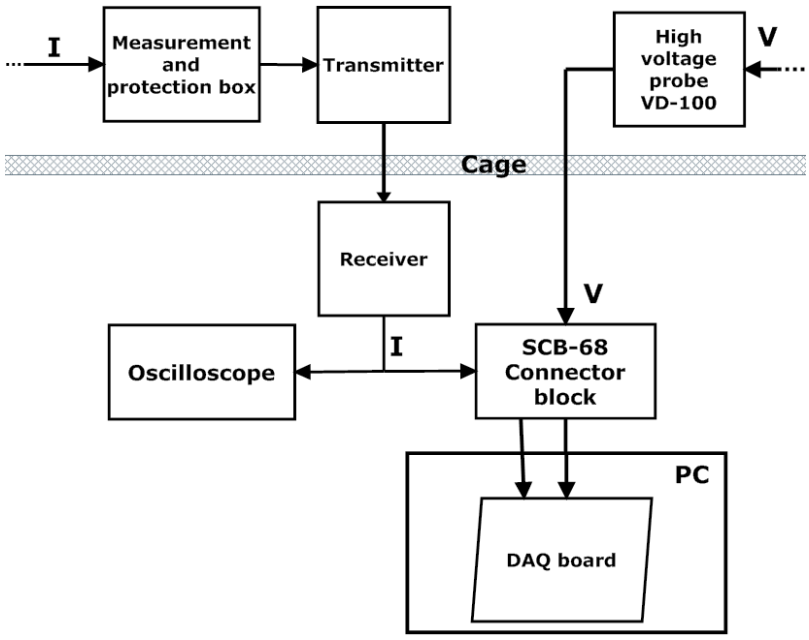

Figure 3-4. Diagram of the data acquisition system.

(b) The data acquisition software

A data acquisition software was developed for the fog chamber test series. It was based on the National Instruments LabVIEW platform and undertook the tasks of acquiring, monitoring and saving in files the waveforms of voltage and leakage current. The software was installed at the same computer which had the National Instruments DAQ board installed. The LabVIEW programme received the digitised data from the PCI-6251 DAQ board and could present the waveforms of applied voltage and leakage current and other derived electrical properties on the computer screen in a user-friendly interface.

Figure 5 shows the programme interface during a test. At the top of the screen, three graph indicators show the waveforms of applied voltage and leakage current. The third graph presents voltage and current as a pair to reveal any phase shift between these waveforms. The middle section contains two graphs

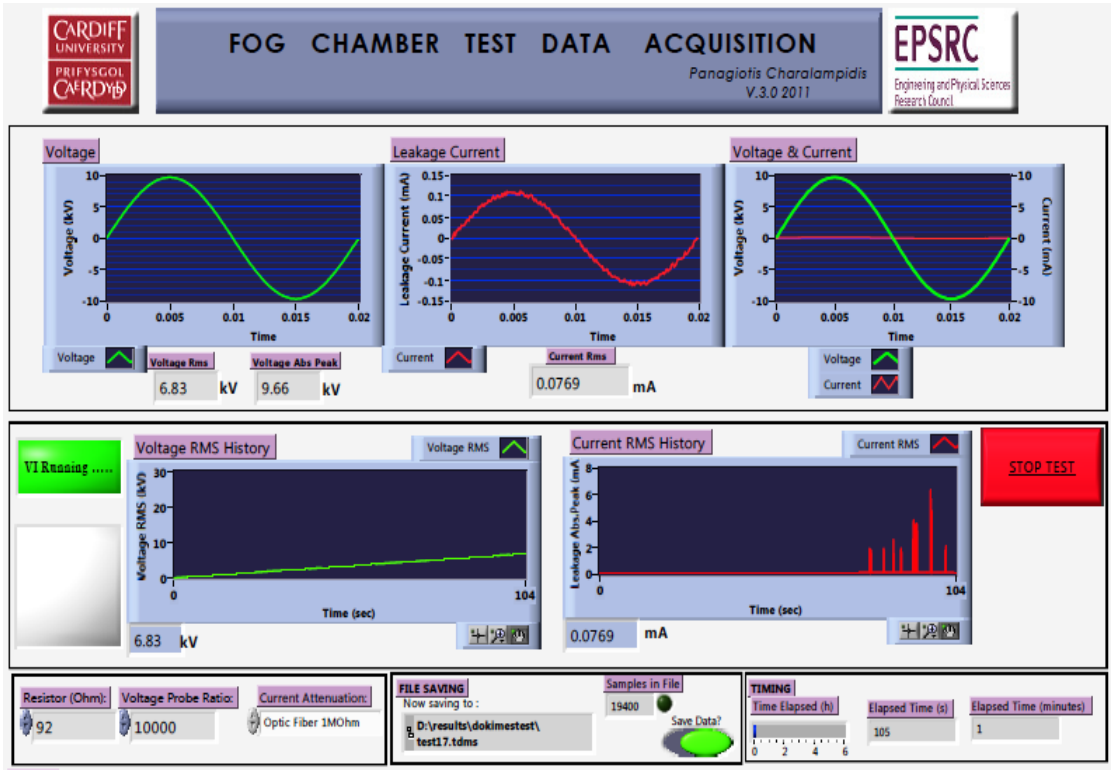

Figure 3-5. Front panel of LabVIEW data acquisition programme for the fog chamber tests series.

with the history of the root mean square values of voltage and current, which provided information of their development throughout the test. At the bottom, the interface is completed with controls to set the values of the measurement

resistor, the high voltage probe ratio, the optical link attenuation, and indicators of the elapsed test time and the file saving function.

The chosen sampling rate was 10^4 samples per second for each of the two analogue channels of the DAQ board that acquired the voltage and current signals. The time increment between two acquired samples was 100μs. For the power frequency of 50Hz, each cycle consisted of 200 samples. A high speed and high resolution acquisition was achieved by implementing Producer/Consumer programming architecture and fast data streaming TDMS files. The saving function of the programming code was based on a State Machines programming logic. This file saving code opened a file and saved data at a high speed. As soon as the file had stored 60 ksamples (corresponding to 6 seconds of real time test) for each channel, the file closed automatically and a new file opened, ready to store the new incoming samples. The use of LabVIEW features like the Queue/Dequeue functions secured the reliable and continuous saving during the transition of closing one file and opening a new one. As these records were segments of voltage and current waveforms, a separate post-processing programme was developed to assess and analyse the information acquired during testing.

(c) The post-processing software

A post-processing LabVIEW programme was developed to analyse and extract information from the file segments saved by the data acquisition system during the fog chamber tests.

The programme accessed concurrently the voltage and current records. After defining the location of the source folder containing the data acquisition records and also defining the target file for saving the new processed data, the software located the first file to be read. Data were accessed in sets of 200 samples: as soon as 200 samples (one cycle for 50Hz) of voltage and current waveforms were extracted, calculations over these samples were performed to calculate other electrical characteristics. These were the root mean square and absolute peak of voltage and leakage current, the average power, energy and accumulated energy.

After these newly calculated properties were saved in the target file, the programme continued to access the next 200 samples and perform the next calculations. This was repeated until all $60x10^3$ samples of the source file have been processed and then the next file was accessed. At the end, the target file contained all the new processed data of which each sample (or graph point) was the result of a calculation performed over a single-cycle time window of the raw source data. Analysis could also be performed at any user-defined time window. The graphical interface of the post-processing programme was arranged in tabs (Figure 3-6). The front panel tab contained the main settings for the data mining of the source files. At the upper left side, the range of files that was required to be read could be defined.

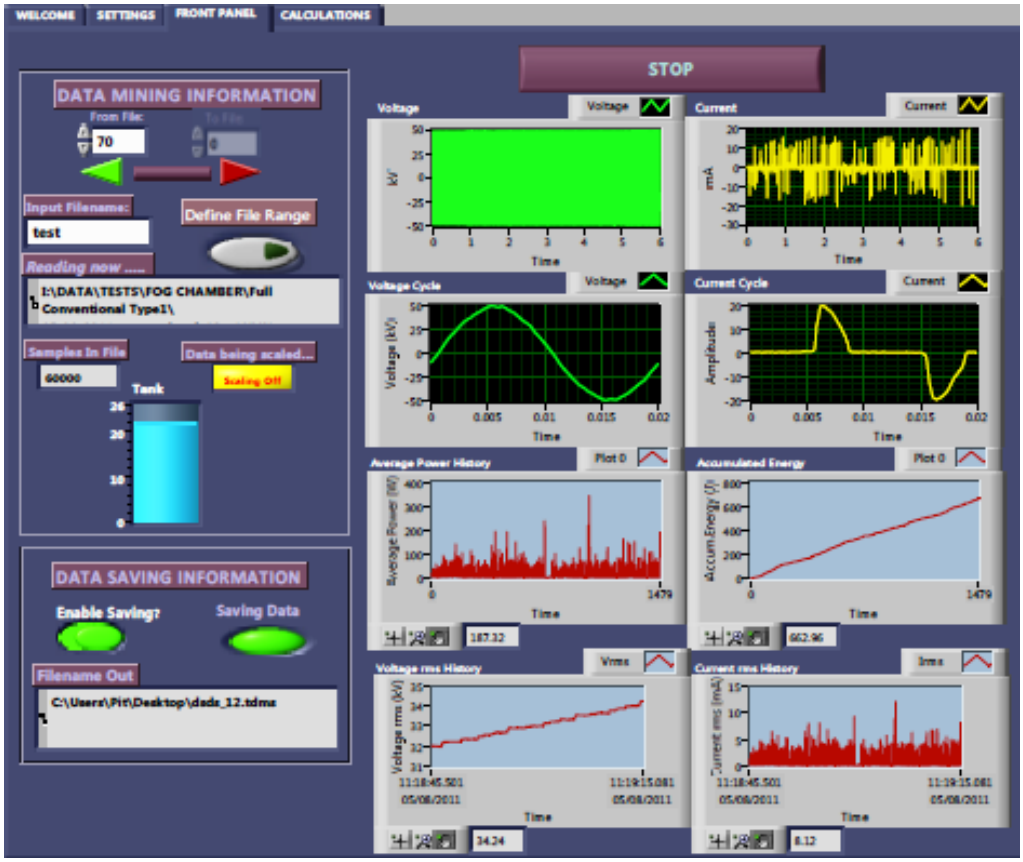

Figure 3-6. Front panel of the data post-processing programme.

There were are also information indicators showing the path of the source file that was currently processed, the path of the target file, and indicators prompting the user to save the processed data.

The software calculated the *root mean square* of the voltage (and current) signal for one cycle according to the formula:

$$u_{rms}= \sqrt{\frac{1}{N}\cdot\sum_{n=1}^{N} u_n^2} \tag{3-1}$$

where N is the number of samples per cycle (200 samples for the current work). The same formula applies for the calculation of the root mean square of current.

The *absolute peak* of the voltage and current signals for one cycle, $|v_{peak}|$ and $|i_{peak}|$, was computed by calculating the absolute values of all cycle samples and detecting the greatest value.

The *average power* was calculated by multiplying sample by sample the cycles of voltage and leakage current. The resulting array is an array of products, each one of them expressing the instantaneous power:

$$p_n = v_n \cdot i_n \tag{3-2}$$

where v_n and i_n are single samples of the voltage and current signals respectively. The average power for one cycle was then calculated as:

$$p_{av}= \frac{1}{N}\cdot\sum_{n=1}^{N} v_n \cdot i_n \tag{3-3}$$

The *energy* per cycle was calculated by multiplying the average power with the cycle period.

$$e_{av}= p_{av} \cdot \mathrm{T} \tag{3-4}$$

where T is the cycle period, 20ms for this work. The *accumulated energy* was the summation of the cycle energy for all recorded cycles:

$$e = \sum_{k=0}^{K} e_{av_k} \tag{3-5}$$

where K the total number of captured cycles and e_{av_k} is the average energy of the k^{th} cycle.

3.2 Test insulators

The test insulators were cast in the high voltage laboratory. The housing was made of room temperature vulcanised, two component, silicone rubber (RTV-2). The housing was cast over a glass fibre core with metal terminals attached on each end. Some insulators were cast over a polyether ether ketone (PEEK) core, also manufactured in the high voltage laboratory.

Two types of conventional insulators of different profile were manufactured: Type 1 and Type 2. Both profile designs are based on commercially available insulators. Type 2 is characterised by a longer creepage distance and bigger sheds than Type 1. Also, Type 2 shank diameter does not remain the same for all sections, but the middle section has a smaller diameter. Figure 3-7 shows both insulators and their dimensions.

Two commercial silicone rubber materials were used for the manufacturing of the test insulators. For the purpose of this work, they were named material A and material B. Type 1 insulators are noted by the letters CON followed by the letters 'A' or 'B' to indicate the housing material. Type 1 insulators were cast in both materials, CONA and CONB, while the type 2 design was made exclusively with material A.

Cylindrical prototypes, without sheds, were also prepared. These simplified samples were made of the same housing material and cast over the 134mm cores that Type 2 design utilised. Testing of such samples aimed to benchmark the moulding and testing procedures before moving to shedded insulator designs.

The polymeric housing was cast using a metal tooling fabricated by the Manufacturing Centre at Cardiff University. The steel mould was machined using electrical discharge machining (EDM) techniques and the cavity was formed by separate metal inserts mounted on the mould metal plates. Two sets of metal inserts were manufactured, one for each insulator type, thus using the same mould plates to get both design variations. A hollow channel connecting the mould exterior with the cavity, called the injection gate, is used to inject the silicone rubber during casting.

Smaller channels are constructed to ensure the venting of the cavity, thus inhibiting the formation of voids in the material caused by entrapped air (Figure 3-8). The insulator core is carefully placed in position and both mould plates are combined and secured with the help of threaded rods and bolts.

SiR insulator Type 1 design

SiR insulator Type 2 design

Dimension (mm)	***Type 1***	***Type 2***
Creepage distance (Lc)	375	530
End fitting separation (L)	175	134
Shank diameter (d)	28/42	28/42
Shed diameter (D)	90	142
Shed separation (s)	46	50
Core diameter	18	18
Form factor (F)	2.76	2.78

Figure 3-7. Test insulators Type 1 and Type 2 and their dimensions.

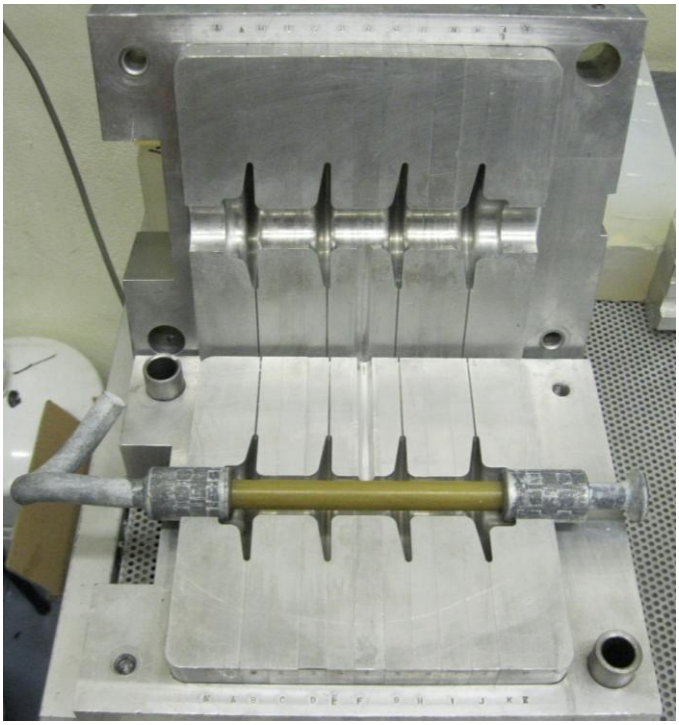

Figure 3-8. The metal mould with a fibre core in position.

The RTV silicones come in 2 parts (components), the base resin (component A) and the curative (component B). The components were mixed in a pot at a 9:1 ratio and mixed thoroughly in vacuum using a MCP 5/01 vacuum casting machine (Figure 3-9).

As can be seen on the figure, the casting machine contains two separate chambers that communicate through a control valve. This valve can isolate each chamber from the other, allowing different pressure levels to be applied to each compartment. The top chamber is where the mixing takes place while the lower chamber contains the mould.

After the removal of trapped air, the mix is ready to be injected in the mould which is already in place in the casting machine. Degassing times vary depending on the volume of the mix. For an insulator cast, it was approximately 12 minutes.

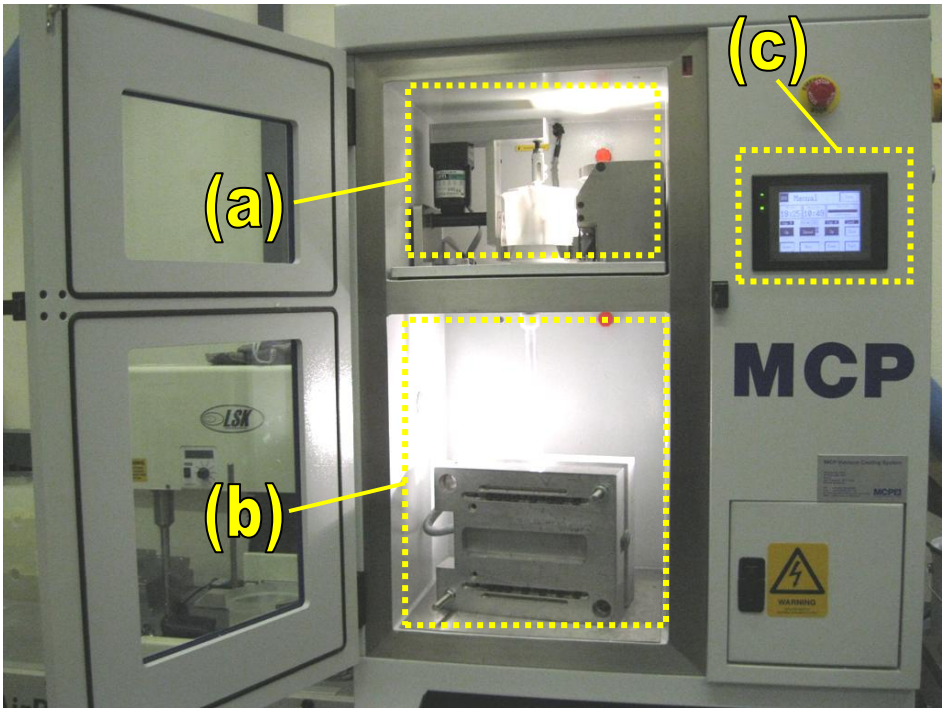

Figure 3-9. The vacuum casting machine: the top mixing chamber (a), the lower injection chamber (b), control touch panel (c).

Due to the complicated geometry of the mould cavity and the limited pot life within which the silicone mix can be worked, the injection is performed by applying variable pressure. The control valve is closed to isolate the chambers from each other. While the lower chamber, where the mould is situated, remains in vacuum. A controlled leak of air from the upper chamber allows a small pressure of approximately 25-30 mbar to grow, thus forcing the material to move in the mould cavity. Caution was taken not to apply higher pressure that could inject air through the casting funnel in the mould.

When the material fills up the cavity, it starts to emerge from the venting channels. The casting machine was then switched off and the mould placed for curing in an oven at 50^{o} Celsius for 8 hours. After the mould had been left to cool down for an hour, the mould plates were gently separated to reveal the cast. The insulator was then removed and inspected for any obvious imperfections or voids. If there was no problem, it was left for another 24 hours in room temperature or 2 hours in 50^{o} Celsius to make sure that the cross-linking of the polymer had been completed.

Any extra rubber material that was attached to the cast, due to the material filling the injection gate and the venting channels, was removed with a sharp scalpel. The insulator was gently cleaned with warm water and allowed to rest for another 1-2 days and then it was ready to be tested.

The metal end-fittings of the insulator cores came in two designs: pigtail and pin design (Figure 3-10a) and socket and pin design (Figure 3-10b). The glass fibre cores had attached fittings made of stainless steel while the PEEK cores fittings made of aluminium. Due to the poor adhering properties of silicone rubber to metal surfaces, a special adhering primer was used to precondition the metal fittings to achieve a firm bonding between the terminals and the polymeric housing.

More details about the casting procedure of the silicone rubber insulators can be found in the Appendix.

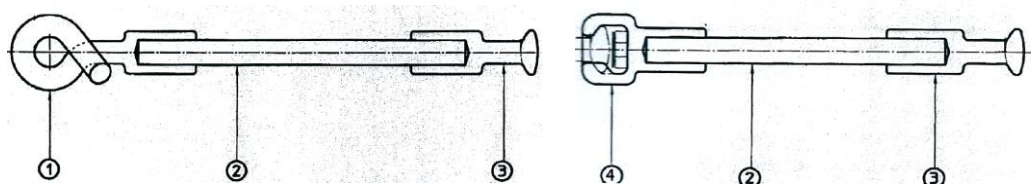

(a) (b)

Figure 3-10. End fittings designs: pig and pin design (a) and socket and pin design (b). Pigtail (1), core (2), pin (3) and socket (4).

3.3 Camera recordings

An FLIR A325 camera was employed to map the thermal stress on the insulator surface during the fog chamber test and detect the formation and development of dry-bands. The camera detector had a spectrum range from 7.5 to 13μm with an infrared resolution of 320x240 pixels. The maximum imaging frequency was 60 Hz that could also be adjusted to a lower, user-defined level. It was mounted on a tripod and placed outside the chamber monitoring the insulator through the rectangular opening of the chamber door. An Ethernet link with a personal computer established the communication with the FLIR ThermaCAM Researcher software that processed and stored the captured infrared records and also

allowed control operation of the camera. The file format was .SEQ files that could be dynamically post-processed retrieving most real-time data.

In parallel with the infrared camera, a Sony Handycam was used to capture visual records of the discharge activity during the test. These records were used to associate arc discharging that could be seen with a naked eye with the formation and position of dry-bands as revealed by the infrared recordings. For a close-up investigation of dry-bands, a Nikon D700 digital camera with 200mm focal length was used with a long exposure time setting to capture low-luminosity discharges across the dry-band.

An air fan was directed at both infrared and visual cameras to inhibit condensation of the escaping fog on the camera lenses that could damage the equipment.

3.4 Artificial pollution testing of insulators

There are no international standards for the pollution testing of polymeric insulators. A test procedure using a kaolin/salt pollution suspension with the addition of Triton X-100 non-ionic agent is presented. The test voltage was controlled by the Hipotronics PLC unit and was programmed to produce different voltage patterns to assess the flashover performance of the insulator, dry-band development and the pollution layer behaviour under fog wetting conditions.

3.4.1 Pollution suspension

A pollution suspension consisting of tap water in which sodium chloride was added to achieve a volume conductivity value of 11.2 S/m, 1 g/l of non-ionic wetting agent Triton X-100 and 40 g/l kaolin as the non-soluble component, was prepared (Figure 3-11). This value of volume conductivity was selected as a value representing heavy pollution conditions according to Table 3 in clause 13.2 of the IEC-60507 standard. In a few cases, a pollution slurry with a volume conductivity of 4 S/m was also prepared to investigate the effect of salt concentration. The volume conductivity of the pollution slurry was also used to express the severity of the test insulator contamination.

Figure 3-11. Kaolin and sodium chloride suspension with Triton X-100 wetting agent.

3.4.2 Pollution application

The clean insulators were contaminated by pouring the pollution slurry thoroughly ensuring that all surfaces have been covered with the contaminant. Then, the insulator was left to dry vertically for at least 24 hours. The effect of hydrophobicity recovery was not investigated in this work but insulators were normally tested within 48 hours after they were polluted. The insulators were visually inspected after drying to confirm that a uniform solid pollution layer was formed. The insulator was then mounted in the fog chamber, ready to be tested (Figure 3-12).

3.4.3 Fog air pressure and flow rate

The fog air pressure and flow rate were controlled by the external fog generation control panel. According to the international standard for ceramic insulators, the fog rate should be such that maximum conductance of the pollution layer is achieved within 20-40 minutes from the moment fog is applied in the fog chamber. For this reason, low voltage tests were performed to define an acceptable fog rate for the examined silicone rubber insulator. Different fog generation rates were used to investigate the effect of pollution layer wetting rate.

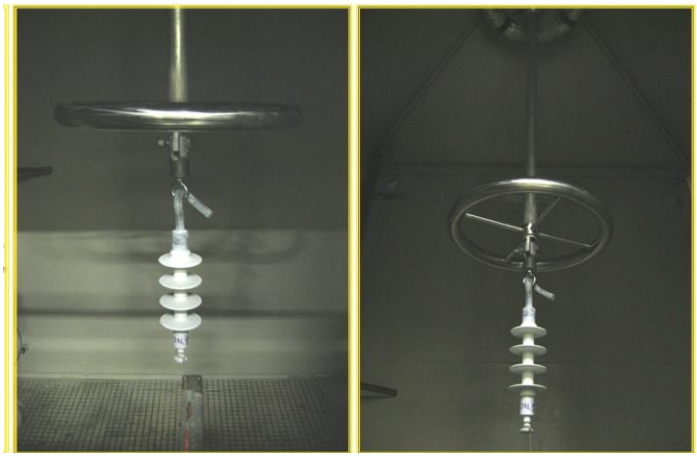

Figure 3-12. Silicone rubber insulator mounted in the fog chamber ready to be tested: side view (left) and bottom view showing the chamber ceiling and the high voltage electrode.

3.4.4 Fog tests of cylindrical prototypes

A series of tests were performed for cylindrical samples without sheds (Figure 3-13). These early stage tests were useful to establish a comprehensive test procedure and to explore the capabilities of the infrared camera in detecting dry-band formation and development. The test sample was tested in the fog chamber with a fog rate of 3 l/h and pressure 35 psi, and it was polluted with a pollution slurry of volume conductivity 0.3 S/m. The voltage was increased in steps manually with a rate of 2kV every 5 minutes, and the sample was monitored by the infrared camera throughout the test until flashover. These prototypes were manufactured using special silicone rubber moulds, as described in detail in Chapter 5.

Figure 3-13. Cylindrical silicone rubber prototype with no sheds.

3.4.5 Low voltage fog test

The polluted silicone rubber insulator was placed in its test position in the fog chamber. The test sample was monitored by the infrared camera. The test voltage was constant at 0.87kV, which is the minimum output of the Hipotronics power supply. The fog was applied simultaneously with the test voltage. The data acquisition system monitored the development of leakage current as the pollution layer gradually became wet. The fog input rate should be sufficient to achieve the maximum value of layer conductance within 20-40 minutes from the fog application. It was very important to ensure that no drying of the pollution layer, due to power dissipation, happened during the low voltage test. For this reason the insulator was constantly observed with the infrared camera to detect any surface heating.

3.4.6 Clean insulator fog tests

A Type 1 insulator was tested clean, without applying pollution on its surface. The applied fog rate was generated with water flow of 6 litres/hour and an air pressure of 35 psi. The purpose of this test was to assess the behaviour of a clean silicone rubber insulator in clean-fog conditions and to map its thermal profile to compare with the performance of the same sample with a solid pollution layer. The infrared and visual cameras probed the insulator throughout the test while the LabVIEW data acquisition software recorded continuously the signals of voltage and current. As these were initial tests, non-standard protocols were followed: after 15 to 18 minutes at 0.87 kV at the start, the test voltage is gradually increased at steps of 4kV up to a magnitude of 25 kV. However the test voltage did not exceed 60 kV to protect the measuring equipment and the sample from unnecessary damage that could be inflicted by a high current flashover arc.

3.4.7 High voltage fog tests with ramp control

The high voltage tests were performed to investigate the flashover performance of the silicone rubber insulator and the dry-band development along with the associated discharge activity. The pollution severity was measured and expressed as the volume conductivity of the kaolin/salt suspension used to pollute the insulator surface.

(a) Test protocol

An AC 50Hz test voltage was supplied using the Hipotronics motorised power unit that could be programmed using the control unit. The rms voltage followed automatically a ramp pattern with a rate of increase approximately 4kV/min. This rate was chosen so that flashover could be achieved within 5 to 10 minutes. The voltage supply could be manually interrupted or it was interrupted by the embedded circuit breaker upon an overcurrent event (flashover). Fog generation in the chamber was initiated simultaneously with the application of the test voltage and ran uninterrupted for the full length of the test.

The polluted test insulator was placed in the fog chamber and was monitored by the visual and infrared cameras. The nominal frame rate of the visual camera was 50 fps but to due to interlacing of the captured frames, the exported video media files had a frame rate of 25 fps. The sequential (.SEQ) files used to store the IR records demand a significant storage space. For that reason and taking into consideration that dry-band formation and development did not change rapidly with time, a frame rate of 1 fps was chosen for the infrared recording to reduce the captured data size.

The signals of voltage and leakage current were both monitored and stored using the LabVIEW data acquisition system, with a sampling rate of 10 ksamples per second for each channel, capturing 200 data points for each waveform cycle.

As soon as both test voltage and fog supplies were initiated, LabVIEW and camera recorded were also triggered to start. Throughout the test, observations on the dry-band dynamics though infrared monitoring, the spark discharge activity through the visual camera recording and the electrical properties of voltage and current though LabVIEW monitoring, were performed.

The increase of voltage would eventually lead to a flashover event which triggers the interruption of the voltage supply and the end of camera and LabVIEW recordings. However, the fog generation was kept running with no disruption. The test insulator was left unenergised for a relaxation time of 5 minutes after which a new ramp voltage was supplied and camera and electrical signals monitoring were resumed until a new flashover occurred.

The choice of the ramp and fog conditions was based on the variability of the test data.

(b) Reproducibility of test data

A full ramp series consisted of a number of flashover shots ranging from 4 to 12 flashovers. In the initial tests, the need for establishing a comprehensive test procedure and investigating the effect of layer wetting and pollution washing off on the flashover voltage, long ramp series were performed usually consisting of 12 flashovers. These tests anticipated that as the pollution layer would be gradually washed off, the insulator surface and the flashover voltage would increase due to the decrease of the layer conductance. In this case, the flashover performance of both conventional and textured insulators would converge to a steady level. The results will be described in Chapter 4.

For later tests, the flashovers per ramp series were reduced to 4 flashovers. This decision was based on the hypothesis that the first four flashovers are the most important in terms of defining the flashover performance as it replicated more realistically the wetting conditions for an insulator in service e.g. a morning mist or fog slowly wetting the pollution layer on the insulator surface.

It must be noted that investigating the flashover performance in such tests and especially for dynamic hydrophobic surfaces like silicone rubber, is a particularly difficult task as a number of parameters can effectively alter the test conditions. Environmental conditions (atmospheric conditions such as fog temperature, atmospheric pressure or air density) can vary, and/or the pollution layer status during the ramp test may profoundly change during the test due to pollution washing. The application of the kaolin/salt pollution during the preparation of the insulator before testing is inherently variable, and may result in a pollution layer that is not identical to the one applied for past tests. Therefore, a test sample is not exactly the same for each ramp test and is not even the same for each flashover shot during the same ramp series.

In these test series a considerable number of tests aimed to achieve good statistics and establish trends and behaviour during the ramp tests by varying some of the test parameters. As a result, the ramp test conditions followed were:

- Ramp tests with a high level of pollution and high fog rate (11.2 S/m and 8 litres/ hour)
- Ramp tests with a high level of pollution and low fog rate (11.2 S/m and 3 litres/hour)
- Ramp tests with a low level of pollution and high fog rate (4.0 S/m and 8 litres/ hour)

3.4.8 Constant voltage tests

(a) Test protocol

Unlike the ramp voltage tests, the constant voltage tests were performed at a steady voltage level in order to simulate line conditions. The insulators were placed in the fog chamber and were subjected to a constant voltage level. If a flashover occurred within 30 minutes from the application of the test voltage, the test was repeated immediately but with the voltage level reduced by 2 kV. The test was completed when the insulator managed to withstand the stress for 30 minutes, marking a withstand (WS) voltage level. The corresponding minimum flashover voltage was calculated as the withstand voltage increased by 1 kV.

Current and camera recording were employed in the same manner as described for ramp voltage tests. The constant voltage tests were performed under conditions of high pollution, 11.2 S/m, and low fog rate 3 litres/ hour.

(b) Selection of start voltage level

The selection of the start voltage level was established by assessing the results of the ramp voltage tests. This start voltage level should lead to flashover of the insulator but, at the same time, it should not differ significantly from the expected withstand voltage that could expose the pollution layer to extensive washing. By exploring the minimum flashover points of each ramp test, it was decided that the optimum start voltage was 30 kV for conventional insulators.

Performing the test starting with low voltage levels and increasing in steps until a flashover event occurred was reviewed. This method was rejected and abandoned because the prolonged exposure of the pollution layer and the

washing effect of the chamber fog would have produced optimistic flashover levels and would be more time consuming.

3.5 Summary and conclusions

The test methods for ceramic insulators cannot be applied in the case of polymeric insulators mainly because of the dynamic hydrophobic properties. There are currently no international standards for the artificial pollution test of polymeric insulators.

A proposed artificial pollution test procedure has been presented. The test method is based on the IEC-60507 Solid Layer method. The insulator is polluted with a kaolin/salt slurry with the addition of a non-ionic wetting agent as proposed by Swift et al. [2.13]. The insulator surface is covered with a solid pollution layer and is tested in a clean-fog chamber.

A series of tests are proposed for the estimation of the flashover performance of 11 kV conventional silicone rubber insulators. Moreover, the effect of pollution severity and the rate of the pollution layer wetting rate is investigated. The high voltage tests are performed by applying either a steadily increasing voltage of a ramp pattern or by applying constant voltage levels.

A data acquisition system was built to monitor and store in files the waveforms of applied voltage and leakage current until flashover. A separate post-processing software was developed to analyse the acquired data to investigate the development of voltage and current throughout a clean-fog test and to calculate other electrical properties deriving from these data.

Digital camera and infrared camera recording is also employed to monitor the discharge activity on the insulator surface and to explore whether dry-band formation could be detected and correlated with such discharges and the voltage/current records.

The test samples were cast in-house using vacuum casting techniques. Two types of insulators, Type 1 and Type 2, were manufactured of different profiles. Their designs were both based on commercially available insulators. Two types of commercially available two-component silicone rubber materials, material A

and material B, were used to manufacture the insulator housing of the Type 1 variation while Type 2 insulators housing were exclusively manufactured using material A. Cylindrical samples, with no sheds, were also prepared to perform preliminary tests and to optimise the casting techniques later employed for full, shedded insulators.

A good understanding of the behaviour of conventional silicone rubber insulators under conditions of artificial clean-fog tests and establishing an effective casting and testing technique were essential for the development and testing of full textured insulators prototypes.

Chapter 4. Laboratory classification of dry-band formation and flashover mechanism

Introduction

In Chapter 3 the experimental techniques and test protocols for the manufacturing and artificial testing of silicone rubber insulators were presented. In this chapter, the test results of the clean-fog tests are presented.

The flashover performance of conventional silicone rubber insulators was explored. The effect of pollution severity and the pollution layer wetting rate were also investigated. These tests showed that the controlled wetting of the pollution layer and the increasing layer conductance reduced substantially the flashover voltage.

Visual and infrared photography was also employed to monitor the test sample during the clean-fog tests. Visual records showed the development of pre-flashover arcs spanning sections of the insulator shank. Infrared photography during a clean fog test provided images of the formation and development of stable dry-bands on the insulator surface which were not seen before in the published literature. These zones are characterised by negligible conductance but the current continuity is maintained by a series of streamer discharges across the bands; the current is limited by the low conductance of the pollution layer, and the surface temperature of the dry-band regions is of the order of 10^{o} C above ambient. However, higher-current partial-arcs develop frequently, occasionally bridging separate dry bands. These unstable high current partial-arcs always precede flashover.

Current measurements were performed using the LabVIEW data acquisition software. The stored records were post-processed to calculate other electrical properties deriving from the waveforms of voltage and current and to correlate them with the digital camera and infrared records. Current records confirmed the inverse relationship between the flashover voltage and the layer conductance.

4.1 Testing of cylindrical prototypes

The plain cylinder insulator was placed in the fog chamber and was monitored using the infrared camera to detect thermal stresses. The volume conductivity of the pollution slurry used to contaminate the test sample was 0.3 S/m. The test voltage was increased by approximately 2kV every 5 minutes. Figure 4-1 shows the development of the test voltage and the leakage current during the test.

After 30 minutes of testing in the fog chamber, a flashover terminated the test at 15 kV. The leakage current probe was removed 5 minutes before flashover occurred to protect the measuring equipment from the high current surge. The current reached a maximum value of approximately 7mA at 12.7 kV.

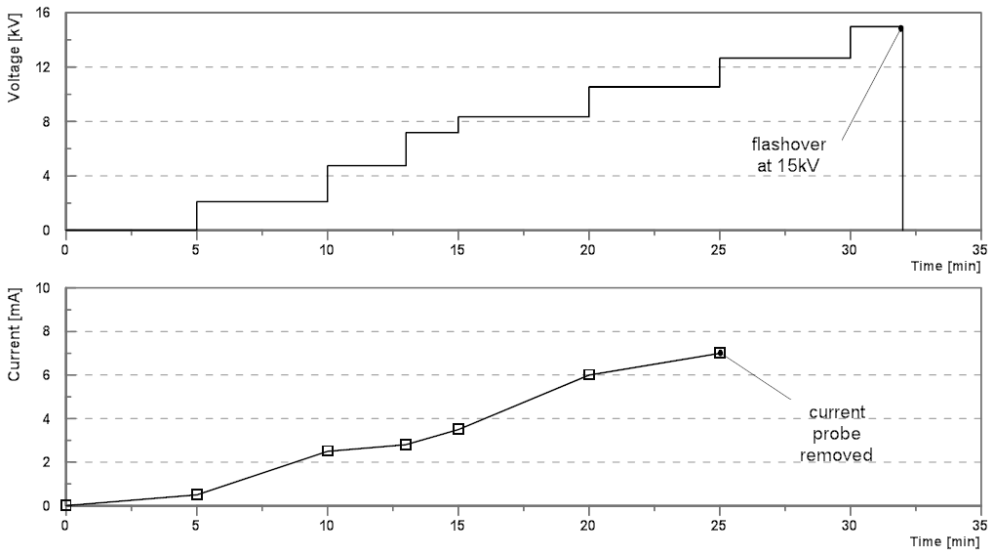

Figure 4-1. Cylindrical insulator prototype non-standard test: Test voltage and current.

Apart from calibrating the test apparatus and the data acquisition system, this test series was very useful in exploring the capabilities of the infrared camera to record thermal stresses and dry-band formation.

Figure 4-2 shows a series of infrared records at increasing voltage levels during the clean-fog test of the cylindrical insulator.

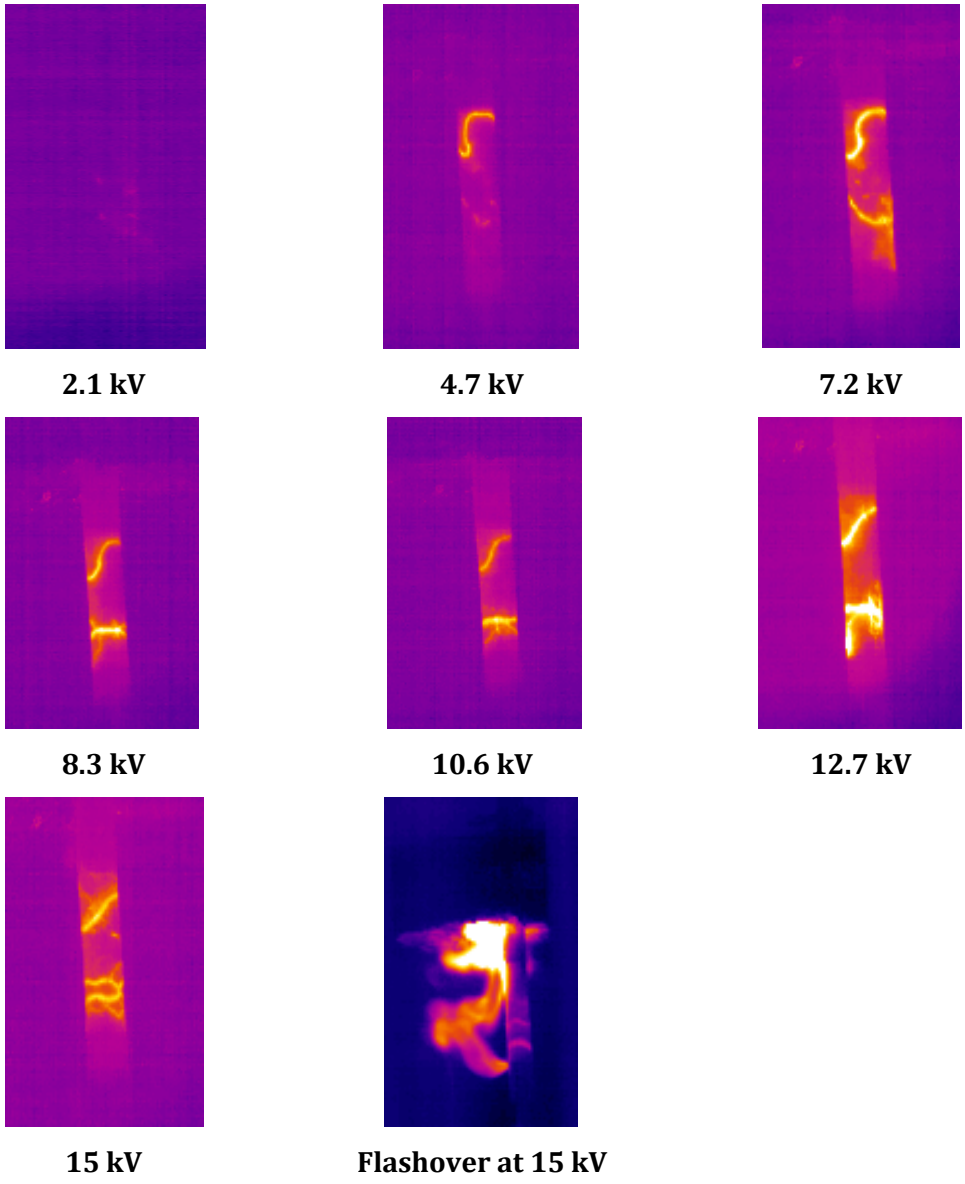

Figure 4-2. Infrared records of the cylindrical prototype and dry-band development during clean-fog test.

At the beginning of the test and with the sample energised at 0.87kV, no surface heating is detected by the infrared camera as a very small leakage current is being conducted through the pollution layer. As the voltage increases at 2.1 kV, the first signs of surface heating are picked up by the infrared camera due to the increasing conduction of the pollution layer. When the voltage is further increased to 4.7 kV, a 'ring shape' hot zone gradually develops on the sample surface, indicating the formation of a dry-band. This dry-band was not visible with the naked-eye. The temperature range measured for these dry-bands was 32 to 34^{o}C, about 10^{o}C higher than the temperature of the surrounding fog. A

close observation of the infrared records showed small discharges bridging these hot regions. At 7.2 kV, a second dry-band formed with the first one remaining active. Long spark channels were visible at this voltage level, bridging long sections of the creepage. This discharge activity became more intense as voltage increased to 12.7 kV. At 15 kV and just before flashover, a third dry-band appeared resulting in a redistribution of the test voltage along the sample which could be observed by the rather less luminous dry-bands compared with those observed at 12.7 kV and for two dry-bands present.

Cylindrical samples testing revealed that the use of the infrared camera during a clean-fog test could provide outstanding images of dry-band formation and development. This allowed a more systematic study of dry-bands and their role in pollution flashover of fully shedded polymeric insulators during a clean-fog test.

4.2 Low voltage tests of insulators

Figure 4-3 shows the conductance of the pollution layer of a Type 1, 375 mm creepage length, silicone rubber insulator for two fog rates: 3 litres/hour and 8 litres/hour.

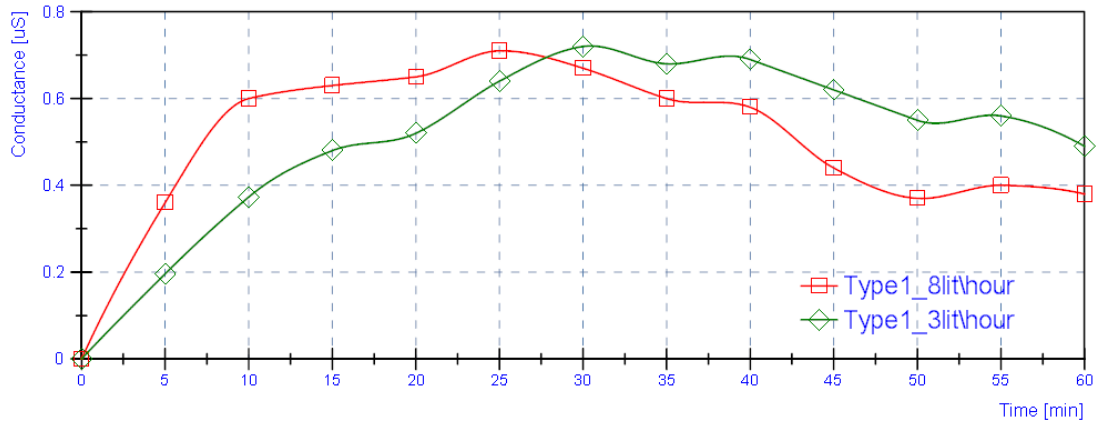

Figure 4-3. Conduction of the pollution layer for two fog rates: 3 litres/hour and 8 litres/hour.

The graphs show the gradual increase of the leakage conductance as it becomes wet and conductive due to the applied fog. The maximum conduction measured was approximately 0.7μS for both applied fog rates which would correspond to a layer resistance of 1.4 MΩ. This maximum value was reached after 20 minutes of wetting but quicker for the high fog rate than the lower fog rate.

For 8 litres/hour, the layer conduction built up rapidly during the first 10 minutes to 0.6 μS and reached the maximum value after 25 minutes. However, due to the high wetting rate, the pollution layer started to wash off from the insulator surface causing a decrease of the layer conduction to 0.43 μS.

Unlike the high fog rate, at 3 litres/hour the layer wetting was slower as portrayed by lower rate of increase of conduction compared with the case of high fog rate. Maximum conduction was observed after 30 minutes. In contrast with the high fog rate, the washing of the pollution layer is slower for the lower fog rate.

For both cases, the pollution layer conductance converged to a value ranging from 0.5 to 0.35 μS after 1 hour of testing indicating a further washing of the layer.

4.3 Clean insulator test

Figure 4-4 show the applied voltage and the leakage current during a clean-fog test with a clean insulator. The test insulator was left for 17 minutes in the fog and energised at 0.87 kV. Then, the test voltage was raised to 25 kV and increased at steps of 4kV up to 53 kV where the supply voltage was switched off to prevent the high arc damaging the measuring apparatus.

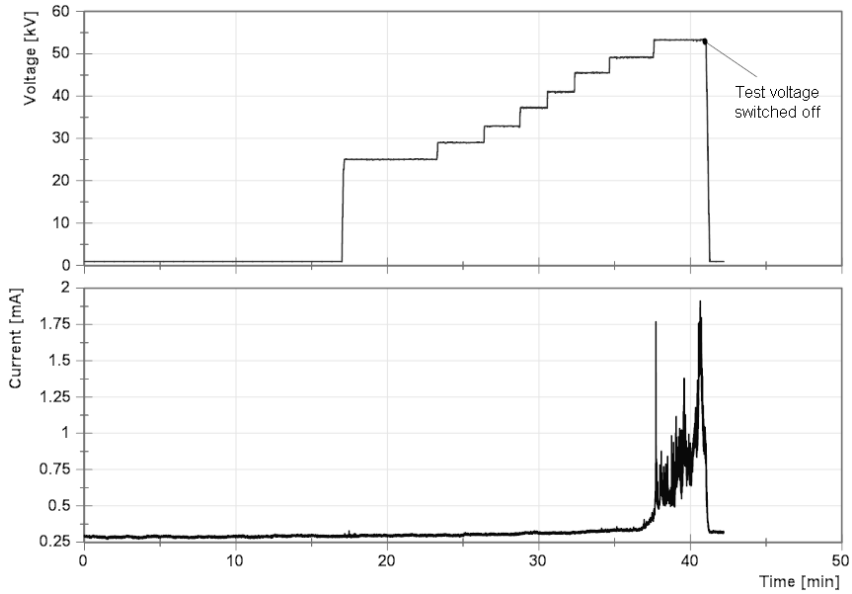

Figure 4-4. Voltage rms and current rms records for a clean-fog test of an unpolluted insulator. The test followed a non-standard protocol of voltage application as it was part of initial tests.

The insulator was characterised by a low leakage current (<1mA), and no discharge activity was observed for voltages below 40 kV. Only after 40 kV, discharge activity in the form of streamer-like discharges was detected, as indicated by the current record and the visual and infrared images (Figure 4-5).

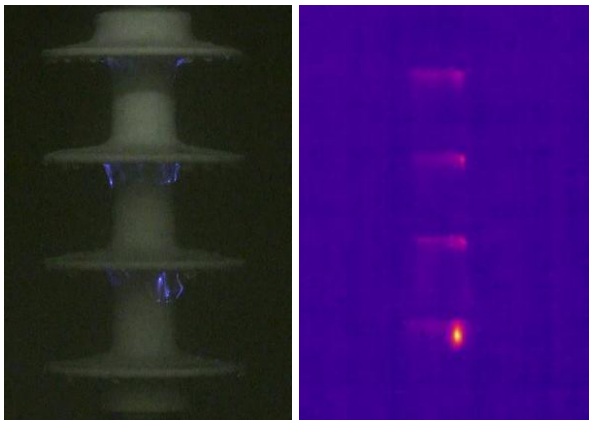

Figure 4-5. Visual and infrared records of a clean insulator at 45 kV.

For polluted insulators, unlike clean samples, the presence of a conductive wet pollution layer, the formation of dry-bands, the arc-like discharge activity and the redistribution of voltage across the length of the insulator result in a significant depression of the flashover voltage, as will be described in the next paragraph.

4.4 High voltage flashover tests under fog with ramp control

4.4.1 Flashover performance summary

The flashover performance of Type 1 silicone rubber insulator was investigated for three different condition combinations of the salinity of the pollution slurry and the fog rate supplied in the test chamber. After the completion of each ramp voltage test series, the insulator was cleaned and re-polluted for a new test series. Table 4-1 summarises the results of ramp voltage tests.

The processing of flashover data from all test series provides the largest sample space as possible. However, variations between the test series are unavoidable as discussed in section 3.4.7.b.

Table 4-1. Summary of ramp voltage tests results

	Insulator	Number of ramp voltage test series	Total number of flashovers[1]	Average flashover voltage [kV][1]	Standard deviation[1]
High pollution (11.2 S/m) and high fog (8 l/h)	CONA	5	20	28.3	4.4
High pollution (11.2 S/m) and low fog (3 l/h)	CONA	6	24	28.6	3.3
	CONB	5	20	33.3	6.0
	CON[2]	11	44	30.1	5.3
Low pollution (4.0 S/m) and high fog (8 l/h)	CONA	1	4	41.2	6.8

[1] Only the first 4 flashover shots of each ramp voltage tests series.

[2] All insulators, both CONA and CONB

4.4.2 High pollution (11.2 S/m) and high fog rate (8 litres/hour)

Figure 4-6 shows the average curve of the ramp test series for a volume conductivity of the pollution suspension at 11.2 S/m and a fog rate of 8 litres/per hour. Each ramp test series consisted of 12 flashover shots. All tests were performed using insulators made of material A, CONA.

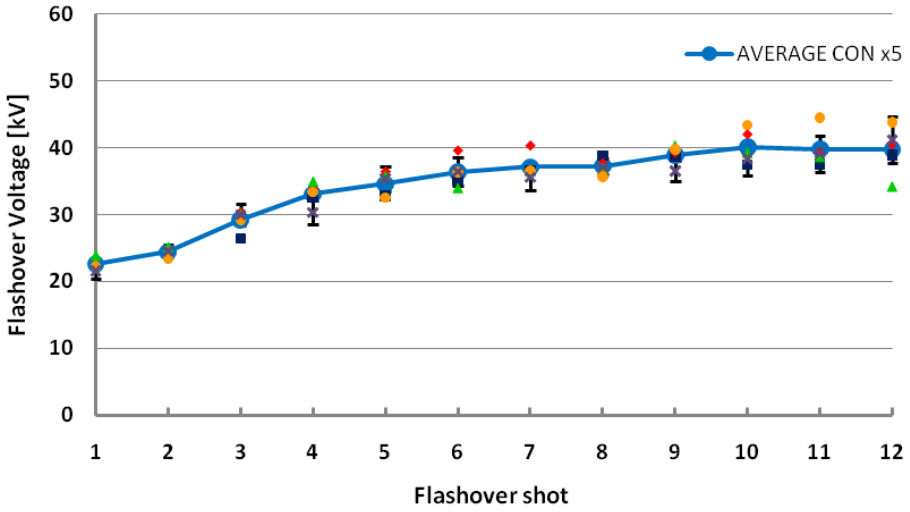

Figure 4-6. Average curve of 5 ramp voltage test series for a conventional silicone rubber insulator. Each ramp voltage test series consists of 12 flashover shots.

The flashover voltage steadily increases from 23 kV for each of the following flashover shots. However, from the 9th flashover shot, the curves became more flat and the flashover voltage remained stable in the region of 40 kV. The vertical bars represent the standard deviation of the flashover voltages acquired for each ramp test series, and they reveal a low dispersion around the average values. The maximum standard deviation, observed for the 12th shot, was 3.5 kV and the minimum standard deviation was observed for the 2nd shot, at 0.9 kV.

The shape of the average curve suggests that the insulator is most vulnerable at the 1st flashover occurrence where the minimum flashover voltage is observed, the pollution layer is fully wet and the resistance minimum. For the next flashover shots, the pollution layer was gradually washed off the insulator, thus increasing the layer resistance and increasing the level of flashover voltage. From the 9th flashover shot until the 12th shot, a significant amount of the pollution layer has been removed due to the prolonged exposure to the washing effect of the fog. Thus, the asymptotic value of 40 kV is very close to the average flashover for low pollution tests that was found to be 41.2 kV (Table 4.1).

The first 4 flashover shots are very important as they simulate line conditions where a polluted insulator in service is gradually wetted by a morning fog or mist. The average flashover voltage of all first 4 shots for all ramp voltage test series (a total of 20 flashover values) was 28.3 kV.

4.4.3 High pollution (11.2 S/m) and low fog rate (3 litres/hour)

Each ramp test series consisted of 4 flashover shots. The test was performed using both CONA and CONB insulators, thus the effect of the housing material was also investigated.

Figure 4-7 shows the average curve of the ramp test series for a volume conductivity of the pollution suspension at 11.2 S/m and a fog rate of 3 litres/per hour, for both CONA and CONB insulators.

Unlike the case of high pollution and high fog rate, the flashover voltage did not increase steadily but the test series curve had a 'U-shape' where the 2nd flashover voltage was lower compared with the 1st flashover level, only to start recovering

after flashover events 3 and 4. This behaviour was attributed to the lower fog rate that required longer time to wet the pollution layer.

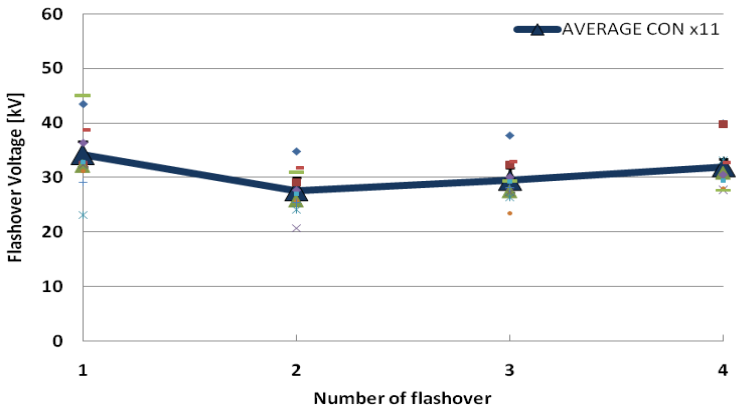

Figure 4-7. Average curve of 11 ramp voltage test series for both CONA and CONB. Each ramp voltage test series consists of 4 flashover shots.

The average flashover voltage when both CONA and CONB insulators are taken into account was 30.1 kV, compared with the 28.3 kV for high pollution and high fog rate that refers solely to CONA insulators. However, as shown by the data in table 3-1, CONB insulators performed better than the CONA insulators, as the average flashover level of the latter was 28.6 kV compared with the 33.3 kV for CONB samples (Figure 4-8). Moreover, the average minimum flashover voltage was 25.4 kV for CONA, a value close to the minimum average voltage for high pollution and high fog rate which is 22.7 kV.

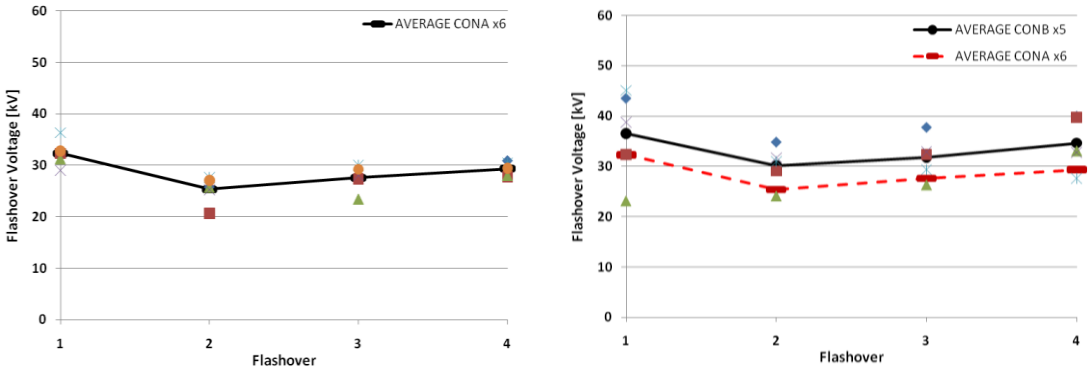

Figure 4-8. Average flashover curve for CONA insulators (left) and for CONB insulators (right) for 11.2 S/m and 3 litres/hour pollution conditions.

Unlike the case for CONA insulators, the flashover values dispersion was wider for CONB insulators. The variability of the flashover voltage behaviour of CONB insulators suggested that material B was more hydrophobic than material A, thus

inhibiting the formation of a uniform pollution layer when the insulator was polluted using the kaolin/salt suspension. The partially polluted insulator surface would include wide zones with no pollution, interrupting the layer continuity and the leakage current conduction. Leakage current and infrared records were examined, as it will be described in the next paragraph, to interpret this more unstable behaviour of material B compared with material A.

The comparison between the ramp voltage test series under conditions of 11.2 S/m for two fog rates, 3 and 8 litres/hour, and the variation of flashover voltage in a U-shape pattern, indicated the inverse relationship between the flashover voltage level and the pollution layer conductance.

4.4.4 Low pollution (4.0 S/m) and high fog rate (8 litres/hour)

In order to investigate the effect of the salinity of the pollution suspension on the flashover voltage, a ramp test series was performed on a CONA insulator with a high fog rate of 8 litres/hour, and a pollution suspension with a volume conductivity of 4 S/m, significantly lower than 11.2 S/m. The test series consisted of 12 flashovers, as shown in Figure 4-9.

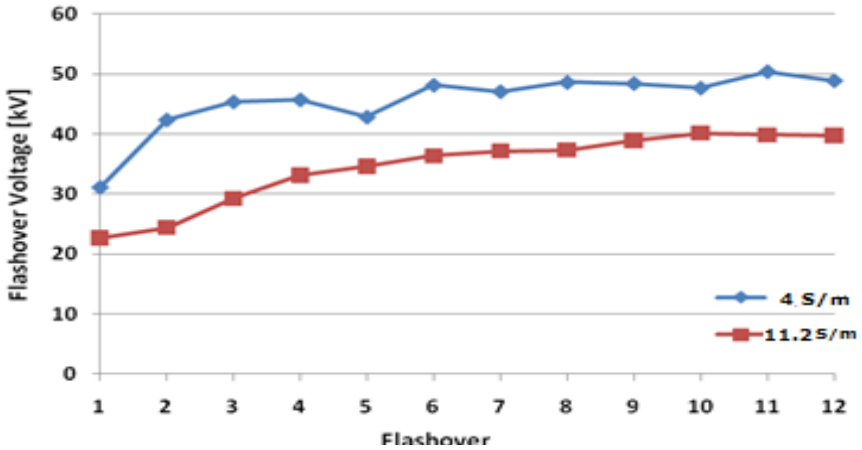

Figure 4-9. Ramp voltage test series for fog rate 8 l/h: effect of pollution severity.

As can be seen on figure, the flashover voltage for the case of 4 S/m is significantly higher compared with the average curve of 5 ramp voltage test series at 11.2 S/m for the same fog rate, 8 l/h, and the same material, CONA. This result is in agreement with the inverse relationship of the flashover level and the layer conductance which depends on the salinity of the pollution suspension.

4.5 Flashover performance under constant voltage tests

Constant voltage tests using CONA and CONB insulators were performed. Table 3-2 shows a summary of the constant voltage tests.

Table 4-2. Summary table of the constant voltage tests results.

Insulator	Number of constant voltage tests	Average withstand voltage [kV]	Average flashover voltage [kV]	Average flashover voltage for ramp voltage tests [kV]
CONA	3	22	23	28.6
CONB	2	24	25	33.3
CON[1]	5	23.6	24.6	30.1

[1] Both CONA and CONB

The average flashover voltage for constant voltage tests is lower compared with the ramp voltage tests under the same conditions of pollution severity and fog rate. The average flashover voltage for CONA was 23 kV, for CONB 25kV and the average for both CONA and CONB 24.6 kV, contrasting the 28.6 kV, 33.3 kV and 30.1 kV for the ramp voltage tests respectively.

The starting level of a constant voltage test was 30 kV and the flashover event occurred from the 10^{th} to the 29^{th} minute. However, when the insulator was subjected to a reduced test voltage of 28 kV, flashover occurred sometimes instantly upon the application of the test voltage or it occurred within the first 5 minutes from the application of the test voltage. This behaviour was observed for lower voltage levels, thus the final flashover voltage was lower compared with the flashover levels obtained with the ramp voltage test series for the same insulators.

This 'memory effect' where the insulator flashover performance is affected by the previous flashover events and the exposure time of the pollution layer in the chamber fog, were the reasons why the number of constant voltage tests were not as extensive as in the ramp voltage tests. For the same reasons and additionally because of time restraints, up-and-down test method was not adopted in this work.

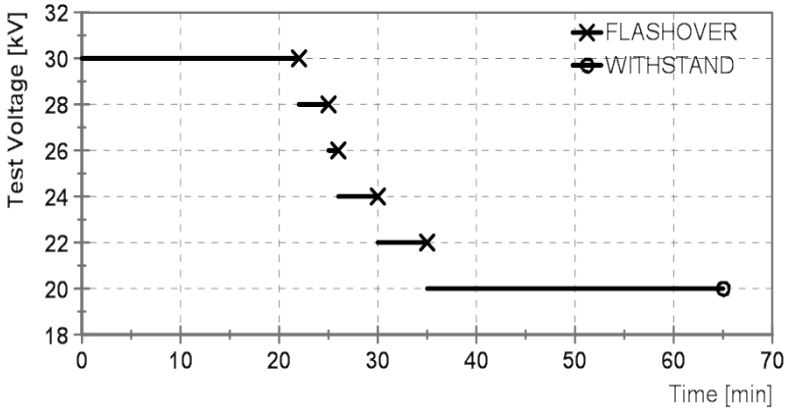

Figure 4-10. Memory effect and fall of flashover voltage level during a constant voltage test. The insulator withstood the stress for 22 minutes at 30 kV. Flashover occurred swiftly for all successive voltage levels, reducing the withstand voltage to 20 kV.

A method of avoiding the 'memory effect' could involve the testing of the insulator at one voltage level. If flashover occurs, then the insulator should be removed from the fog chamber, cleaned thoroughly, re-polluted and dried so it could be tested at the reduced voltage level. This procedure will have to be repeated until a withstand voltage is established. Such a method, except from being very time-consuming, it will also increase the probability of flashover variations due to the variations of the pollution layer itself from test to test.

The tests outcome suggested that an alternative method of a slow ramp voltage, with a rate ≤1 kV/min, could be adopted. The test voltage should reach the expected flashover voltage within 25-30 minutes when the pollution later conductance has reached its maximum value. This procedure avoids the complications introduced by successive flashover events by applying a single slow ramp voltage.

4.6 Visible and infrared photography records

4.6.1 Digital videos in the visible spectrum

The digital videos captured using the SONY Handycam digital camera provided images of the discharge activity as seen with a naked-eye on the insulator surface during a clean-fog test (Figure 4-11).

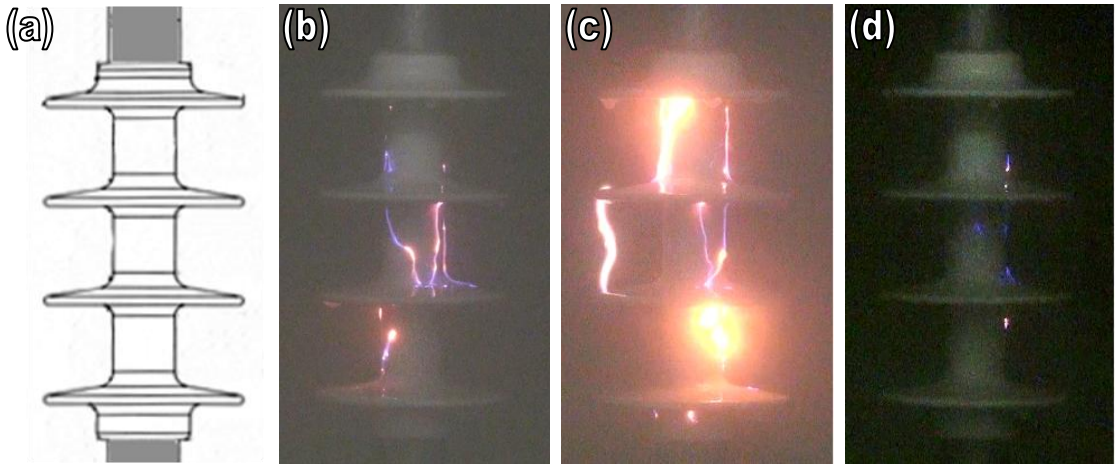

Figure 4-11. Captured digital images of the test insulator during a clean-fog test at 34 kV: (a) the test insulator design, (b) spark channels bridging sections of the insulator shank, (c) bridging of sheds caused by water droplets and (d) small streamer discharges.

Elongated spark channels were visible, bridging sections of the insulator shank. These transient events were of short duration but were repetitive and little could be seen between events. Sometimes, small blue streamer channels could be seen at the shank regions that were more visible when spark channels were not active. However, these streamers were very difficult to detect due to low visibility caused by the fog in the test chamber. Occasionally, water cascades bridged the insulator sheds, initiating a high current discharge or even could result in flashover.

It must be noted that additional discharge activity was present at the back face of the insulator that was not visible to both the digital camera and the infrared camera.

Even though the shape or appearance of the surface discharges did not provide a solid indication of an imminent flashover, the discharge activity recorded by the digital camera, seemed to be decreased before flashover. These more 'quiet' periods before a flashover event were later correlated with the current and IR records.

The presence of small streamer discharges and the more bright and elongated spark channels at the shank sections of the insulator suggested the presence of dry-bands in these regions. However, records in the visible spectrum did not provide a clear indication of the pre-flashover phenomena and mechanism. The

investigation of current and infrared records in conjunction with visible digital records provided a more comprehensive insight of the cascade of events leading to pollution flashover.

4.6.2 Infrared records

The experience gained by employing infrared photography for the monitoring of cylindrical samples, was utilised for the case of full insulators. Infrared records captured the transient heating caused by the surface discharges seen with a digital camera (Figure 4-12). But more importantly, infrared photography revealed the influence of leakage current on the pollution layer which was manifested by the presence of dry-bands that could be seen very clearly.

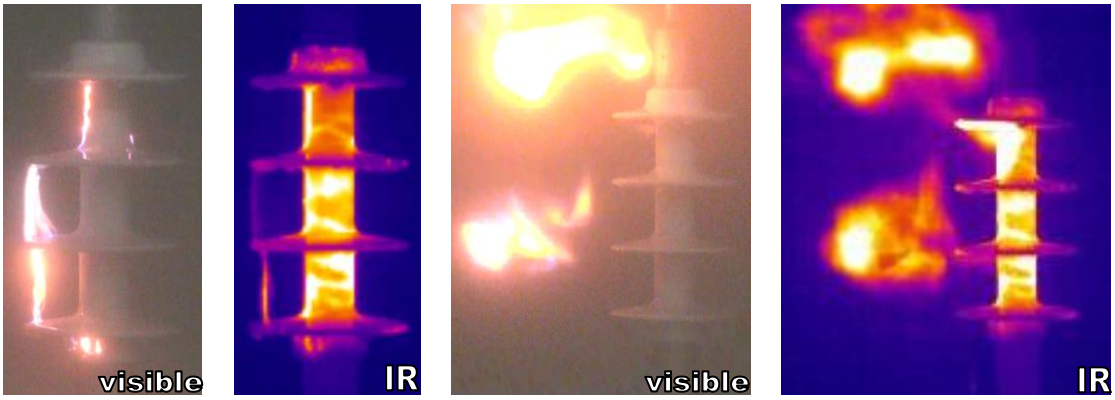

(a) (b)

Figure 4-12. Examples of transient heating captured by the infrared camera: spark channels on the insulator shank and bridging of sheds (a) and a flashover event (b).

Figure 4-13 shows a visible image along with an infrared record and the temperature profile along the axis LI01 on the insulator at 28 kV. The infrared image has been captured immediately before the surface discharges seen in the visible image.

The infrared records clearly reveal dry-bands at all three sections of the insulator shank. In this case, the top shank section has two adjacent dry-bands. The surface temperature profile along the length of the insulator shows that the dry-band regions can be as much as 5°C above the ambient 22°C. Each dry-band was found to develop, change form and fade over lifetimes of minutes (Figure 4-14).

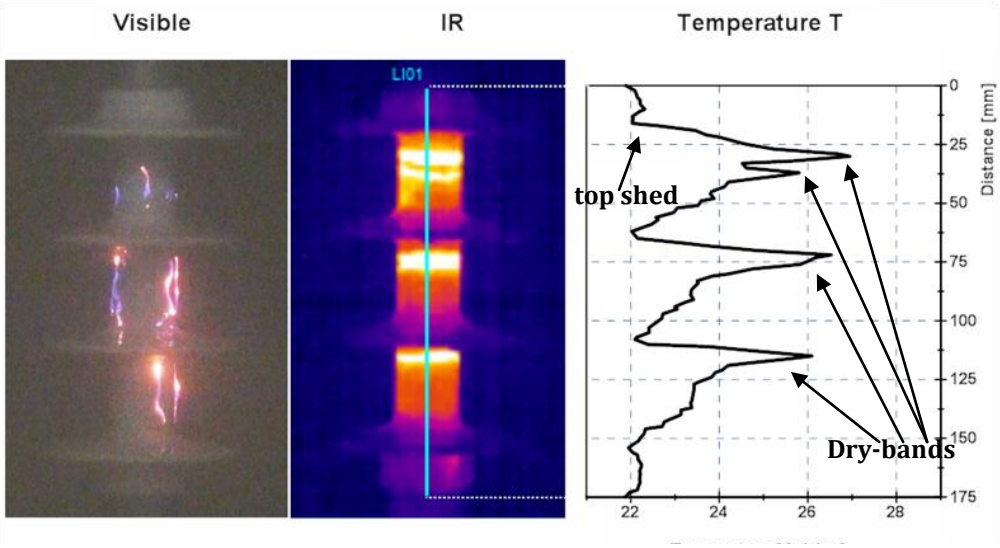

Figure 4-13. Visible image, infrared record and temperature profile on insulator at 30 kV: The infrared record shows dry-bands at all three sections of the insulator shank immediately before discharges as seen in the visible image.

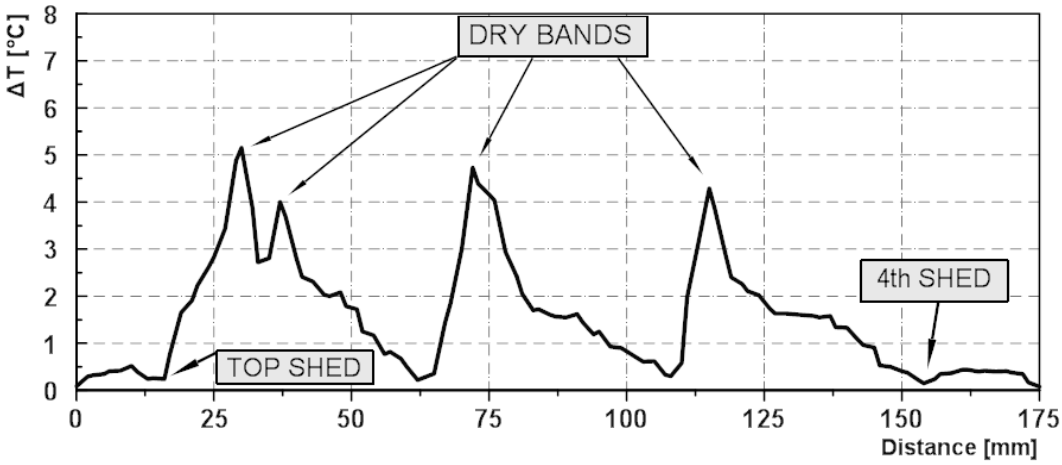

Figure 4-14. Temperature difference between the axial temperature profile and the ambient temperature 22°C.

The non-uniform leakage current conduction in the wet pollution layer causes local heating due to local power dissipation and drying on the insulator surface. Leakage current density is higher that the shank regions thus dry-bands appear in these regions. These dry zones expand until they form a 'ring' shape dry-band which interrupts the pollution layer conduction. When the voltage across the dry-bands is sufficient, they are bridged by surface discharges. The visual records captured by the Sony digital camera revealed long spark channels bridging sections of the insulators. The development and dynamics of these dry-bands were better investigated utilising the successive infrared records during

ramp voltage tests and special close-up photography using a NIKON digital camera with high exposure times.

4.6.3 Development of dry-bands with increasing voltage

Figure 4-15 shows the development of dry-bands on the insulator shank during a ramp voltage test under conditions of high pollution (11.2 S/m) and low fog (3 litres/hour).

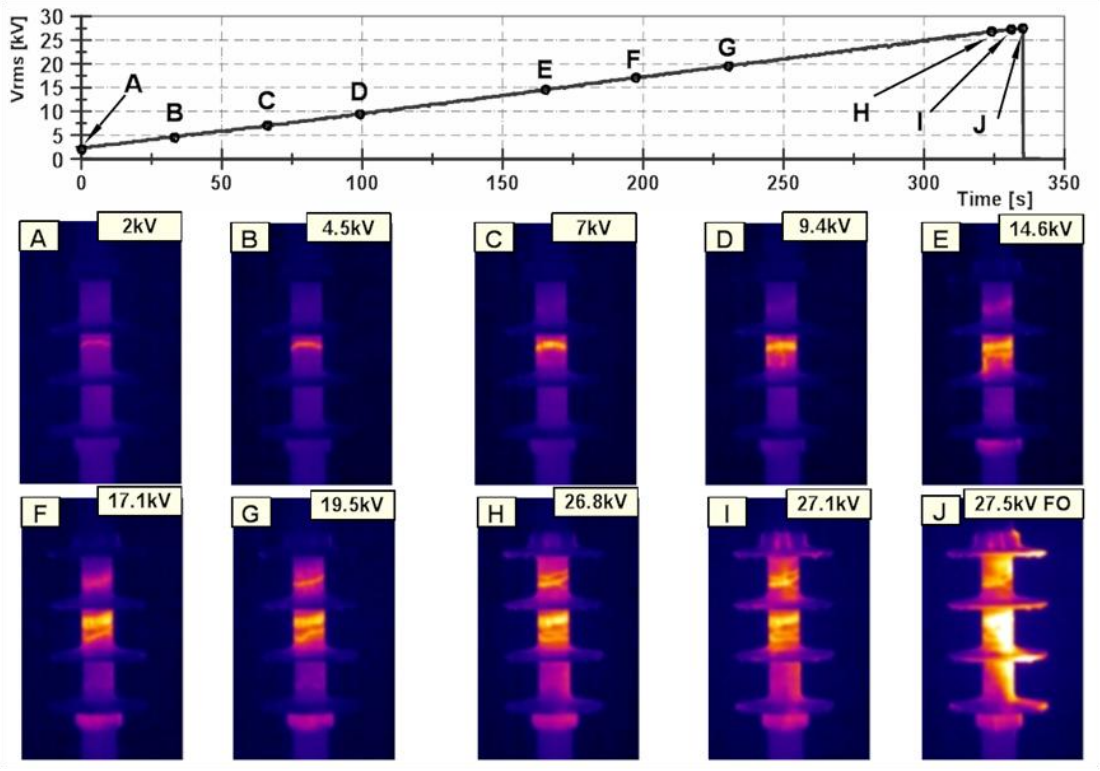

Figure 4-15. Formation and development of dry-bands during a ramp voltage test (11.2 S/m and 3 litres/hour). The width of the dry-bands is expanding as the test voltage increases with time.

A dry-band started to form in the middle section of the insulator shank at the beginning of the test and at 2 kV. This dry-band became more active and wide as the ramp voltage increased to 4.5 kV and 7 kV. At 9.4 kV, another dry-band starts to form at the top shank section while another dry-band formed very close to the pre-existing dry-band in the middle section. Moreover, local heating was detected below the fourth bottom shed but, it did not evolve into a full and luminous dry-band. Further increases of the ramp voltage from 17 kV to 27 kV was followed by even wider dry-bands and the formation of new, more narrow, dry-bands next to the existing ones whereas the lower shank section remained

free of dry-bands. Before flashover (Figure 4-15 H and I), the dry-bands seemed to be at their maximum expansion leading to a flashover at 27.5 kV.

Even after flashover, the pre-flashover temperature profiles persisted for some time. However, dry-bands became less luminous right after the interruption of the test voltage. Moreover, the dry-bands were present during the early stages of the ramp test, without any visible spark channels spanning sections of the insulator. Some discharge activity was detected on the dry-bands by the infrared camera but it was difficult to distinguish them clearly as these discharges were not hotter than the dry-band itself. As described already, the visible records of the digital Sony camera showed some streamer discharges at the shank sections (Figure 4-11d). All the above information indicated the presence of local discharges spanning the dry-bands and maintaining them active, without necessarily the presence of longer and brighter spark channels.

4.6.4 Close-up photography of dry-bands

An insulator was polluted with a pollution suspension of volume conductivity 11.2 S/m and was suspended in the fog chamber. The fog rate was set to 3 litres/hour at an air pressure of 42 psi and the test voltage was raised manually to 16 kV. The test sample was monitored by an infrared camera to detect the formation of dry-bands. In parallel, a Nikon D700 digital camera with a zoom lens was used to photograph pre-spark discharges bridging the dry-bands. The camera was set to capture images in different exposure times to acquire the clearest images possible (Table 4-3).

Table 4-3. Nikon D700 settings

Camera model	**Nikon D700**
Effective pixels	12.1 million
F-stop	f/2.8
Exposure time	1.60 sec to 30sec
ISO speed	ISO-200
Exposure bias	0 step
Focal length	200 mm
35mm focal length	200 mm

Figure 4-16 shows the insulator photo reference, the close-up digital image and the IR records of the insulator. The Nikon camera was set to 15 seconds exposure time.

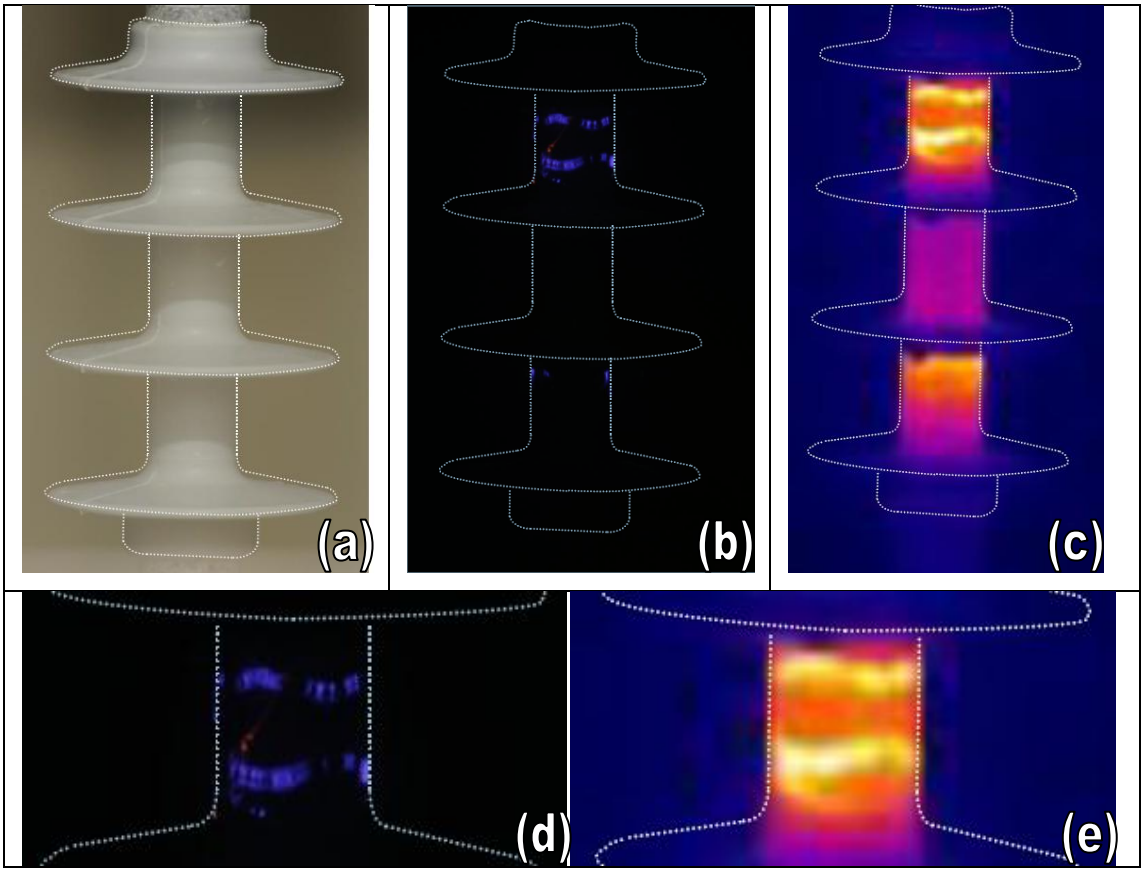

Figure 4-16. Reference picture of the test insulator (a), close-up picture of the discharges bridging 3 dry-bands on the insulator shank (b), infrared record showing the position of the dry-bands and zoomed section of the digital and IR records (d & e).

The close-up image clearly showed a series of streamer discharges bridging the dry-band when no spark channels are present. These discharges did not take place simultaneously but only few of them spanned the dry-bands at the same time. This was in agreement with the few streamer discharges that were detected by the Sony digital camera on the insulator shank.

Figure 4-17 shows another image of dry-band streamer discharges along with spark discharges for 30 seconds of exposure time. The position of the dry-bands as indicated by the infrared record, matched the position of the streamer discharges as seen by the close-up visible image (Figure 4-18).

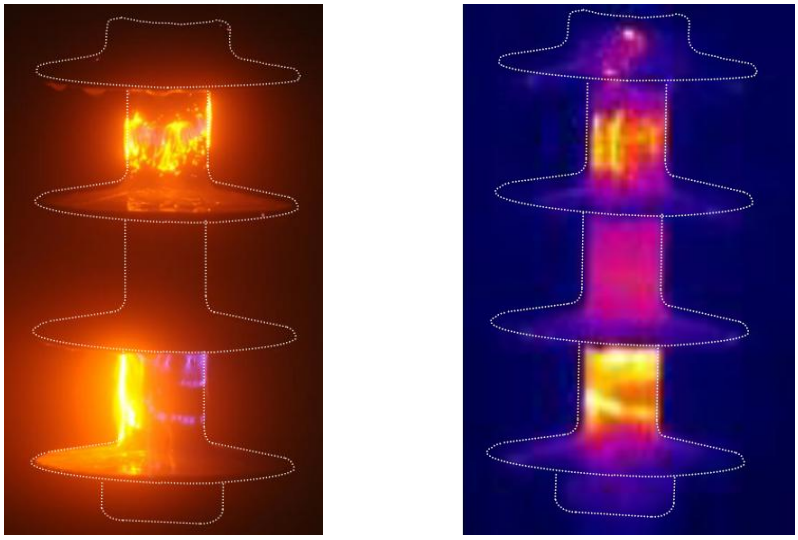

Figure 4-17. Close-up image of an insulator showing streamer discharges and spark channels bridging dry-bands. Some spark channels are spanning more than one neighbouring dry-bands. The IR image confirms the position of the dry-bands. Exposure time 30 sec.

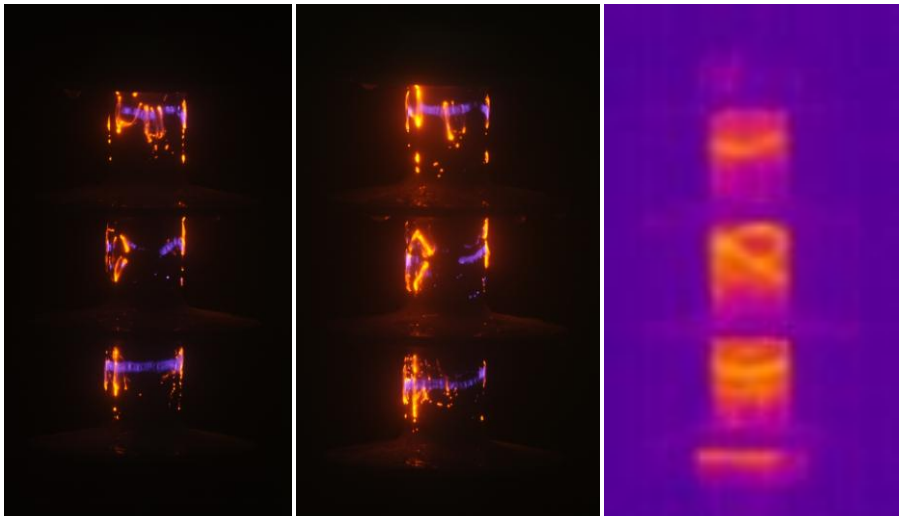

Figure 4-18. Close-up images showing dry-band sparks and streamers and infrared record.

The dry-bands are characterised by very low conductance. However, current continuity and heating of the dry-bands is maintained by the small-scale streamer discharges bridging the bands. The current is limited by the low conductance of the pollution layer. Nonetheless, as the dry-bands expand, higher current spark channels develop from the streamer channels. These sparks may span separate neighbouring dry-bands and they always precede flashover.

As the dry-bands gradually increase their width, spark channels start to bridge longer sections of the pollution layer. Their inception is assisted by the local air ionisation caused by the dry-band streamer discharges. Spark channels carry

more current than the rather low-conduction streamer channels as they span a lower series resistance than the streamer discharges (Figure 4-19). The current records provided more information about the nature of the streamers and the spark discharges which resemble the behaviour of a spark gap controlled by a series resistance where the discharge current is limited and controlled by the pollution layer resistance.

The characteristics of the dry-bands observed during clean-fog tests on silicone rubber insulators are very similar to the dynamics of dry-bands formed on textured silicone rubber samples during the inclined-plane tests described in Chapter 5.

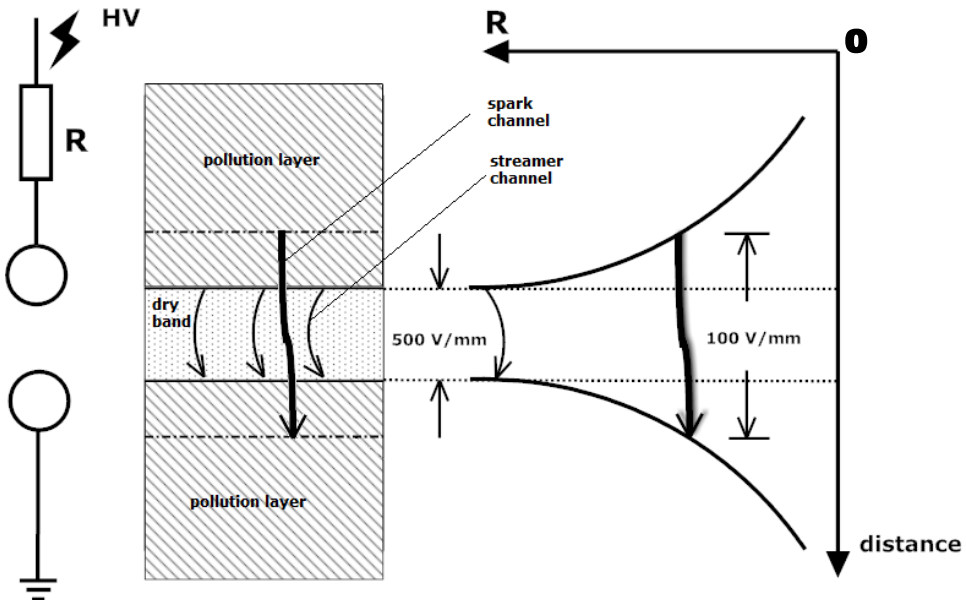

Figure 4-19. The current of streamer discharges is limited by the very high resistance of the dry-band whereas spark channels are more conductive as they bridge a smaller series resistance. This behaviour resembles a spark gap limited by a series resistance R.

4.7 Current records

4.7.1 Calculated electrical properties

The acquired waveform data of the applied test voltage and leakage current were post-processed using the analysis LabVIEW programme to calculate electrical properties. The processing time windows were selected to achieve the optimum resolution in order to obtain comprehensive information depending on the purpose of the analysis. For this reason, data were analysed at a time window of 20ms (cycle duration at 50Hz) and 2 s (the duration of 100 cycles at 50Hz).

Analysis of the current signal over a single cycle, combined with careful synchronization with the video and IR images, enabled the properties of individual discharge events to be determined. On the other hand, a data window of 2s allowed the statistical averaging of rms current, power dissipation and energy loss as a function of voltage.

(a) 20 ms window

Figures 4-21 to 4-25 show the calculated electrical properties of root mean square (rms) of the test voltage and leakage current, the average power and the energy over one cycle of a typical ramp voltage test series consisting of 12 flashover events. The figures show the derived quantities for selected flashover events: 1, 3, 5, 8 and 12 to demonstrate the development of these properties during a ramp voltage test series.

The flashover voltage gradually increased from 21.6 kV for the first flashover event to 30.1, 35.5, 37.3 and 41.2 kV for ramps 3, 5, 8 and 12 respectively. This increase of the flashover voltage was attributed to the gradual washing off of the pollution layer in the fog chamber.

The leakage current of an individual flashover event gradually increased with time along with the increasing ramp voltage towards the flashover instant. However, as the ramp test series progressed, the leakage current of each ramp first increased from the first ramp to the second and then gradually decreased for the rest of the applied ramps confirming the inverse relationship between voltage and the pollution layer conductance. The residual heating due to the previous flashovers could also account for the decrease of current.

The average power maximum pre-flashover peaks reached 100 W, and it was not uncommon to reach 1.3 kW, especially upon the inception of spark discharges. The measured power confirmed the layer heating and the heating of discharge transients detected by the infrared camera. Energy maximum peaks varied from 9 to 28 Joule and followed the same trends as those of average power with respect to the flashover event.

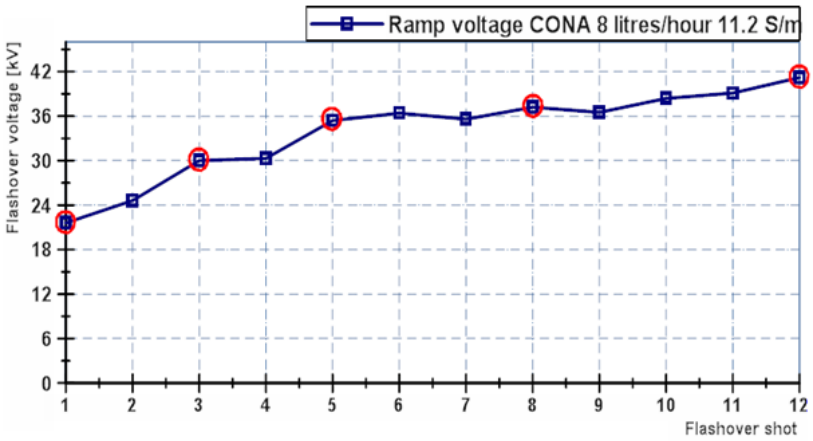

Figure 4-20. Ramp voltage test series for CONA insulator under conditions of high pollution and high fog rate associated with the electrical properties shown at Figures 4-21 to 4-25.

Ramp 1

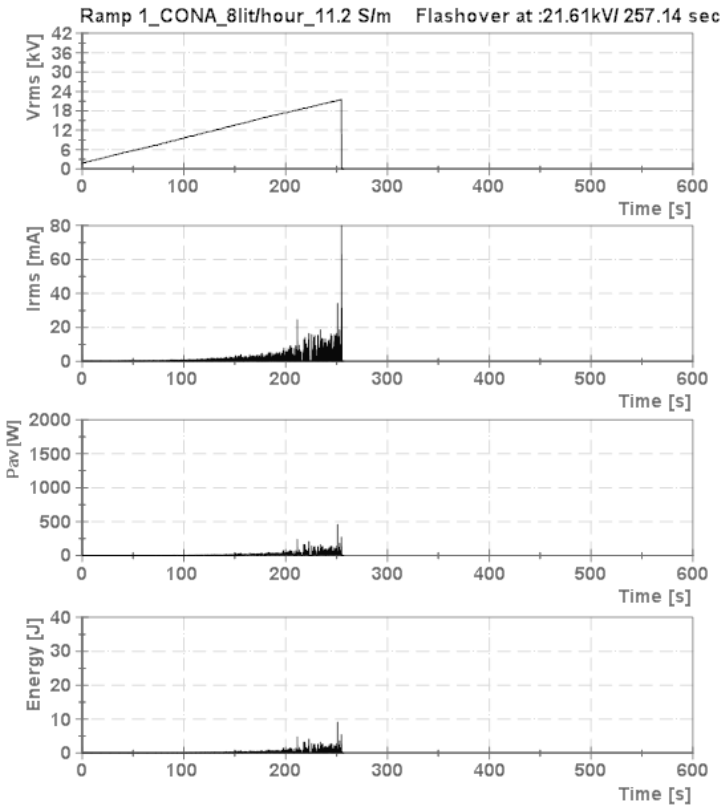

Figure 4-21. First ramp voltage test

Ramp 3

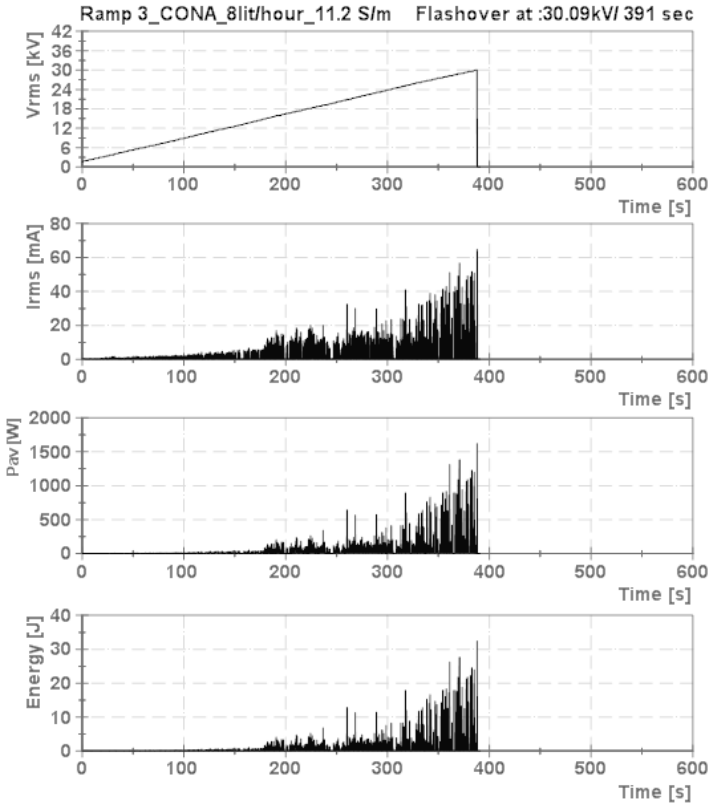

Figure 4-22. Third ramp voltage test.

Ramp 5

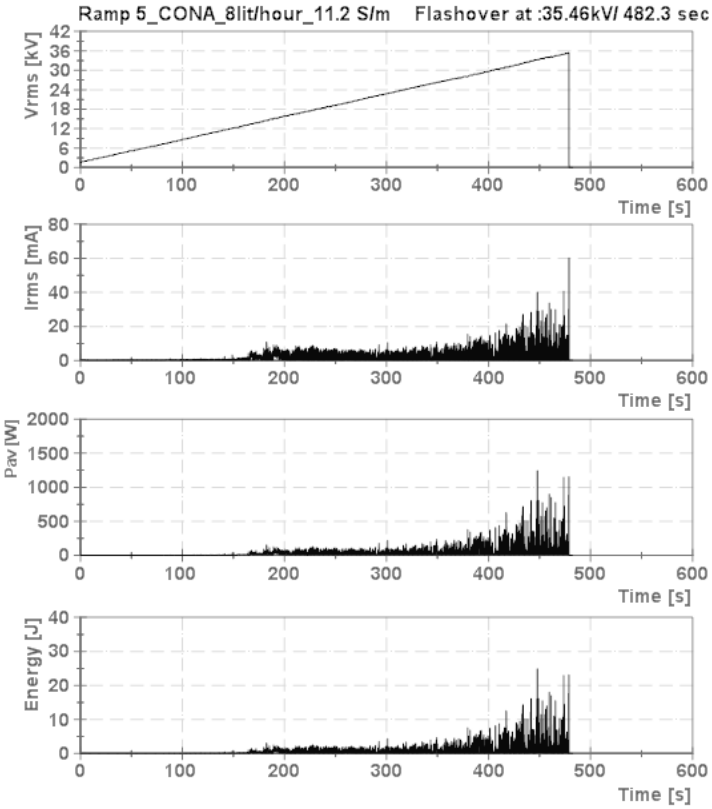

Figure 4-23. Fifth ramp voltage test.

Ramp 8

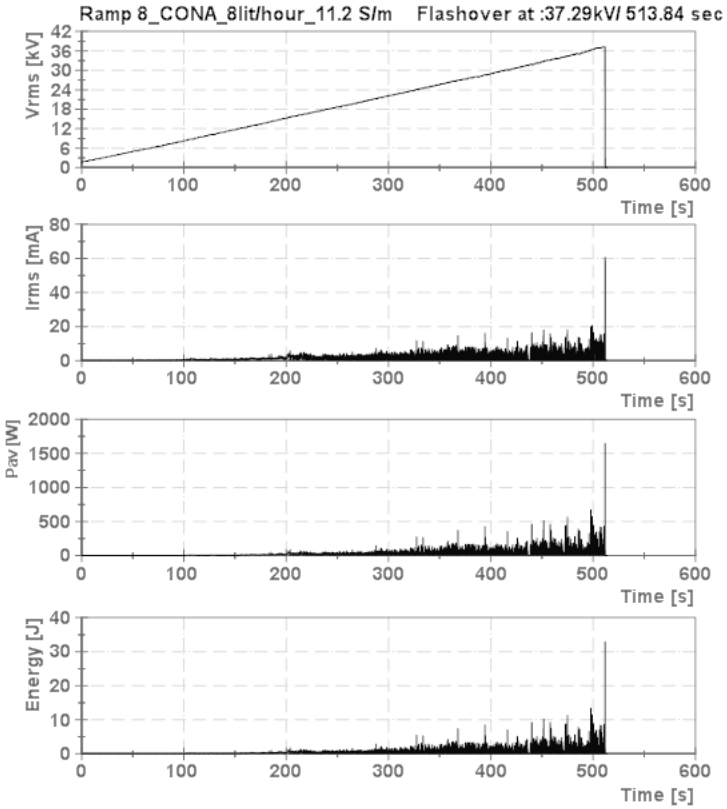

Figure 4-24. Eighth ramp voltage test.

Ramp 12

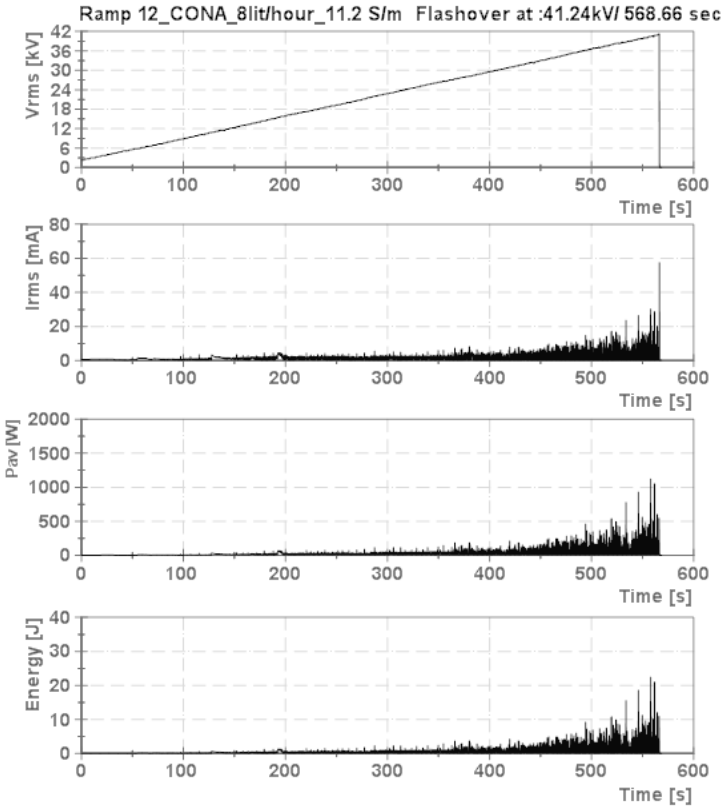

Figure 4-25. Twelfth ramp voltage test.

The current records confirmed that the dry-band and its associated discharges behave in a similar way as a spark gap controlled by the layer resistance (Figure 4-19). Dry-band streamer discharges in series with the pollution layer were characterised by a high resistance that was significantly reduced upon the inception of longer spark channels and the spanning of longer sections of the pollution layer corresponding to a lower series layer resistance. The dissipated power associated with the initiation of spark discharges confirms the local heating and thermal profiles detected by the infrared camera.

The graphical representation of data for a 20ms window provided high resolution of the development of electrical properties during testing. Nevertheless, an effort was made to optimise the analysis time window in order to obtain more information about possible trends associated with the flashover event and to correlate visual and infrared records with the measured and calculated electrical properties.

(b) 2 s window

In this case, the data were presented in an inverse order with the time axis representing the time before flashover in seconds; thus x=0 corresponded to the instant just before flashover. This way of graphical representation was selected to facilitate the comparison between different ramp tests of different time duration by deducing the results on the common event of insulator flashover.

Along with the test voltage, the rms current and the dissipated power, the number of peaks per seconds, N, was calculated. It must be noted that the analysis algorithm counted only peaks greater than 0.5 mA with the intention of excluding peaks not associated with spark channels that could be induced by measurement noise.

The ratios I_{rms}/N and P_{av}/N were also calculated to associate the discharge activity frequency with the leakage current and average power. The ratio I_{rms}/N has the unit of coulombs, and represents the rms average of charge flow per discharge during the window. The ratio P_{av}/N has the unit of joules and quantifies the rms average of energy loss per discharge.

Figure 4-26 shows examples of 2-second average curves for a CONA insulator under conditions of high pollution and low fog rate. As it can be seen on the figure, it was often observed that the discharge activity as expressed by N would progressively decrease as the test approached a flashover event. At the same time, as the discharge activity decreased, the discharge events became more intense and was expressed by the higher values of the charge flow (I_{rms}/N) and energy loss (P_{av}/N) per discharge.

The decrease of discharge activity as the test voltage approaches the flashover level is attributed to the extension of the dry-bands that had been already observed with the infrared camera. The bridging of the wider dry-bands is more difficult, however, when discharges appear, they come in the form of longer higher-current sparks, as revealed by the P_{av}/N and I_{rms}/N graphs.

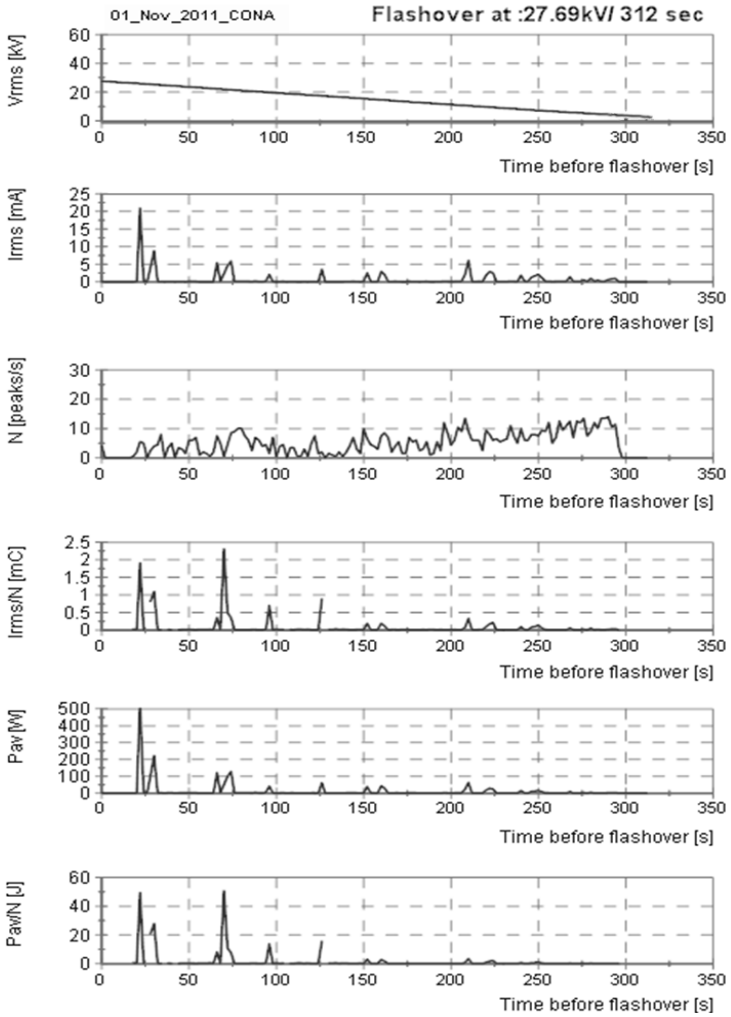

Figure 4-26. Data analysis over a 2 seconds time window for a conventional CONA insulator: flashover at 27.7 kV.

Figures 4-27 to 4-30 show the correlation of digital camera and infrared records with the analysed data of a ramp test, revealing the gradual growth of dry-bands at different instances that last 290 seconds before flashover.

At the beginning of the test, a dry-band formed at the middle shank section (shank section 3) as clearly revealed by the infrared record (Figure 4-28-F). Small discharges at the same region were also detected by visible digital record. As the ramp voltage steadily increased, this dry-band became more vivid and its associated discharges became more intense (Figure 4-28-E). A second dry-band started to form 200 seconds before flashover at shank section 2, with faint discharges again visible in the digital camera records corresponding to this dry-band. Meanwhile, the first dry-band became wider (Figure 4-29-D). As the test progressed, both dry-bands increased in width and surface discharges bridged long sections of the insulator (Figure 4-29-C & B). However, it was often observed with a naked-eye that the discharge activity decreased before flashover, as confirmed by the current records. Therefore, 73 sec before flashover, new dry-bands adjacent to the existing ones appeared and high-current events stressed the insulator (Figure 4-30-A) that eventually resulted in insulator flashover (Figure 4-30-FO).

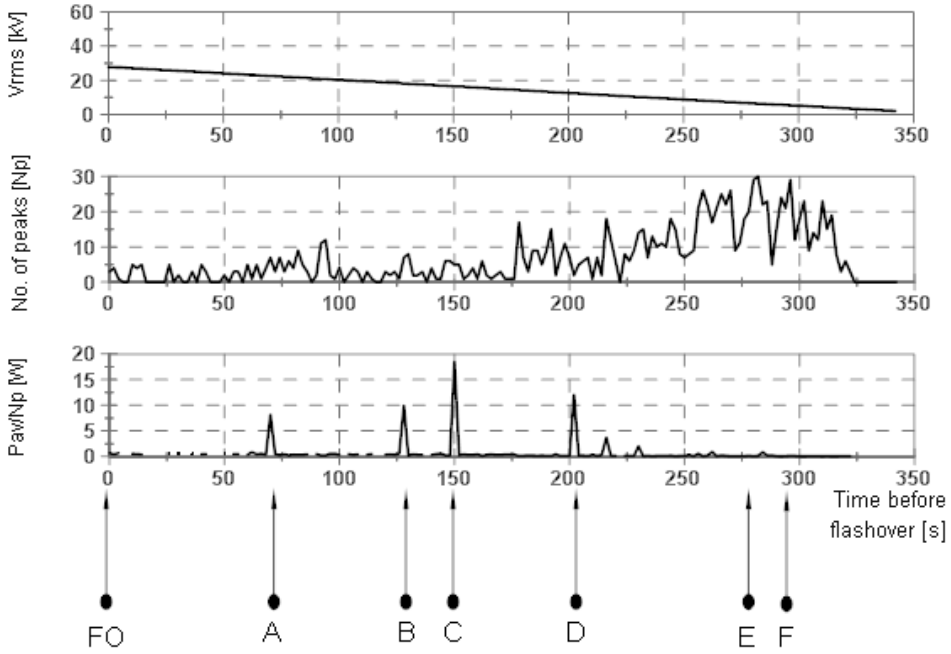

Figure 4-27. Correlation of 2s data with infrared and digital camera recordings for events A, B, C , D , E, F and flashover FO associated with figures 4-28, 4-29 and 4-30.

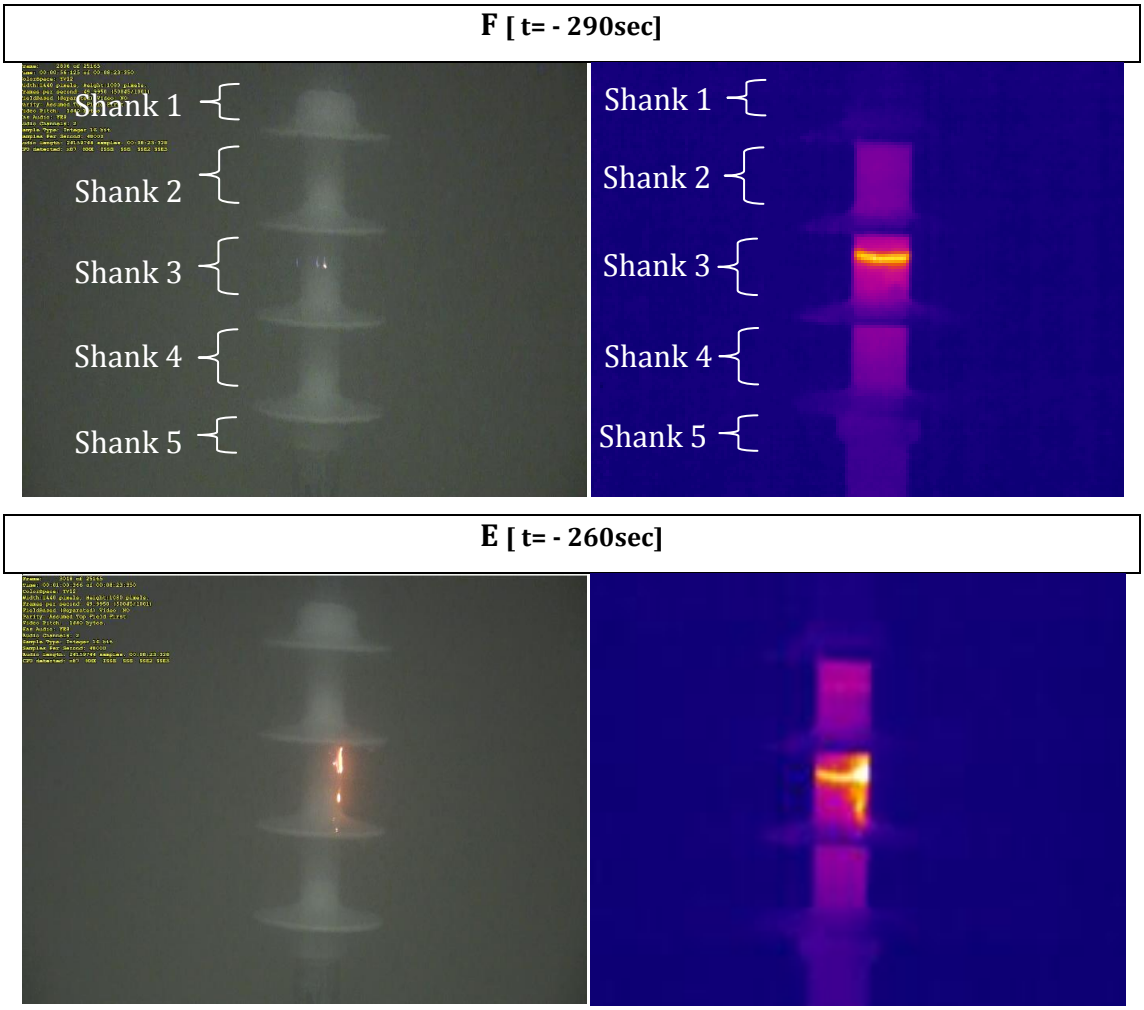

Figure 4-28. Correlation of digital camera and infrared records with current measurement data: records shown in Figure 4-27 at t=-290 sec (F) and t=-260 sec (E).

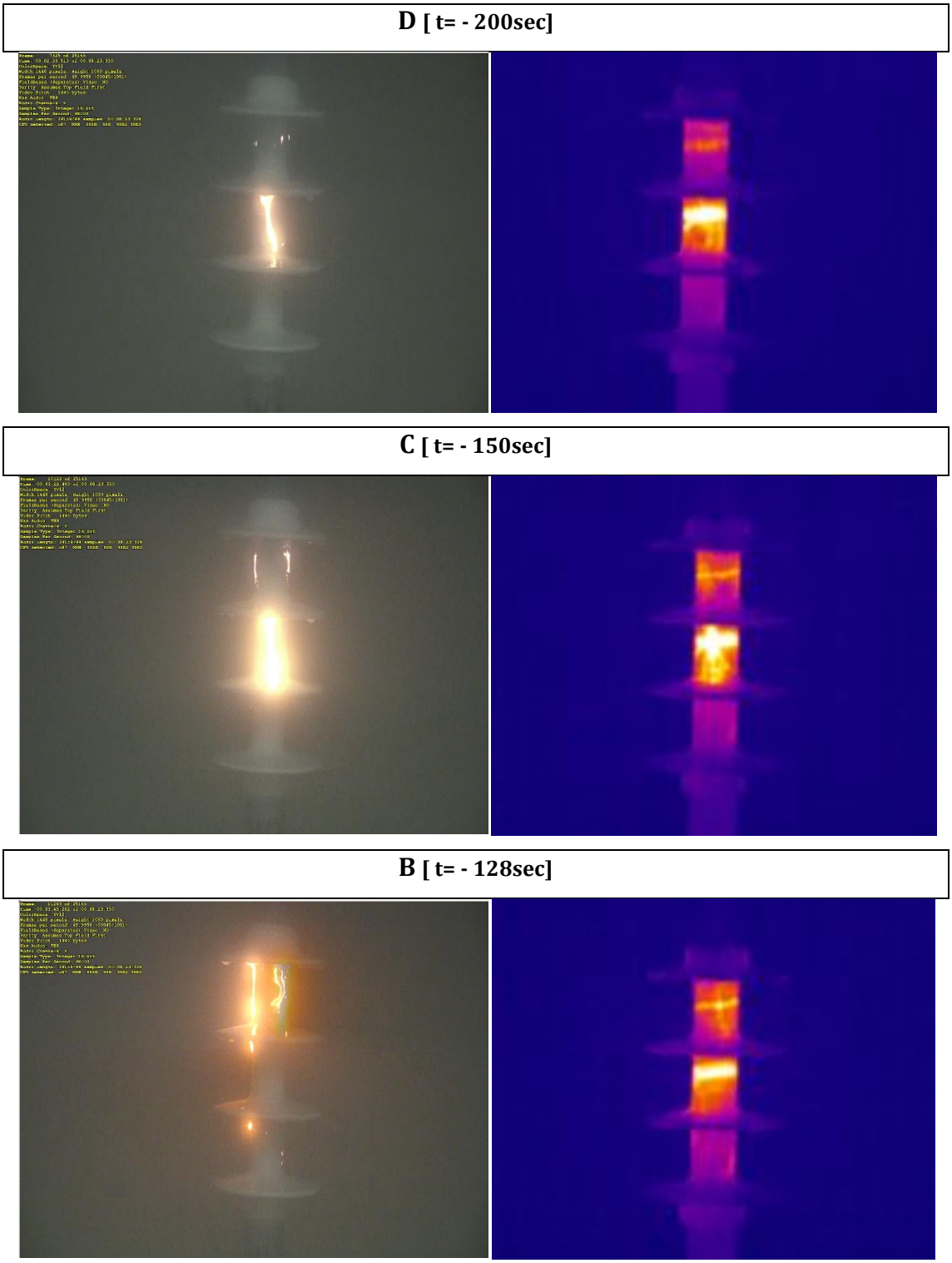

Figure 4-29. Correlation of digital camera and infrared records with current measurement data associated with Figure 4-27: records at t=-200 sec (D) and t=-150 sec (C) and t=-128 sec (B).

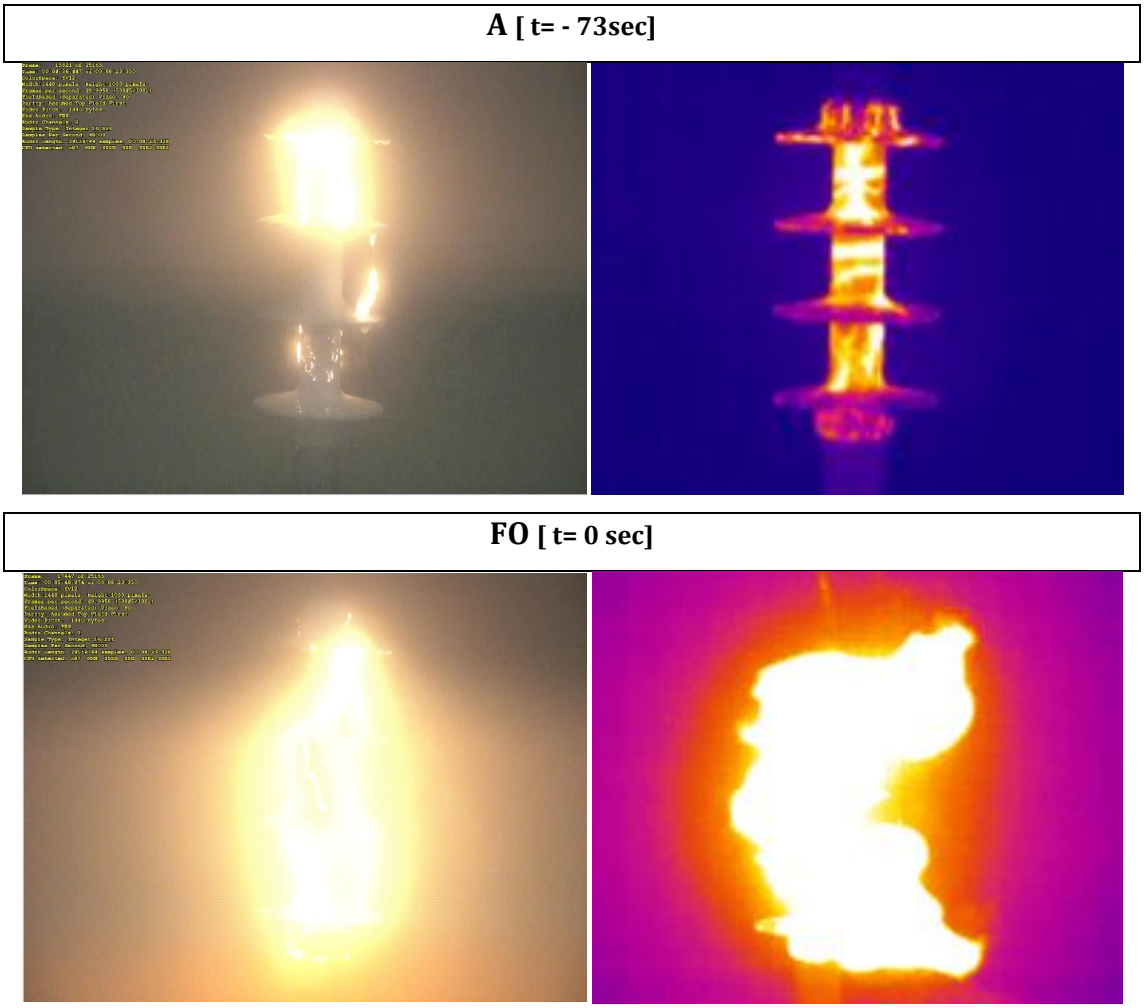

Figure 4-30. Correlation of digital camera and infrared records with current measurement data associated with Figure 4-27: records at t=-73 sec (A) and at flashover (FO).

4.8 Current records for material A and material B

A shown in table 4-1, material B performed better than material A in terms of flashover voltage estimation for ramp voltage tests under conditions of high pollution and low fog rate. This was attributed to a seemingly more hydrophobic surface for material B.

Figure 4-31 shows the 20 highest current peaks in a descending order that were recorded for samples made of material A (CONA – red lines) and samples made of material B (CONB – blue lines) for flashover shot 1, 2, 3 and 4 for all ramp test series. Material A showed higher current peaks than material B, an indication that could suggest that material B is more hydrophobic than material A.

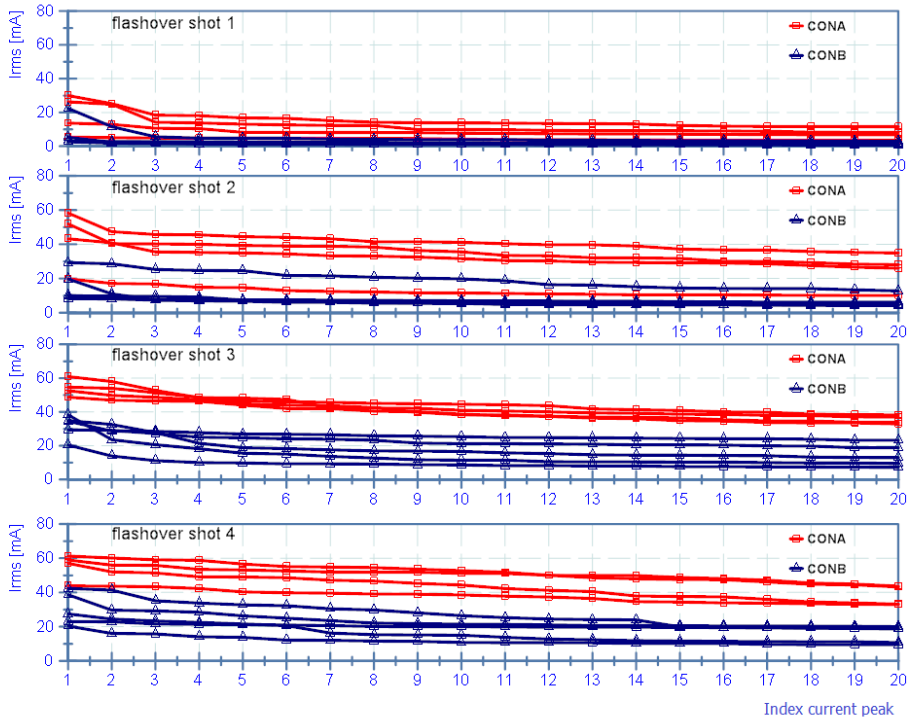

Figure 4-31. Comparison of current peaks between material A and material B. The graphs show the 20 higherst current peaks in a descending order.

4.9 Conclusions

The flashover performance of silicone rubber insulators in clean-fog tests was investigated. In these tests, the increasing conductance associated with the controlled wetting of the kaolin/salt layer by the fog is shown to cause substantial fall on the flashover voltage. The U-curve variation of flashover voltage with wetting time, as revealed by the ramp tests, indicated that flashover voltage varies inversely with the conductance of the pollution layer.

Infrared recordings revealed the modes of dry-band failure of polluted silicone rubber insulators. These dry-bands, that are normally invisible to observation, were monitored and their development was investigated with detail.

The current continuity and heating of the dry-bands are maintained by small-scale streamer discharges, which are of low visibility in fog tests. These streamer discharges may initiate more extended higher current spark discharges that frequently link dry-band regions. Spark channels always precede flashover.

Infrared records also showed that the dry-bands width increase with the increasing test voltage.

Current measurements confirmed the inverse relationship between flashover voltage and layer conductance. Moreover, further data post-processing and correlation with the infrared and visible pictures showed that less discharges are present before flashover but these discharges are characterised by higher current/power peaks. The discharge current is controlled by the layer resistance. In the case of streamer discharges, the dry-band resistance is extremely high, limiting the current. However, when spark discharges bridge longer sections of the insulator, the overall series resistance is lower, allowing the development of the higher currents observed for spark discharges.

The established test procedures, the casting techniques and the investigation of pre-flashover mechanisms for conventional silicone rubber insulators were later applied for textured silicone rubber prototypes as it will be described in Chapter 6.

Chapter 5. Comparative performance of insulation samples with different textures

Summary

Polymeric materials have been extensively used for over 30 years for outdoor insulation applications. The light weight and small size, the resistance against vandalism attacks and the superior anti-pollution performance have contributed to the expansion of polymeric insulators for use with system voltages up to 132kV. Silicone rubber is the polymer that has been favoured due to its excellent water repellent properties and the ability of recovering this hydrophobicity by transferring low molecular weight silicone chains to the adhering pollutants. However, polymeric materials are susceptible to long-term degradation due to erosion and tracking caused by surface discharges.

The reduction of surface wetting of silicone rubber leads to a reduction of leakage current and the associated discharge activity, thus alleviating thermal damage. Nevertheless, under severe atmospheric conditions, the discharge activity is not totally eliminated. For a polluted silicone rubber insulator, the shank regions are more vulnerable, due to the enhanced values of the electric field E and the current density J that favour dry-banding and electrical discharging. The anti-fog designs employed for porcelain and glass insulators can not be applied to polymeric insulators. Moulding restrictions of one-piece housings require designs with simple profiles and without re-entrant parts [1.1]. However, a recently proposed design [1.7] for polymeric insulators consisting of an array of hemispherical protuberance aims to reduce power dissipation by reducing both the electric field E and the leakage current density J and increase the longitudinal creepage length without increasing the overall length of the insulator. Moreover, the formation of parallel current paths could lead to less harmful discharges. Initial reports [1.8] have shown that the introduction of such surface texturing resulted in an enhanced performance compared with conventional, smooth-surface, samples.

Materials that are meant to be used for outdoor insulation should be tested for their ability to resist erosion and tracking. The inclined-planed test, specified by the IEC-60587 standard, is an accelerated ageing test where rectangular samples are subjected to severe electrical stress in order to investigate the performance of materials against erosion and tracking.

In this chapter, inclined-plane tests of rectangular silicone rubber samples are described. Samples with surface texturing were prepared and tested and the results were compared with those for conventional non-textured samples made of the same material. The test results showed an outstanding improvement introduced by texturing. While all conventional non-textured samples failed to fulfil the criteria of the standard test, textured samples on the contrary successfully passed all tests and exhibited a significant reduction of thermal damage due to erosion and tracking. This improvement was attributed to the unique dynamics of surfaces discharges of textured samples: controlled dry-bands form and spanned by discharges that lead to a fall rather than an increase of leakage current. This current limitation inhibits the development of a runaway current that would lead to the transition of surface discharges in the more damaging arc phase. For non-textured samples, dry-band formation was random and anchored arc discharges caused severe erosion. Ancillary current measurements also revealed that the formation of parallel current paths for textured samples, allowed discharges near the metal ground electrode to be mobile, thus mitigate thermal damage.

The formation of stable dry-bands and the development of a high-resolution data acquisition system allowed the characterisation of dry-band discharges by utilising the captured voltage and current records.

The theoretical classification of textured samples, as described in Chapter 2, concluded to a short list of textured configurations that could be employed to develop a full insulator prototype. The material tests explored the performance of these candidate patterns and concluded in the optimum designs that were later implemented in the manufacturing of full textured insulators.

5.1 Textured patterns

The textured samples that were chosen to be experimentally explored consisted of an array of hemispherical protuberances in three arrangements:

- *Contiguous hexagonal* pattern (Texture A, Figure 5-1a).
- *Intersecting hexagonal* pattern (Texture B, Figure 5-2b).
- *Intersecting square* pattern (Texture C, Figure 5-3c).

At any given region of the insulator, if the textured design controls the surface area in a way to reduce the leakage current density J by a factor α and increase the creepage length by a factor β and subsequently reducing the electric field strength by the same factor, then local power dissipation per unit area will be reduced by the combined power density factor ($\alpha \times \beta$). Therefore, factors α and β (and $\alpha \times \beta$) can be considered as a figure of merit of the anti-pollution performance of the insulating surface. A higher value of ($\alpha \times \beta$) would mean enhanced anti-dry band behaviour [1.8].

Table 5-1 show the geometrical calculations of area, creepage and power density factors for textures A, B and C that were the most promising for the development of a textured insulator.

Table 5-1. Area, creepage and power density factors for textures A, B and C [1.8].

Texture	Area factor α	Creepage factor β	Power density factor α x β
Contiguous hexagonal (A)	1.907	1.209	2.306
Intersecting hexagonal (B)	1.446	2.356	3.407
Intersecting square (C)	1.301	2.222	2.891

5.2 Rectangular silicone rubber samples

5.2.1 Test samples

Silicone rubber rectangular samples were manufactured. The dimensions were in accordance with the IEC-60587 standard, 120mm x 50 mm x 6 mm. Conventional non-textured samples were prepared along with samples employing textures A, B and C using the same material and casting techniques. In addition to the textured patterns, a range of diameters of the hemispherical protuberances were used: 2, 4, 6, 8 and 10mm for the intersecting square and 4mm for Textures A and B. Figure 5-1 shows a conventional sample (top) and the zoomed sections of the textured configurations.

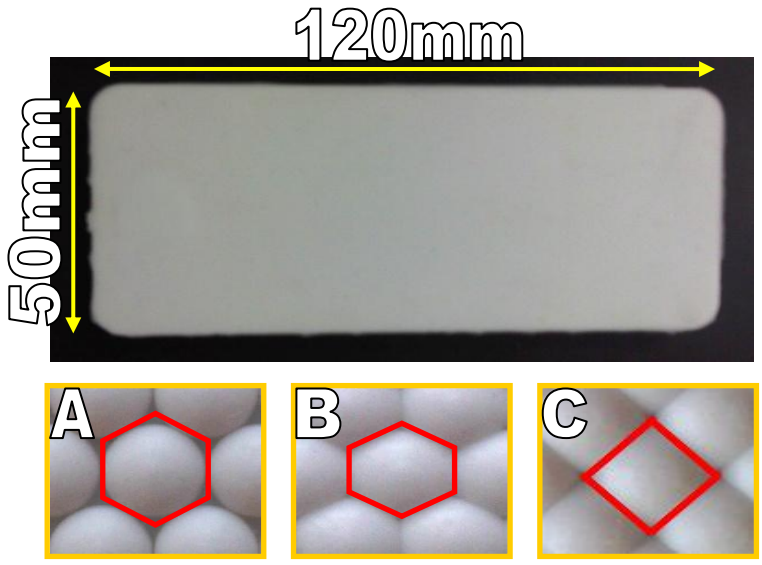

Figure 5-1. Zoomed detail of the contiguous hexagonal (A), intersecting hexagonal (B), intersecting square (C) patterns and a conventional non-textured sample (top).

5.2.2 Sample preparation

The samples were prepared using a commercial silicone rubber, Dow Corning HV 1540/10P. The mixing ratio of the base and the curative was 1:9. Table 5-2 presents some of the main characteristics of this silicone rubber. The casting was performed using the MCP 5/01 vacuum casting machine. The moulding techniques were the same as described in section 3.2. The only difference was that because of the small size and the simplicity of the geometry of the rectangular samples, variable pressure was not applied necessarily (Figure 5-2).

Table 5-2. Properties of HV 1540/10P silicone rubber.

Property	Test method	Typical results
Specific Gravity [g/cm^3]	DIN 53479	1.1
Hardness [Shore A]	DIN 53505	35
Tensile strength [MPa]	DIN 53504	4.6
Volume Resistivity [ohm cm]	IEC 60093	> 5x10^{14}
Dielectric Constant (100Hz)	IEC 60250	2.8
Dissipation Factor	IEC 60250	<0.001
Tracking Resistance	IEC 60587	1A3.5
Dielectric Strength [kV/mm]	IEC 60243	24

A mould consisting of two smooth-surface aluminium plates that, when joined, form a rectangular cavity with the standard dimensions was used to manufacture the conventional samples. For the casting of textured samples, special mould plates were manufactured using a computer numerical control (CNC) machine (Figure 5-2). Blind holes were drilled that would reproduce the contiguous and intersecting patterns on the resulting cast. An injection gate and two vent channels were also drilled in one the two mould plates. The mould was closed and secured in the correct place by using a pair of bolts.

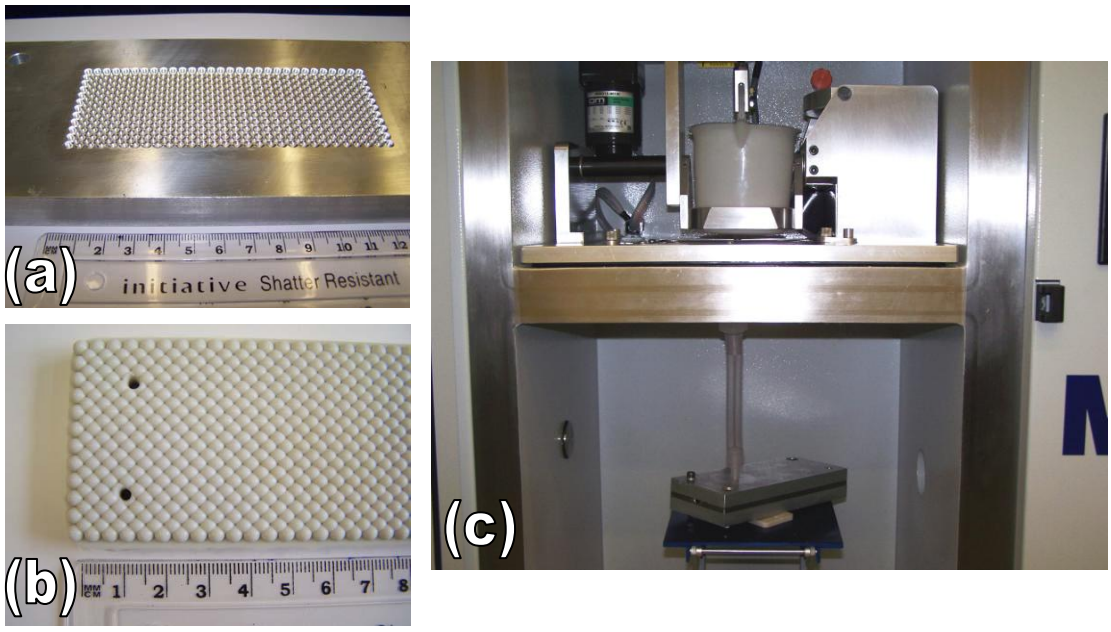

Figure 5-2. Aluminium mould plate for a textured rectangular sample (a), a 4mm intersecting square sample (b) and the mould in the vacuum casting machine (c).

After casting, the mould was placed in the oven for curing at 50° Celsius for 8 hours. After removal from the mould, the sample was visually inspected to ensure that a high quality result has been achieved. Later, it was left at room temperature for another 24 hours to ensure that the silicone cross-linking process has been completed. The sample was then ready for testing.

5.3 The experimental setup

5.3.1 The inclined-plane test facilities

Figure 5-3 shows the inclined-plane test facilities that were used for the material tests of rectangular silicone rubber samples. It consisted of an accelerated ageing unit, a personal computer that had a National Instruments PCI-6254 data acquisition board fitted and another computer used for the infrared monitoring of the test samples. The FLIR infrared camera and Sony Handycam, described in section 3.3, were also employed to monitor the test sample. In some cases, high speed photography was also employed. The arrangement diagram is shown in Figure 5-4.

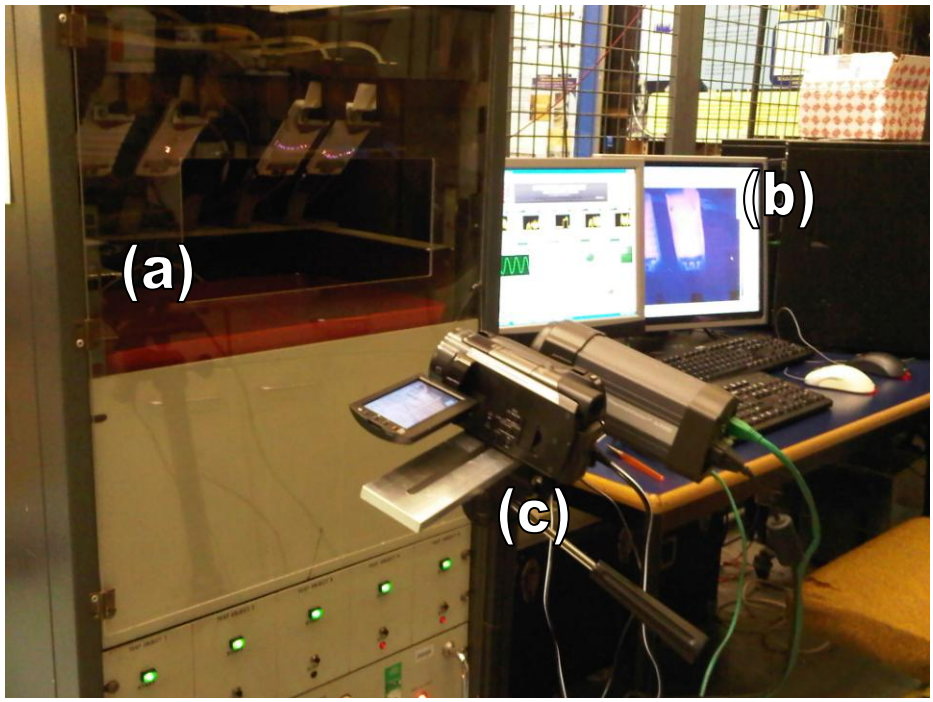

Figure 5-3. The inclined-plane test facilities: the accelerated ageing unit (a), the PCs data acquisition and infrared recording and the FLIR IR camera and the Sony Handycam video camera (c).

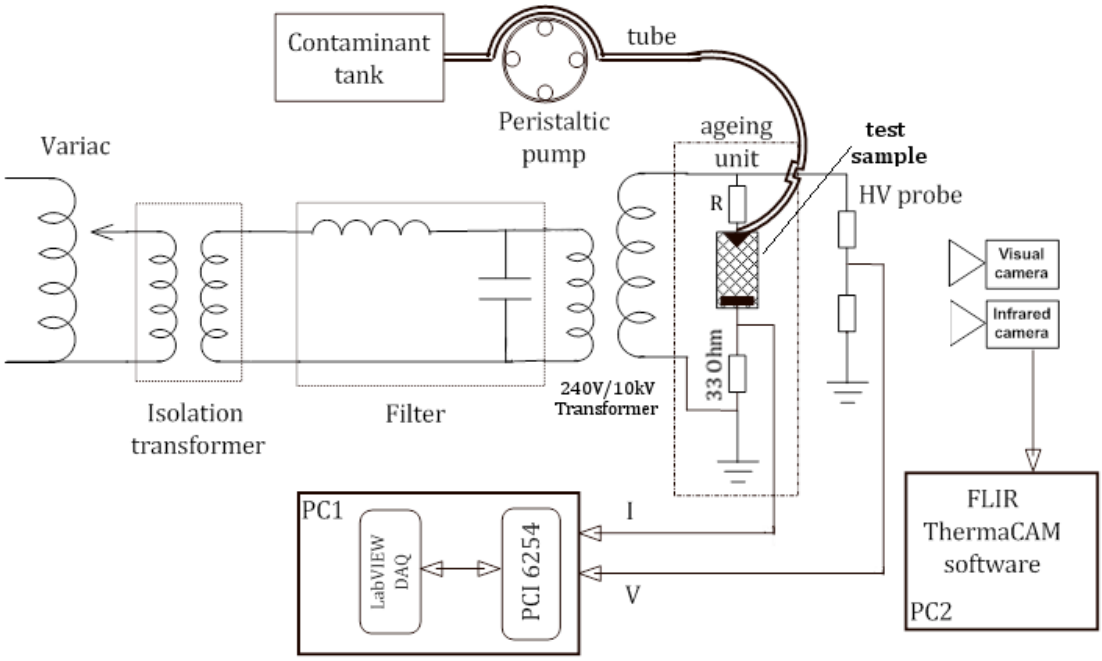

Figure 5-4. The inclined-plane test facilities schematic diagram

(a) The accelerated ageing unit

The accelerated ageing unit is a metal enclosure consisting of the test compartment at the top of the unit and the electrical equipment for the high voltage supply and the saline contaminant supply on the lower shelves of the unit.

Figure 5-5 shows the ageing unit and the two compartments. The top compartment consists of five test bays that can allow the simultaneous testing of five rectangular samples at a 45^{o} inclined position. The contaminant is supplied by five tubes that are attached at the top of each test bay. A peristaltic Watson Marlow 205S/CA pump drives the saline contaminant from a tank in the metal enclosure to the test samples. The pump can achieve flow rates from 0.6 microlitres/min to 22 ml/min. A membrane keypad on the pump allows the adjustment of power and flow rate. A tray at the bottom of the test compartment accumulated the contaminant dripping off the samples and the lost material due to erosion. The top of the test compartment is slotted to allow ventilation. The test compartment door, made of transparent PVC, was modified to allow the monitoring of the test sample using the infrared and visual cameras through a

rectangular opening. An interlock safety system interrupted power supply in case the door was opened during testing.

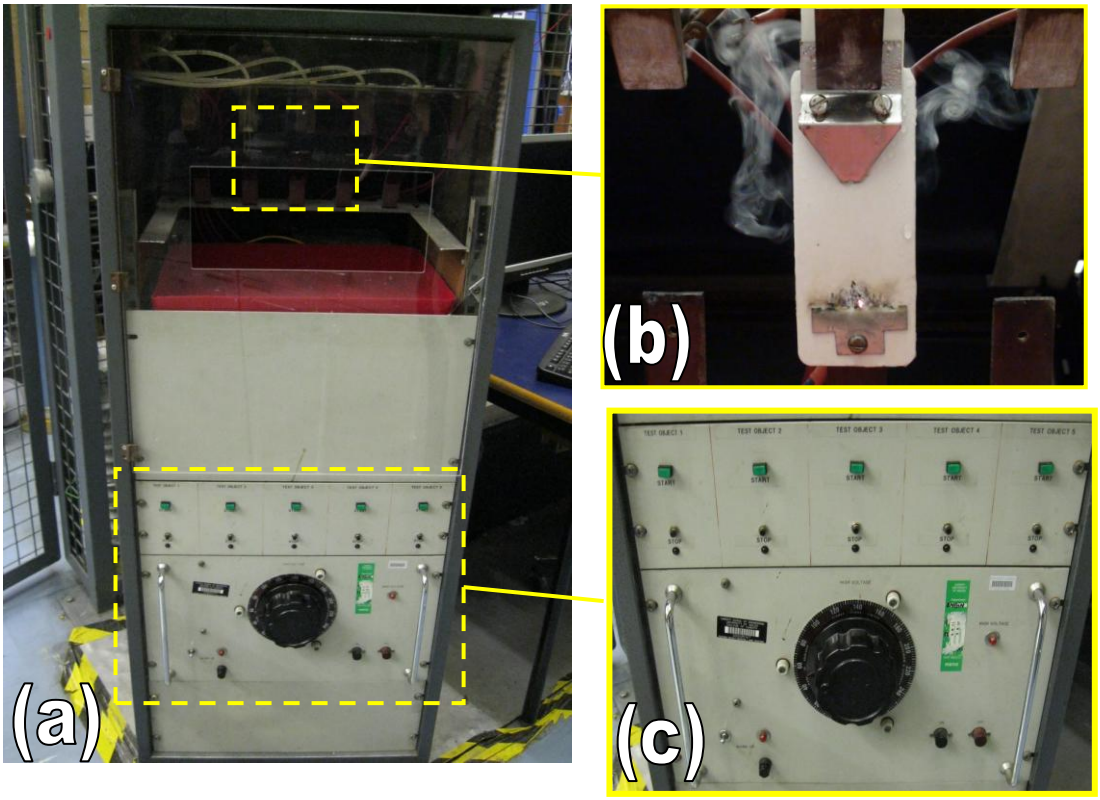

Figure 5-5. The accelerated ageing unit (a), a close-up of a rectangular sample in the test compartment during a test (b) and the HV supply control panel (c).

The distance between the test electrodes (Figure 5-5b) was 50mm. The high voltage was supplied on the top electrode while the bottom was grounded. The contaminant was supplied from the top electrode through a layer of eight filter paper sheets, cut in a shape that they would be fitted between the electrode and the sample. As soon as a steady flow of the contaminant was established on the test surface, the high voltage was supplied.

The IEC standard advocates two test methods: the application of constant voltage (Method 1) and the application of stepwise voltage (Method 2). In the present work, Method 1 was followed. The preferred voltage levels for Method 1 are 2.5, 3.5 and 4.5 kV AC. In these tests, the selected voltage was 3.5kV@50Hz which was maintained constant for up to 6 hours. Depending on the selected voltage, a series resistor and contaminant follow rate were selected based on the guidelines provided in Table 1, clause 4.1 of IEC-60587 standard. For 3.5kV, the

series resistor value was set to 22kΩ and the contaminant flow rate at 0.3ml/min.

The high voltage was supplied by a 240V/10kV, 20kVA transformer whose primary was controlled by a variac embedded in the ageing unit (Figure 5-5c). The supply on each of the five test bays could be switched using five high voltage relays. The relays were also controlled using the data acquisition software that supplied the activation voltage utilizing the digital outputs of the data acquisition board. Push buttons on the ageing unit panel allowed manual switching of the relays as well. The voltage supply was measured using a Ross Engineering high voltage probe (VD 150) with a ratio 2000:1. The transformer and the high voltage probe were located in a caged area that was accessible through a door that would activate an interlock system interrupting the supply if it was opened during high voltage energisation.

The current measurement is performed with the help a 33Ω resistor. A quick-blow fuse in series with the measurement resistor and a 10V metal oxide varistor in parallel are used for the protection of the data acquisition board. The signal, along with that of the applied voltage, is driven to the data acquisition board.

The test end-point criterion that was recommended for criterion A in IEC-60587, as described in clause 5.4, was used. This criterion specifies that states that the sample fails when the leakage current exceeds 60mA for 2 seconds, or if it shows a hole due to severe erosion or if it ignites. Criterion B states that end-point criterion is reached when surface erosion reaches a mark 25mm from the lower ground electrode or when a hole appears due to severe erosion or when the sample ignites. For some ancillary current measurement tests, criterion B was also used and will be stated so in the test procedure description.

The contaminant consisted approximately of 1g of ammonium chloride and 0.2g Triton-X100 non-ionic wetting agent diluted in 1000g of distilled water. The volume conductivity of the contaminant was adjusted to 0.253 S/m. The suspension in the contamination tank was renewed before 4 weeks elapsed.

(b) The data acquisition system

A National Instruments M series PCI-6254 data acquisition board was installed in a personal computer. The card maximum sampling rate is 1.25 MSamples per second for one channel acquisition and 1 MSamples per second for multichannel acquisition. The data board could receive 32 single-ended analogue inputs or 16 in differential mode with a 16 bits resolution. The maximum input range was -10V/+10V. The board could also receive/generate digital signals through 48 digital inputs/outputs. The physical connections arriving from the ageing unit carrying the voltage and current signals was achieved through a SCB-68 connector block. The connection between the connector block and the DAQ board was conducted with a SHC68-68-EPM shielded cable.

A great deal of software development was required to build a data acquisition (DAQ) software that would meet the requirements of the inclined-plane test. The DAQ software was based on National Instruments LabVIEW and it undertook the tasks of acquiring, monitoring and storing the waveforms of applied voltage and leakage current. Moreover, by utilising the digital signalling capabilities of the DAQ board, the programme controlled the ageing unit high voltage relays. The board would send a digital high-state signal in a TTL logic to the relays as soon as the programme was initiated, allowing them to be ready for manual switching. If the leakage current exceeded 60mA, the programme would automatically interrupt the power supply from the failed sample without disturbing the rest of the samples. A relay power supply could also be switched off through the software interface. Once 6 hours of testing were elapsed, the software would switch off all relays, terminating the test.

Figure 5-6 shows the front panel of the data acquisition software. At the top, five graph indicators present the history of rms leakage current during the test for each sample. Below its graph, a virtual push button was used to interrupt the power supply to the corresponding test bay. Lower on the left, another graph indicated the waveform of voltage along with indicators of rms value. Next to it, there is information about the saving of acquired data and the elapsed time with a warning indicator in case the programme has been set not to keep data records. The panel is completed with information about the state of the high

voltage relays (on or off) and the execution of LabVIEW graphical code in the background.

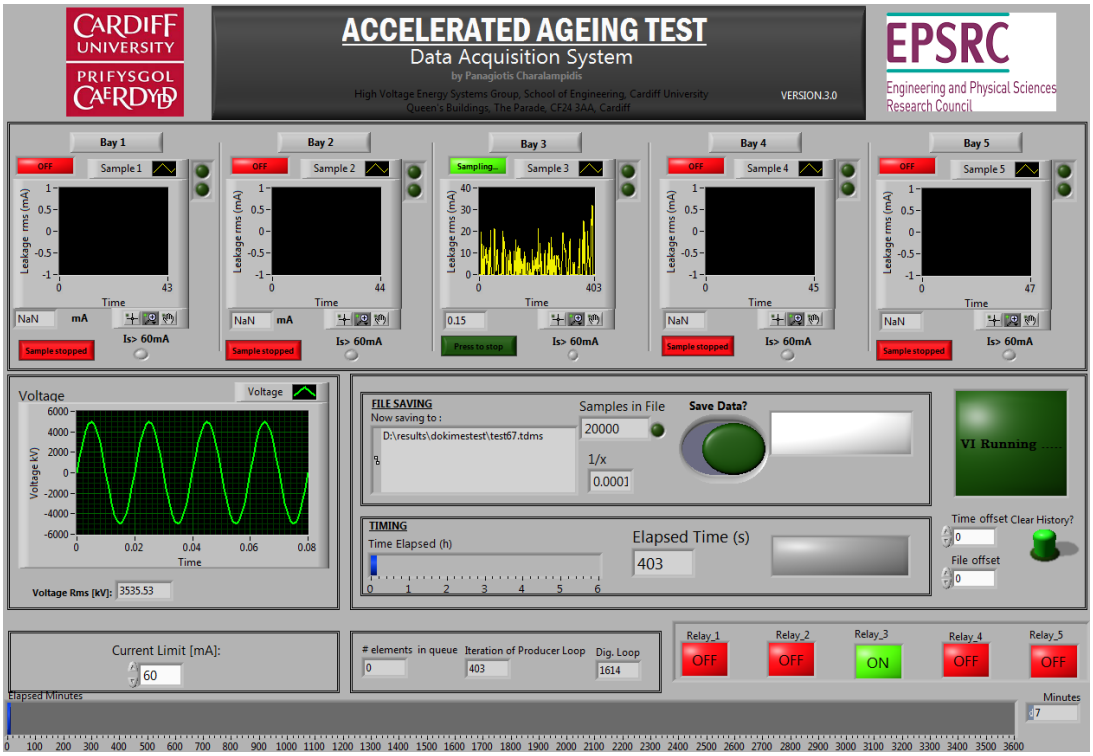

Figure 5-6. The front panel of the data acquisition software during an inclined-plane test of a sample tested in bay 3.

The sampling rate for all material tests was 10 kSamples/sec per channel. For the power frequency, that corresponded to 200 samples per cycle. The waveform signals of voltage and current were stored in TDMS files in the same manner as described in section 3.1.3. The main difference between the data acquisition software designed for the fog chamber tests and the inclined-plane test was the sections of programming code addressing the automation demands for the high voltage relays.

For one test sample and 6 hours of testing, 3600 TDMS files were stored, equivalent to approximately 9 gigabytes of data. This necessitated post-processing of these segmented data which was achieved using the same analysis software described in section 3.1.3.

Figure 5-7 shows a snapshot of the LabVIEW programming code, called block diagram, for the file saving and data processing functions.

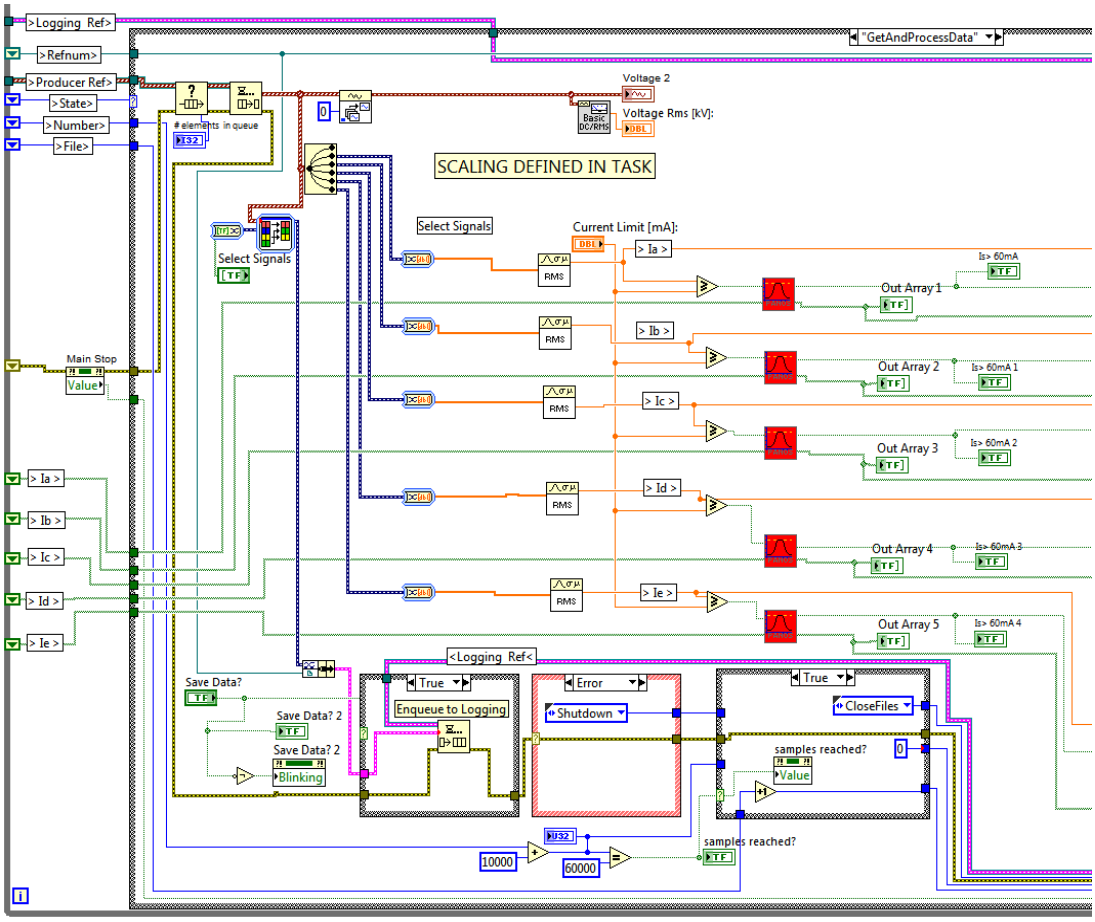

Figure 5-7. Snapshot of the LabVIEW block diagram programming code: data processing and saving functions of the producer loop.

5.3.2 Camera recording

The FLIR infrared camera and the Sony Handycam visual camera described in section 3.3 were employed to monitor the samples during the inclined-plane tests. The parallel monitoring enabled the comparison of records in both the infrared and the visual spectrum. For this purpose, the PVC door of the test compartment was modified with a rectangular opening allowing camera recordings. The Sony Handycam stored the visual records in its integrated hard disk drive while the infrared A325 camera was connected to a personal computer where the records using FLIR ThermaCAM Researcher software were stored. The image capturing frequency of the camera was set to 60Hz.

5.4 Test procedures

5.4.1 Inclined-plane tests

The rectangular samples were weighed before the test. Then, they were fitted with the steel electrodes and the filter paper sheets between the sample and the upper electrode. After the sample was placed in the test position in the ageing unit, the peristaltic pump was turned on to supply 0.3ml/min of the contaminant by setting the pump speed to 16.5 rpm. Both visual and infrared cameras were mounted in parallel on a tripod, monitoring the test sample. Video records of test events were stored in files. The FLIR infrared camera was set to maximum image capturing, storing 60 frames per second.

The data acquisition software enabled the high voltage relays by sending a high-state 5V DC signal. As soon as steady and uniform flow of contaminant on the sample surface was secured, the relays were turned on to supply the test voltage by operating the push buttons on the control panel of the ageing unit. The test voltage was 3.5kV at power frequency throughout the test. At the same time, the data acquisition programme started monitoring and storing in files the waveforms of voltage and current. The sampling rate was 10 kSamples/sec for each analogue channel, capturing 200 samples per cycle. The duration of the test was 6 hours throughout which visual observations on evidence of thermal damage were performed. The test was terminated when current exceeded 60mA for 2s, or the sample showed a hole due to erosion or the sample ignited. After the test, the sample was removed from the ageing unit to weigh it and to note the amount of material loss during the test.

5.4.2 Ancillary current measurements: Five-electrode inclined-plane tests

For the purpose of having a more detailed insight of the current distribution on the sample surface, the standard single ground electrode was replaced by five smaller and separate electrodes (Figure 5-8). The data acquisition software was also modified to monitor and store the waveforms of voltage and the five current signals obtained from the five separate electrodes. Specifically for these modified tests, the end-point criterion used was criterion B, where the test was terminated when the surface erosion track reached a mark, 25mm from the

ground electrode or when a hole appeared due to erosion or when the sample ignited. The test procedure was the same for the standard inclined-plane tests.

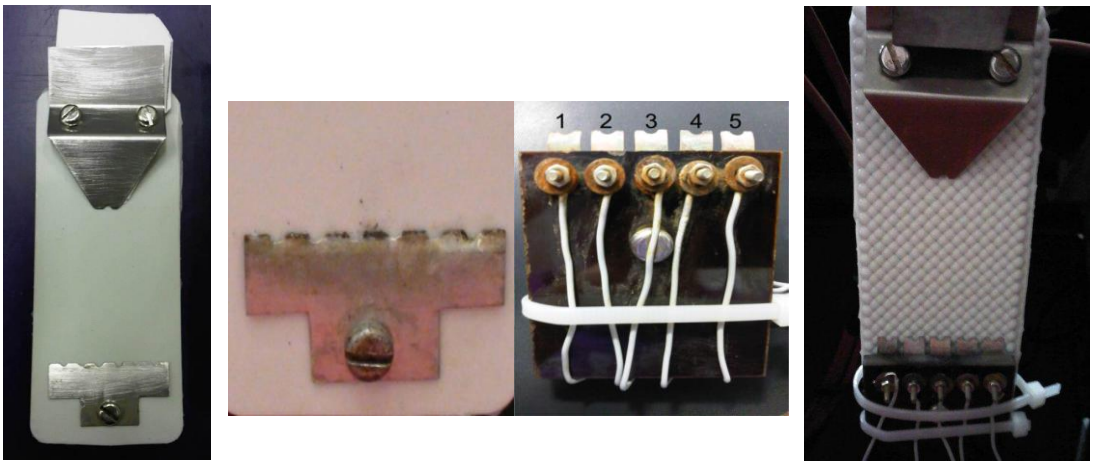

Figure 5-8. The IEC-60587 single ground electrode (left) and the modified ground electrode consisting of five smaller separate electrodes (right).

5.5 Test results - Discussion

5.5.1 Inclined-plane tests results

Table 5-3 summarises the results of the IEC-60587 inclined-plane tests of conventional non-textured samples and textured samples. The results are in full concordance with the anticipated improvement introduced by fine surface texturing.

All textured samples matched the criteria of the inclined-plane experiment and passed the test. The 100% success rate of textured samples, regardless of the geometrical configuration or the protuberance diameter, contrasts with the constant failure of conventional non-textured samples made of the same material. Current measurements and infrared photography extended the interpretation of the inclined-plane test results by correlating visual observations of erosion, tracking and discharge activity with images of the infrared spectrum and electrical properties.

Table 5-3. Test results of IEC-60587 inclined-plane tests

Texture Diameter (Texture type)	Numbers Tested	Pass	Fail	Fail Time (s)		Range of Max rms Current (mA)	Track Length (mm)		Erosion Depth (mm)		Wt. Loss (g)	
				Min	Max		Min	Max	Min	Max	Min	Max
untextured	6	0	6	67	180	> 60.0	42.0	47.0	5.0	6.0	2.5	3.0
2 mm (C)	4	4	0	-	-	38 – 44	20.0	24.0	4.0	5.0	1.5	2.5
4 mm (A)	4	4	0	-	-	34 – 37	20.0	24.0	3.0	5.0	1.0	1.5
4 mm (B)	4	4	0	-	-	42 – 47.5	6.0	18.0	1.0	3.0	0.5	1.2
4 mm (C)	8	8	0	-	-	40 – 43	5.0	15.0	<1.0	3.0	negligible	0.5
6 mm (C)	6	6	0	-	-	40 – 44	6.0	20.0	<1.0	5.0	negligible	1.1
8 mm (C)	4	4	0	-	-	38 – 42	18.0	23.0	3.0	5.0	1.3	1.5
10 mm (C)	4	4	0	-	-	45 – 50	15.0	24.0	4.0	5.0	1.4	1.5

(a) Conventional non-textured samples

Figure 5-9 shows the current rms history of a non-textured sample that failed the test after 110 minutes and an infrared record indicating the heating of the contaminant along with the discharge activity. The flow of the contaminant remained narrow on the sample surface throughout the test (Figure 5-9b). The first few minutes of the test, discharge activity was random all over the test surface. Soon, however, dry-band formation was concentrated near or at the ground electrode region where unstable metal-arc discharges tend to anchor at a specific location, causing severe erosion and eventually failure for all non-textured samples.

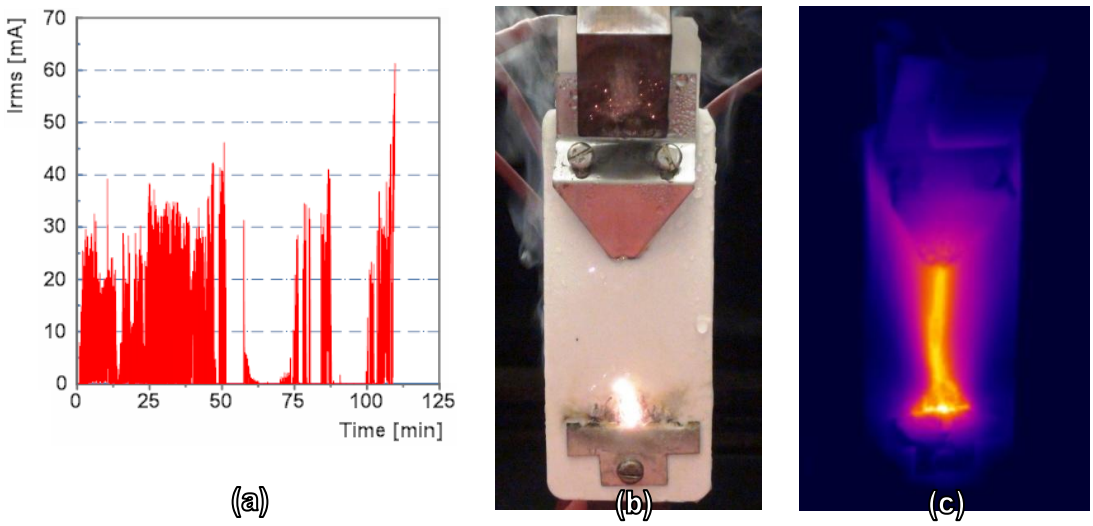

Figure 5-9. Non-textured sample during an inclined-plane test. The current rms record (a), a visual record showing anchored metal-arc discharges at the ground (b) and infrared record showing the narrow contaminant stream and the arc discharging near the ground electrode (c).

(b) 2mm intersecting square (Texture C) samples

The dynamics of surface discharges for textured samples were significantly different than the case of non-textured samples. Arcing at the ground electrode was drastically reduced, and stable and controlled dry-bands formed which could be seen with a naked-eye and were also detectable with the infrared camera. Due to the geometry of the upper high-voltage electrode, dry-band formation was first detected in the adjacent area, and it was characterised by three main features. The development of a line of short parallel and dynamic streamer discharges, that gradually spread across the width of the sample were visually observable. The onset of these surface discharges was associated with a fall rather than an increase of current. This 'necklace' shape of discharges along with the dry-band, moved in the direction of the contaminant flow, reaching the ground electrode after some seconds. The time required for the discharges to traverse the sample surface was greater than the time needed for the contaminant to move from the top to the lower electrode. This discharge activity pattern was repeated throughout the test.

While, in the beginning, the contaminant flow remained narrow, it was later spread on the sample surface as indicated by the infrared records (Figure 5-10). Occasionally, the line of streamer discharges would extinguish while moving along the sample surface but most of the time they would reignite. Whenever the line of discharges reached the ground electrode, the discharges would transform to metal-arcs that would be localised, causing limited erosion.

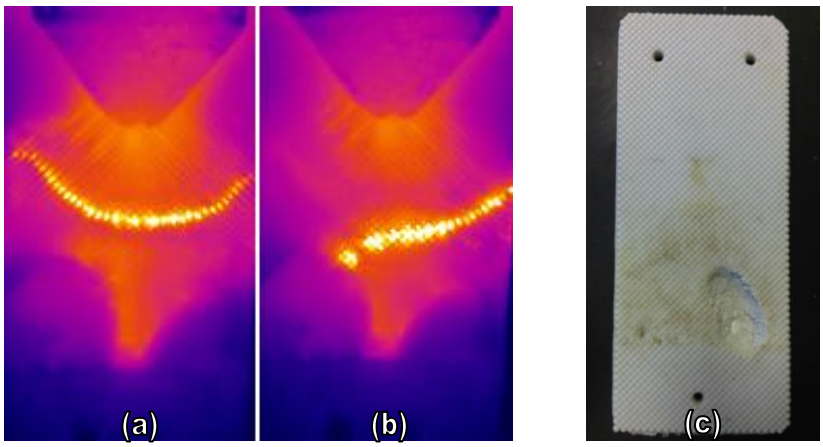

Figure 5-10.Infrared records of line of parallel discharges advanving on the sample surface (a & b) and evidence of thermal damage after a 6 hours test (c) (2mm Texture C).

(c) 4mm Contiguous and Intersecting Hexagonal (Textures A& B) samples

In the case of both contiguous and intersecting hexagonal samples, parallel streamer discharges spreading across the width of the sample and advancing towards the ground electrode were also observed. The appearance of these discharges was associated with a fall of leakage current as well. Near the ground electrode, these discharges took the form of metal-arcing that, unlike non-textured samples, were mobile and spreading across the ground electrode resulting in considerable alleviation of thermal damage and material loss.

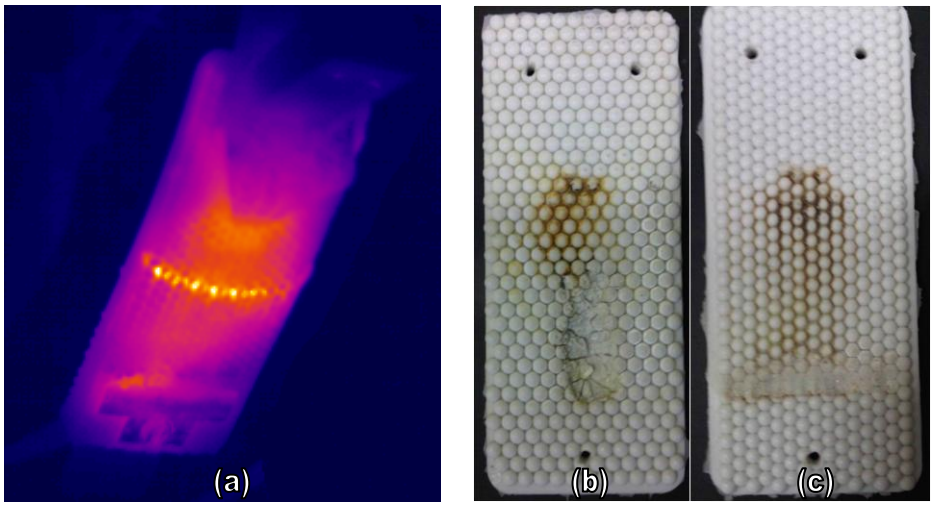

Figure 5-11. An infrared record of a contiguous hexagonal sample with a line of parallel discharges advancing on the surface (a) and evidence of thermal damage of both texture A and B samples after 6 hours of test (b & c).

(d) 4mm intersecting square (Texture C) samples

A line of parallel streamers spread across the width of the sample and advanced towards the ground electrode. A close inspection of these faint discharges revealed that the discharge channels formed along the intersecting edges of the hemispherical protuberances. In the square pattern, all intersections are aligned at 45 degrees to the electric field direction. Figure 5-12 shows the dry-band discharges on a 4mm square sample along with a temperature profile. These discharges, as seen with the naked-eye, are rich in UV, which is typical of streamers growth. As the discharge approached the proximity of the lower ground electrode, the discharges got elongated and tend to jump over the protuberances rather than following the intersections paths. The IR records and the temperature profiles show obvious similarities with the dry-bands observed

for silicone rubber insulators which were also maintained by streamers spanning the dry-bands at the insulator shank.

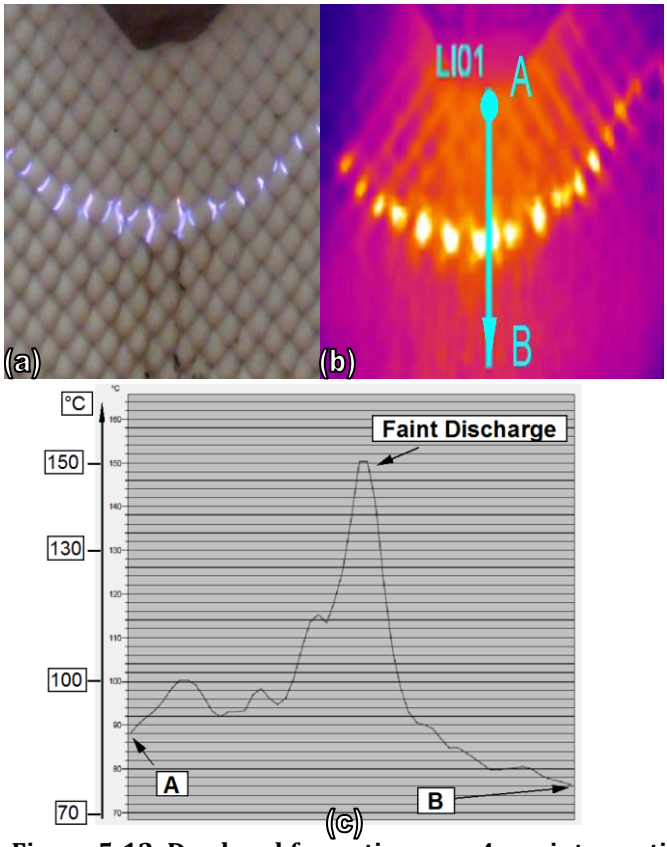

Figure 5-12. Dry-band formation on a 4mm intersecting square sample: Visible record (a), IR record (b) and temperature profile along the path A→B (c).

With the help of a high-speed camera operating at 2000 fps and exposure time of 0.5 ms, it was observed that not more than 3 discharges bridged the dry-band per half-cycle of current. The onset of the faint discharges were again associated with a fall of current and the time required to traverse the sample surface was slower than the time required for the contaminant to reach the ground electrode.

Figure 5-13 shows IR records of a line of discharges advancing towards the ground electrode. During this transit, the streamer discharges of the moving dry-band could briefly extinguish only to resume few seconds later. It took approximately 20 seconds to cross the whole length of the sample. Near the ground electrode, the discharges got elongated and took the form of metal-arc discharges but these were very mobile, thus erosion and material loss were greatly alleviated.

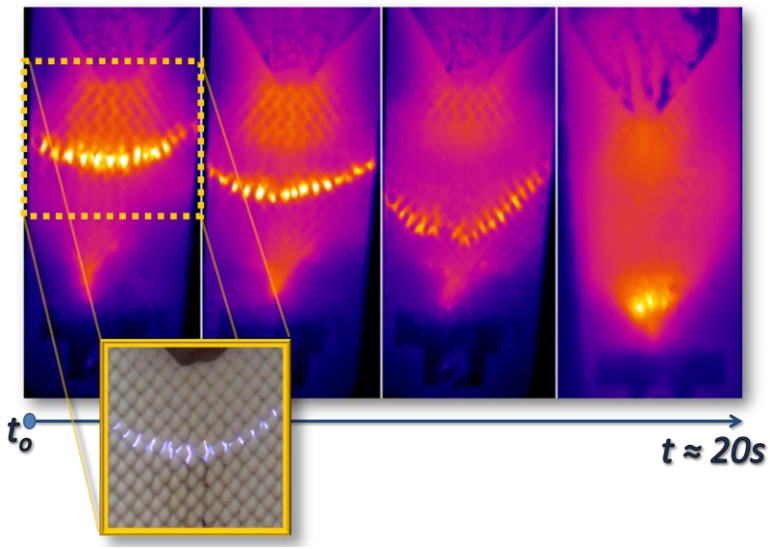

Figure 5-13. Progression of line of streamer discharges along the sample surface.

This repetitive pattern could be interrupted by periods of no activity. These 'dark periods' were associated with the erosion of the sample around the ground electrode that sometimes inhibited contaminant flow continuity.

(e) 6mm intersecting square (Texture C) samples

The line of streamer discharges traversed the sample surface and the onset of these discharges was associated with a fall of leakage current. The 6mm intersecting square pattern had overall a very similar behaviour to that of the 4mm intersecting square configuration, with the material loss due to erosion being slightly greater than the 4mm intersecting square pattern (Figure 5-14).

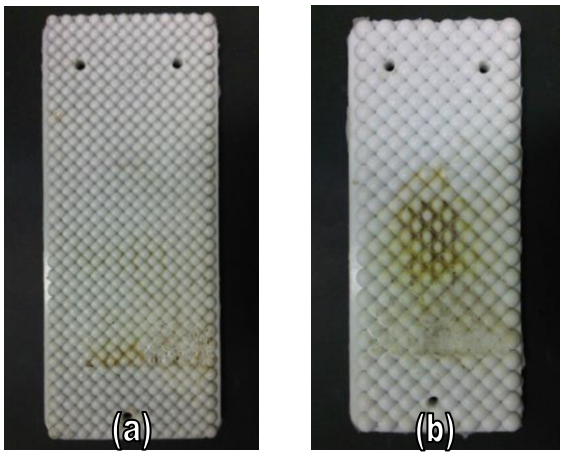

Figure 5-14. Evidence of thermal damage of a 4mm intersecting square (a) and a 6mm intersecting square sample (b) after an inclined-plane test.

(f) 8mm and 10mm intersecting square (Texture C) samples

Unlike the smaller diameters of Texture C samples, the 8mm and 10mm intersecting square samples showed a more random discharge activity. The line of advancing discharges, observed for smaller diameter sizes, appeared only a few times during the test. That meant that stable dry-bands could not be formed or the 3.5 kV test voltage was insufficient to initiate streamer breakdown of the dry-band. Discharge activity at the lower electrode was more intense and not as mobile resulting in greater loss of material due to erosion (Figure 5-15).

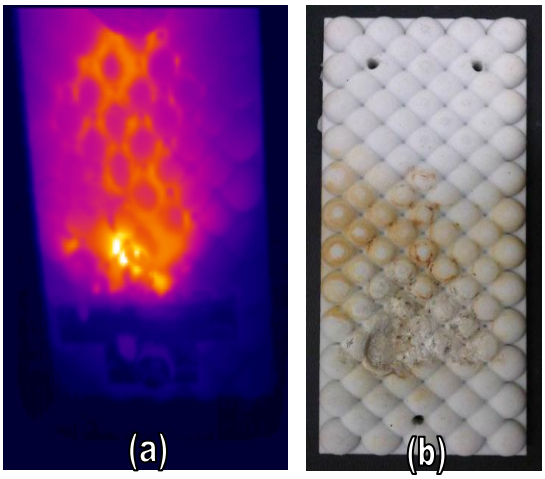

Figure 5-15. IR record (a) and a 10mm intersecting square sample after testing (b).

The inclined-plane tests revealed an outstanding improvement in terms of resistance against erosion and tracking introduced by textured patterns. Based on the discharge activity pattern and the loss of material due to thermal damage, the 4mm and 6mm intersecting square patterns stood out as the most promising configurations for the development of a full insulator prototype.

5.5.2 Modified inclined-plane test results

As described in section 5.4.2, inclined plane tests with 5 separate electrodes were performed to investigate the current multi-path effect. Figure 5-16 shows the current rms history distribution of a conventional non-textured sample that failed the test after approximately 3 hours of testing (criterion B) and a 4mm intersecting square sample that successfully passed the test. The graphs show

the applied test voltage, the current conducted by each separate electrode and the total current rms history.

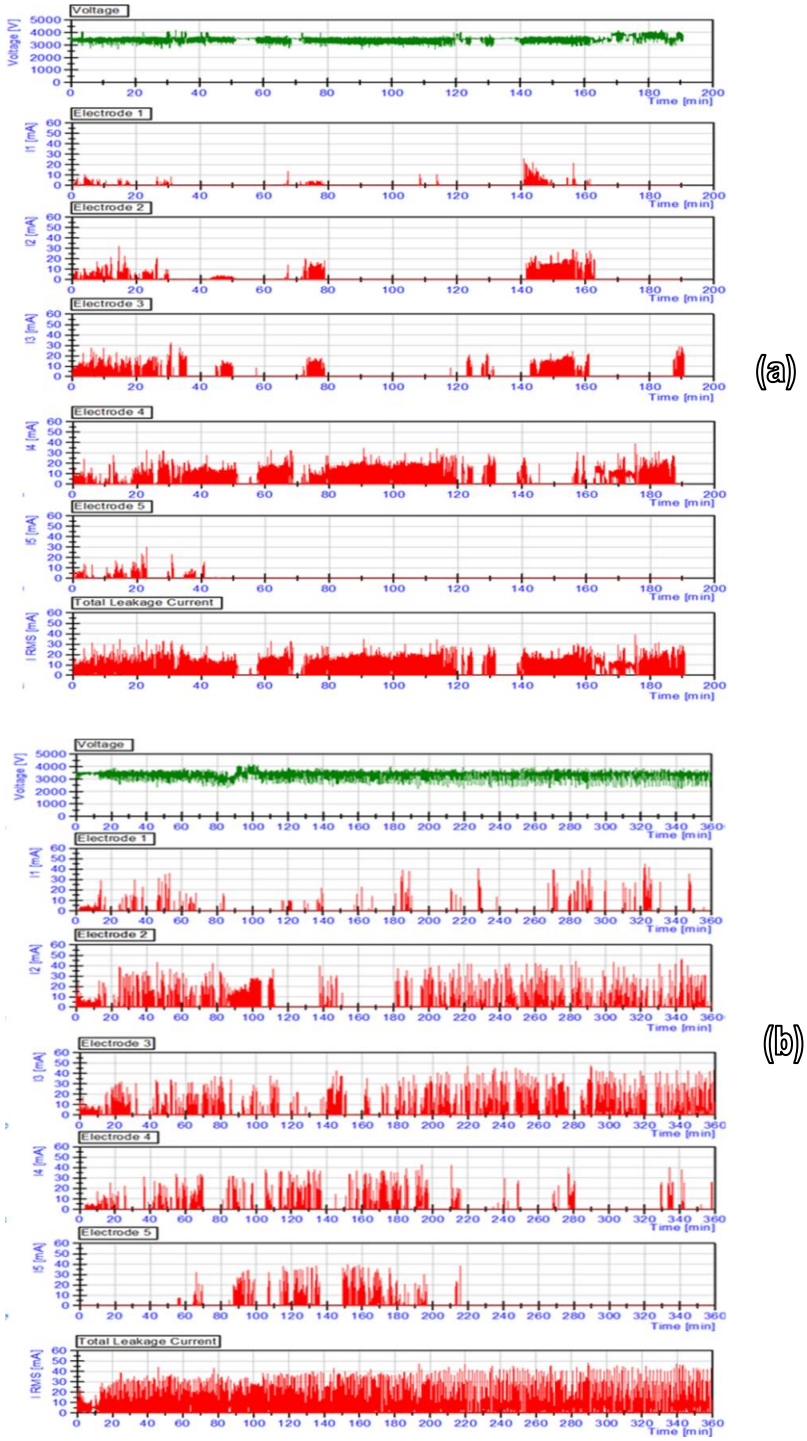

Figure 5-16. Current distribution for (a) non-textured sample that failed the test after approximately 3 hours(time scale 200 mins) and (b) 4mm intersecting square sample after 6 hours of testing (time scale 360 mins).

For the non textured sample, most of the leakage current is conducted by electrode 4, and this was driven by an anchored discharge causing severe

erosion. This behaviour is attributed to the persistence of surface discharges at the narrow contaminant stream. For the 4mm intersecting square case, the leakage current is more evenly distributed across the lower electrode, confirming the formation of parallel current paths and the high mobility of discharges across the ground electrode. This behaviour results in a significant mitigation of surface erosion.

5.5.3 Current measurements and dry-band characteristics

Figure 5-17 shows the leakage current waveform during the progression of a line of streamer discharges of a textured sample from their inception at the upper electrode until the phenomenon ends with metal-arc discharges at the lower ground electrode. The graph is accompanied by the infrared records corresponding to different instants during the discharges progression.

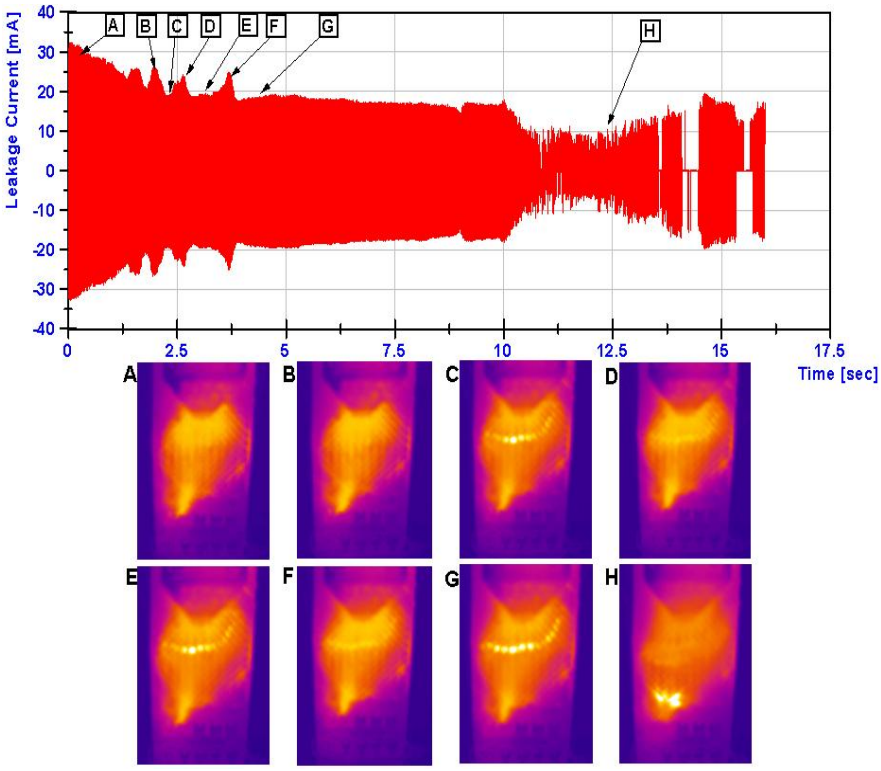

Figure 5-17. Leakage current waveform decay associated with the progression of streamer discharges and corresponding infrared images. The onset of streamer discharges is associated with leakage current valleys (C), (E) and (G) while current peaks (B), (D) and (F) occur when discharges extinguish. The event ends with metal-arc discharges (H).

Data analysis showed that the onset of the discharges spanning the dry-band is associated with a fall of leakage current. The correlation of IR records showing

active discharges spanning the dry-band corresponds to points of minima (valleys) of the leakage current waveform whereas when the discharges extinguish during progression, they correspond to points of maxima (peaks).

Figure 5-18 shows another current waveform record of the dry-band progression. In this case, the dry-band traversed the sample surface from its inception at instant A until it reached 8.5 s later the lower ground electrode at instant E. The waveform showed the characteristic decay shape with peaks and valleys. At the lower electrode, the current was further reduced and the discharges took the form of metal-arcs (instant F) until they self-extinguished and a new cycle of progression began.

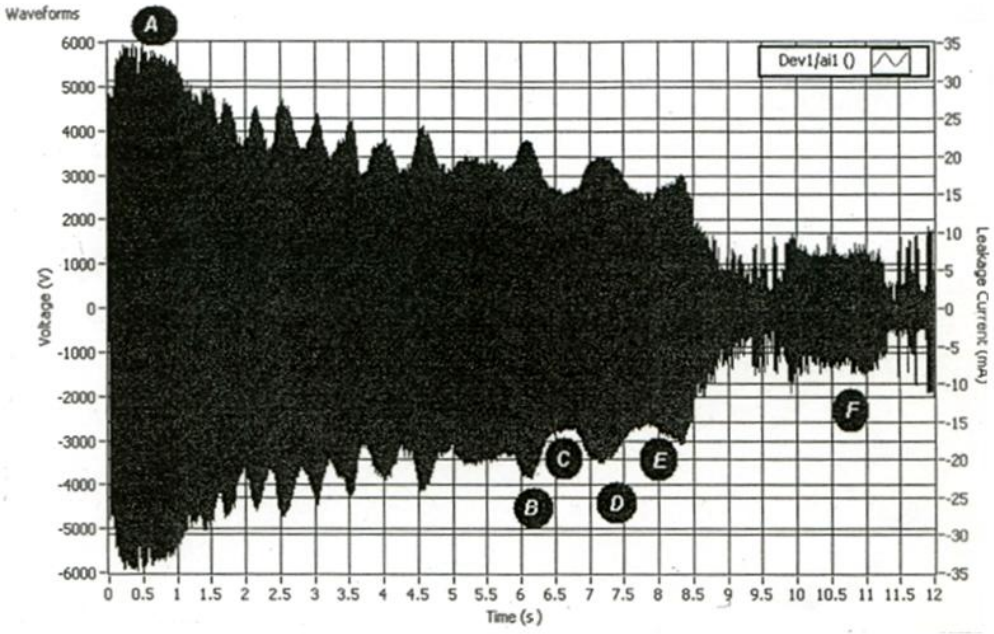

Figure 5-18. Data-logging of leakage current during the traverse of a dry band. Vertical scale 5mA/division. Time scale 12s.

Peaks, like those at instants B and D, were followed by current valleys, like those at instants C and E. Visible streamer discharges matched current valleys whereas intervals of no visible discharges were correlated with instants of peak currents. These intervals were attributed to a temporary re-wetting of the dry-band by the contaminant stream.

Figure 5-19 shows current waveform cycles corresponding to the 3 main instants observed during the progression of the line of discharges for a textured sample: peaks, valleys and discharges. The waveform starts as a sinusoid for the

points of maximum indicating conduction current in the polluted layer, while it became more distorted with nearly flat sections around zero when streamer discharges appeared. The wave shape got even more distorted when the discharges turned from streamer to arcing type at the lower electrode.

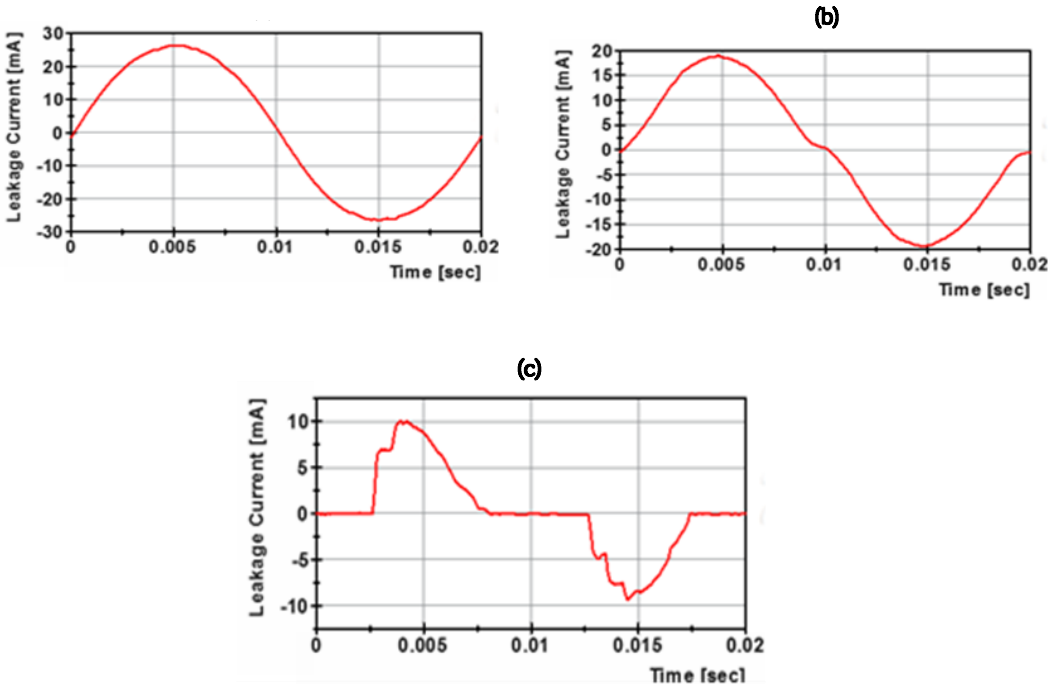

Figure 5-19. Current waveforms of leakage current during the advance of a line of discharges corresponding to (a) peaks (b) valleys of leakage current and (c) arcing-like discharges

These current logs suggested that the discharge channel conductance was less than the conductance of the pollution layer. From Figure 5-18 and the data points corresponding to peak values, the pollution layer conductance decay can be approximated by:

$$i_L(t) = 32.5e^{-0.075t} \text{ mA} \qquad (5\text{-}1)$$

The combined conductance of the pollution layer and the discharges also decayed during the dry-band progression. From the valleys data points:

$$i_{LD}(t) = 26.6e^{-0.08t} \text{ mA} \qquad (5\text{-}2)$$

Figure 5-20 presents the decay of both the pollution layer and the combined pollution layer and discharges current conductance for the case of Figure 5-18.

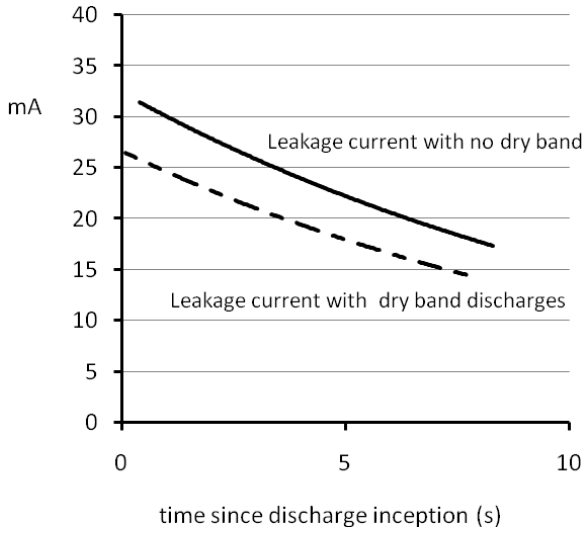

Figure 5-20. Current decay trendlines for the case of Figure 5-18.

(a) Contaminant layer conductance

The current decay described with Equation 5-1 is a result of the reduction of the conductance of the pollution layer. The layer conductance is reduced due to evaporation caused by the ohmic heating on the sample surface as revealed by the IR records. If we assume that the evaporation rate, and thus the layer conductance, is proportional to power loss, then

$$\frac{dG_L(t)}{dt} \propto -U^2 G_L(t) \tag{5-3}$$

which would indicate

$$G_L(t) = G_L(0)e^{-kU^2 t} \tag{5-4}$$

This is consistent with the current logs and the observed decay of current. For a test voltage of 3.5 kV, the measured leakage current displayed in Figure 5-18 gives an initial conductance value of 6.6 μS that falls to half-value after 8 seconds.

(b) Combined discharge-layer conductance

The ratio between the leakage current during the presence of discharges and the current when the discharges are absent is

$$\frac{i_{DL}(t)}{i_L(t)} = 0.82e^{-5\cdot 10^{-3}t} \cong 0.8 \tag{5-5}$$

The ratio is, therefore, constant and equal to 0.8 for the duration of 8 seconds. This means that the combined conductance of the contaminant layer and the discharges, $G_{DL,}$ is lower than the conductance of the layer alone, $G_{L,}$ and it falls from 5.4 μS to 2.7 μS during this time.

If we represent the combined conductance as the conductance of the layer in series with the conductance of the discharges (Figure 5-21) then

$$G_{DL} = \frac{G_L \cdot G_D}{G_L + G_D} \tag{5-6}$$

and the discharges conductance will be

$$G_D = \frac{G_{DL} \cdot G_L}{G_L - G_{DL}} \tag{5-7}$$

The discharge conductance, therefore, falls from 29 μS at t=0s to 13 μS at t=8s. If there are several discharges bridging the dry-band, these values are the sum of the conductance of each individual discharge spanning the dry-band.

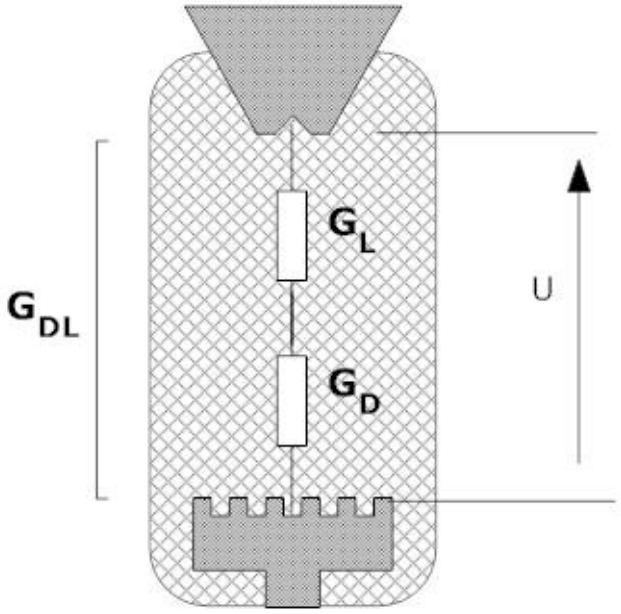

Figure 5-21. The combined conductance of the pollution layer with the presence of dry-band discharges represented by the conductance of the layer in series with the conductance of the discharges.

(c) Modelling of the discharges

The voltage U_D across the dry band when bridged by the discharges is

$$U_D = \frac{G_L}{G_L + G_D} U = 0.18U = 630\ V\ rms \tag{5-8}$$

For the 4mm intersecting square pattern, the dry-band discharge tends to follow the edges of the protuberance intersections. Therefore, the length of the discharge path is

$$Discharge\ path\ length = \frac{\pi \cdot (protuberance\ diameter)}{2\sqrt{2}} = 4.44 \text{ mm} \tag{5-9}$$

Therefore, the peak voltage gradient along a discharge would be

$$E_D = \frac{\sqrt{2} \cdot 630\ V}{4.44\ mm} \cong 200\ V/mm \tag{5-10}$$

The peak voltage gradient along the 50mm of the pollution layer is

$$E_L = \frac{\sqrt{2} \cdot 3500\ V}{50\ mm} \cong 100\ V/mm \tag{5-11}$$

The peak voltage gradient along the discharge is, therefore, significantly greater than the peak gradient along the leakage path of the pollution layer, thus causing the fall of current during dry-band discharging.

(d) Comparison with the streamer-spark model

The measured fall of voltage of 630 V in Equation 5-8 is in good agreement with the predicted voltage for dry-band breakdown described by the streamer-spark model [2.20]. According to this model, a discharge channel length (C+S) comprises a channel C (gradient 100 V/mm) and the associated streamer S (gradient 500 V/mm). For a.c. arc reignition, it is estimated that the length ratio C/S to be 5:1. Thus, for (C+S) =4.44 mm, the voltage drop across the discharge will be

C= 3.7 mm, S= 0.74 mm and

U_D = 0.74 mm x 500 V/mm + 3.7 mm x 100 V/mm =740 V

which is of the same order given by the experimental value of 630 V (Equation 5-8). The model also predicts that the current will be described by the relationship

$$i_D = 0.46(C + S) \quad [A \cdot m] \quad or \quad 2.05\,mA \tag{5-12}$$

which is lower than the experimental values measured that were in the range of 15-30 mA. However, the measured currents may be the sum of currents of parallel discharges. Overall, the experimental results support a model of a low-current, small-scale spark development.

(e) Comparison with the arc model

An alternative approach would be to ascribe to the dry-band discharge a partial-arc characteristic [2.21, 22] of the form

$$U_D = \frac{N \cdot L_D}{i_D^n} \tag{5-13}$$

Using the typically employed values of N = 10^4 and n = 0.5, this gives the discharge gradient for the initial discharge current of 26.6mA as

$$\left.\frac{U_D}{L_D}\right|_{arc} = 61\,V/mm \tag{5-14}$$

But this is lower than the maximum gradient of 100 V/mm in the pollution layer, and would not be consistent with the reduction in current observed with the dry-band discharges. On the contrary, it would represent a runaway flashover condition. The nature of Equation (5-13) does allow, however, adjustment of the empirical constants N and n to represent better the test data.

5.6 Conclusions

The inclined-plane tests of silicone rubber samples experimentally explored the improvement introduced by surface texturing in terms of resistance against erosion and tracking. The tests showed that all textured samples successfully passed the inclined-plane test, whereas none of the conventional non-textured samples made of the same material passed the same test. In particular, the 4mm and 6mm intersecting square (Texture C) configurations were the most

successful as they managed to suppress erosion and tracking damage with the least material loss compared with the other textured patterns. For this reason, these patterns were chosen to be employed for the design, manufacturing and testing of full insulator prototypes. These are further investigated in the next chapter.

The superior performance of these textures was attributed to the significant difference in discharge behaviour of textured samples compared with the non-textured samples. This improvement was attributed to the formation of stable dry-bands in the pollution layer and the parallel streamer discharges across the dry-bands. These discharges follow the protuberance intersections that were aligned at 45^{o} to the electric field for Texture C. Ancillary current measurements revealed that the more uniform distribution of leakage current and a high mobility of discharges across the ground electrode significantly reduced thermal damage for the textured samples. The infrared records confirmed the current measurements as they revealed a more uniform distribution of current for the textured samples whereas non-textured samples are characterised by a higher current density at the narrow region of the pollution stream, resulting in severe damage.

Current measurements also showed that the inception of the parallel discharges across the moving dry-band for textured samples was associated with a fall rather than an increase of leakage current and that the conductance of the pollution layer when the discharges are present is lower than the conductance of the layer with no discharges. The limitation inhibited the instability observed for non-textured samples where intense arcing caused severe damage.

The reproducibility and stability of the dry-band formation along with the current records captured by the data acquisition system allowed the calculation of voltage-current characteristics of the dry-band discharges. These experimental data fitted more the spark-streamer model rather than the arc model.

Chapter 6. Performance of textured silicone rubber insulators under polluted conditions

Introduction

The material tests described in Chapter 5 concluded that the 4mm and 6mm intersecting square designs were the most promising textured patterns for the development of a full insulator prototype. In this chapter, the design, manufacturing and testing of full textured insulators are presented.

The profile of the textured prototypes was based on the Type 1 conventional insulator described in Chapter 3. Textured insulators with a 4 mm square texture in the shank regions were prepared. A further logarithmic 4mm spiral ridge was added to the underside of the four sheds in another design. A 6mm version of each design was also manufactured.

Stereolithography models of the four prototypes were manufactured using a rapid prototyping machine. The textured insulators were cast in-house using silicone rubber moulds and vacuum injection casting techniques.

The textured insulators were later tested in clean-fog according to the test procedures applied for the testing of conventional silicone rubber insulators described in Chapter 3. The aim was to assess the flashover performance of textured insulators and to compare it with the performance of their conventional counterparts. Digital camera and infrared camera recordings were also employed to monitor the development of discharge activity and dry-band formation. It was normally possible to correlate the voltage and current data acquired with LabVIEW and the processed data with these events.

Textured insulators generally showed an improvement of flashover voltage compared with conventional silicone rubber insulators under the same test conditions. The scale of that enhancement varied depending on the design, the housing material and the test conditions. The best results were achieved for the 4mm textured shank design under conditions of heavy pollution and heavy

wetting that reached 26% compared with conventional samples made of the same material and under the same conditions of pollution severity and wetting.

As in the case of testing conventional insulators, textured prototypes manufactured using material B showed higher flashover voltages than material A. The improvement introduced by surface texturing for insulators made of material B ranged from 2% to 9 %. This reduced performance is interpreted as due to the higher hydrophobicity of material B. This also suggests that texturing may be a protection for conditions of loss of hydrophobicity that can occur for silicone rubber insulators.

All insulator prototypes were based on the design profile of Type 1 conventional silicone rubber insulator that was presented in Chapter 3 (Figure 6-1).

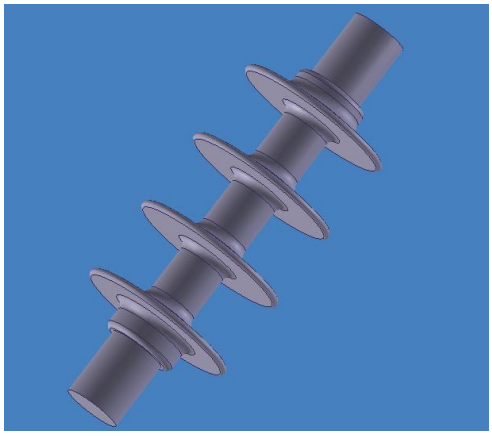

Figure 6-1. Type 1 conventional 11 kV silicone rubber insulator design.

6.1 Textured insulators designs

6.1.1 Textured shank design (TS)

The textured shank (TS) design employed the intersecting square texture pattern on the shank regions of the insulator. The top sides of the insulator sheds were left unchanged with a smooth surface to assist the draining of water and to avoid a possible accretion of pollution after long service in the system.

The design was developed for 4mm and 6mm protuberance sizes. The design with a 4mm intersecting square pattern on the insulator shank was assigned the name TS4 (Textured Shank 4mm) while the design with the 6mm size was assigned the name TS6 (Textured Shank 6mm) (Figure 6-2).

The creepage distance of the textured shed (TS) design was 471 mm compared with the 375 mm for a conventional Type 1 insulator.

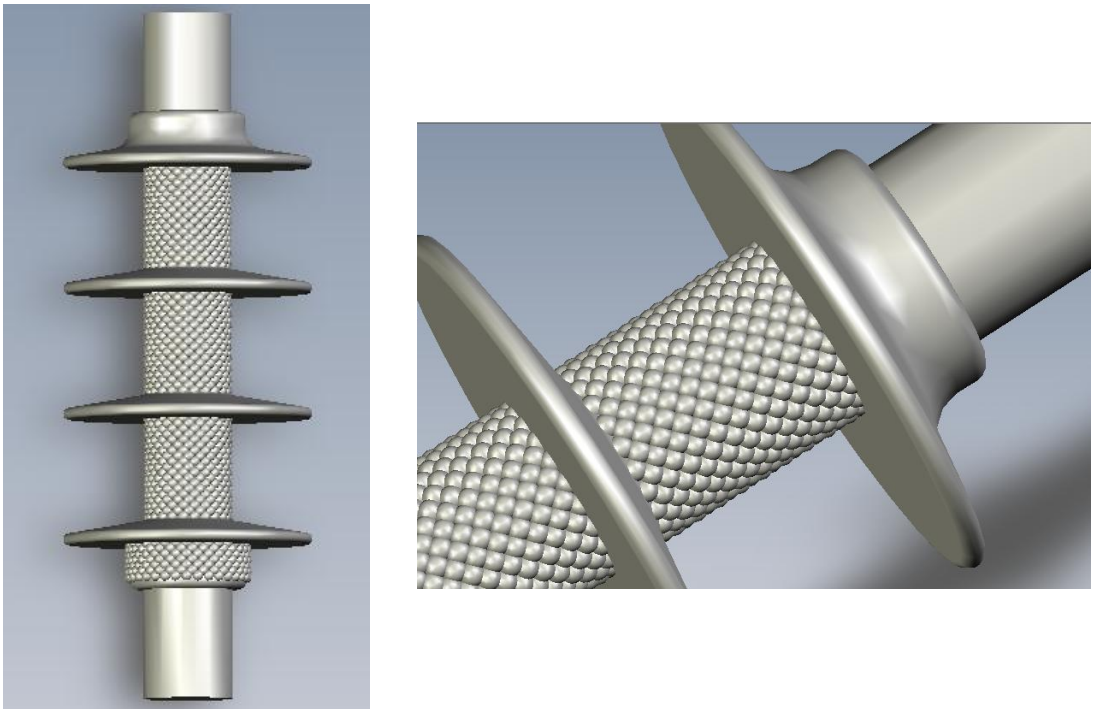

Figure 6-2. Textured shank design (TS)

6.1.2 Textured shank and shed design (TSS)

The superior performance of the intersecting square texture compared with the other textures tested in the inclined-plane test series was attributed to the 45° angle of the protuberances intersections with respect to the electric field. Unlike the cylindrical surface of the shank, it was not possible to achieve a regular, square intersection configuration of hemispherical protuberances (of constant size) which is oriented at 45° to the radial voltage gradient at an insulator shed underside. In this case, an alternative texturing with 45° orientation and a similar increase of the creepage distance and a decrease of leakage current density could be obtained with a logarithmic (Bernoulli) spiral pattern of semi-cylindrical ridges.

In polar coordinates r, θ, the logarithmic spiral equation is (Figure 6-3):

$$r = r_o \cdot e^{\left(\frac{\theta}{\tan\varphi}\right)} \qquad (6\text{-}1)$$

where φ is the constant angle between the tangent to the spiral ridge and the radial coordinate r.

The voltage gradient across an insulator shed is in the direction of the radial coordinate r, so the constant angle φ is set at π/4. In figure 6-3 such a spiral for tanφ=1 is shown, so that for this anticlockwise spiral, the normalised radial coordinate is:

$$\frac{r}{r_o} = e^{\theta} = e^{\alpha + n\beta} \qquad (6\text{-}2)$$

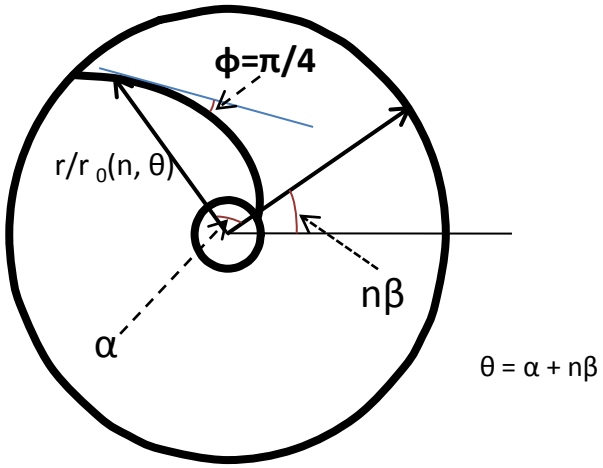

Figure 6-3. Logarithmic spiral (anticlockwise, φ=π/4)

The angular interval β between successive ridges is chosen to provide alignment and continuity with the texture of the square-pattern shank, at the junction between the shank and the shed underside.

In the case of TSS4 design, the radii of the inner and outer boundaries were chosen to fit the radial shank and shed dimensions of the test insulator Type 1.

The number of ridges that could fit the insulator shank:

- Shank circumference = $2\pi r_o$ = 84 mm
- Number of ridges = 84mm/4mm =21

Therefore, the angular interval was:

- $\beta = \frac{2\pi}{21}$ radian = 0.3 radian

From Equation 6-2 and for r = Shed radius= 45 mm and r_o = shank radius = 13.37 mm :

$$\alpha = \ln(45/13.37) = 1.204 \text{ radian} \quad (6\text{-}3)$$

Therefore, the length of each spiral is determined by the angular range of

$$0 \leq \alpha \leq 1.204 \text{ radians} \quad (6\text{-}4)$$

The inner end of each spiral replaced the top row of the protuberance on the shank; the outer ends were spherically profiled.

Therefore, for the family of spirals between 13.37 mm ≤ r ≤ 45 mm, defined by this range of the parameters n and α, the polar coordinates θ are calculated from

$$\theta = n\beta + \ln\frac{r(\alpha)}{r_o} \quad (6\text{-}5)$$

Figure 6-4. Shed underside ridge pattern (anticlockwise, φ=π/4)

A more uniform ridge pattern over the shed underside could be achieved by a nested pair of spiral structures of the type shown in Figure 6-5, where the intermediate outer-spiral ridges are calculated by amending β to a value of 0.21 radian, and calculating θ for a more limited range of 27mm ≤ r(α) ≤ 45 mm. This pattern introduced a total of 42 ridges for each shed underside for the TSS4 design, 21 ridges of a 13.37 mm ≤ r ≤ 45 mm range and 21 ridges of a 27mm ≤ r(α) ≤ 45 mm range. The total number of ridges increased further to a total of 66 ridges on the bottom shed underside for its larger diameter (r_o = 21 mm). 33

ridges have a length within by the range 21 mm≤ r(α) ≤ 45 mm and the remaining 33 nested ridges have a length in the range 35 mm ≤ r(α) ≤ 45mm.

The textured shank and shed design (TSS) employed this double-ridge pattern along with the texturing of the shank regions. Figure 6-6 shows the TSS4 design along with a zoom detail of the ridges and their joining points with the shank texture.

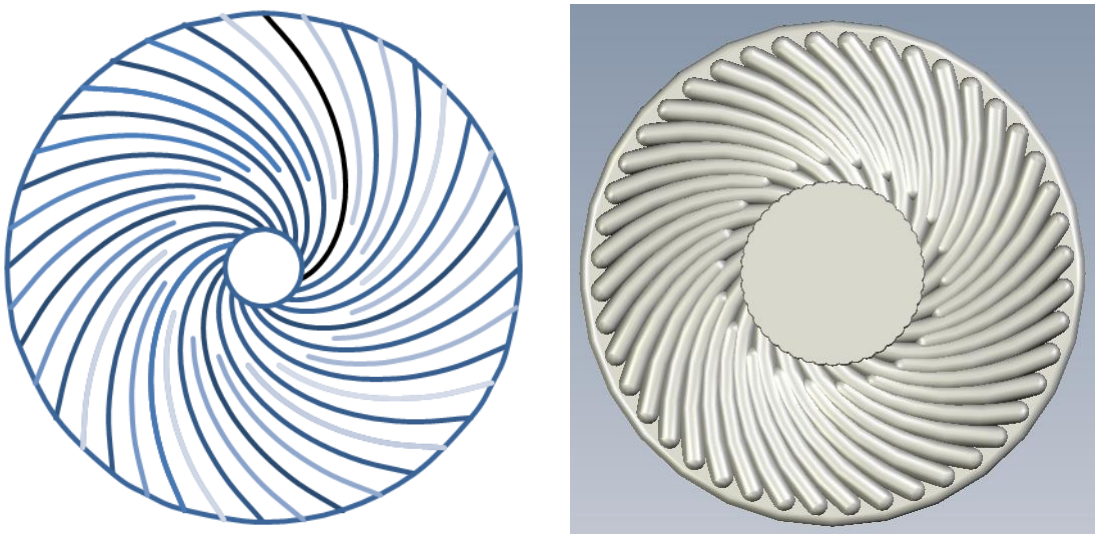

Figure 6-5. Shed underside double-ridge pattern (anticlockwise, φ=π/4).

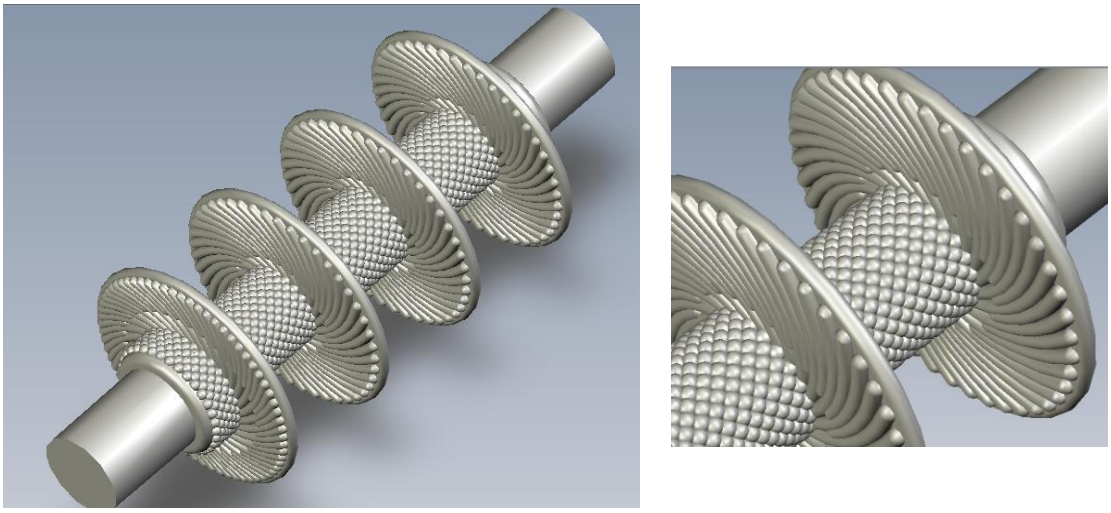

Figure 6-6. The TSS4 textured insulator prototype design (left) and zoomed detail of the double ridge pattern of the shed underside and the junction with the shank square texture (right).

The TSS6 design was similarly developed with a protuberance and ridge size of 6 mm. With this larger size, a total of 28 ridges for the top three sheds and 44 for the bottom shed, were fitted (Figure 6-7).

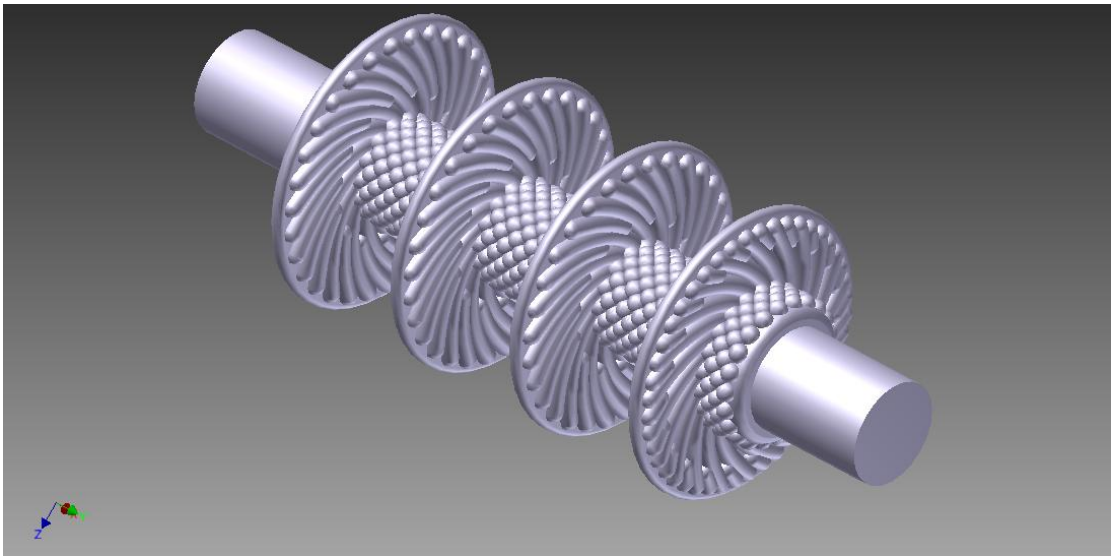

Figure 6-7. The TSS6 textured insular design

The creepage length for the textured shank and shed design was further increased compared to the textured shank only design, and this was 503 mm. It is worth noticing that the creepage distance is independent of the hemisphere radius.

Table 6-1. Creepage distance for conventional and textures insulators.

Insulator design	Creepage distance (mm)
Conventional Type 1 (CON)	375
Textured shank 4mm (TS4)	471
Textured shank & shed 4mm (TSS4)	503
Textured shank 6mm (TS6)	471
Textured shank & shed 6mm (TSS6)	503

After the designs were completed, they were given to the Manufacturing Engineering Centre (MEC) of Cardiff University to produce the stereolithography (SLA) models that would be later used to manufacture the silicone rubber moulds for the casting of the textured insulators.

6.2 Stereolithography models of textured insulators

The stereolithograhy models would serve as the positive samples for the manufacturing of the silicone rubber moulds. The SLA models were built using a SLA 5000 3D material printer within the Manufacturing Engineering Centre (MEC) at Cardiff School of Engineering. Layers of photosensitive resin are scanned by a UV laser according to the 3D CAD design loaded in the 3D printer. The regions scanned by the laser are locally solidified. When a layer is complete, the building platform lowers to expose a new layer of resin ready to be scanned by the UV beam, gradually building up the model. The maximum resolution of the building layer is 0.05 mm and the laser wavelength is 354.7 nm. Four SLA models, corresponding to the four textured insulator designs, were manufactured.

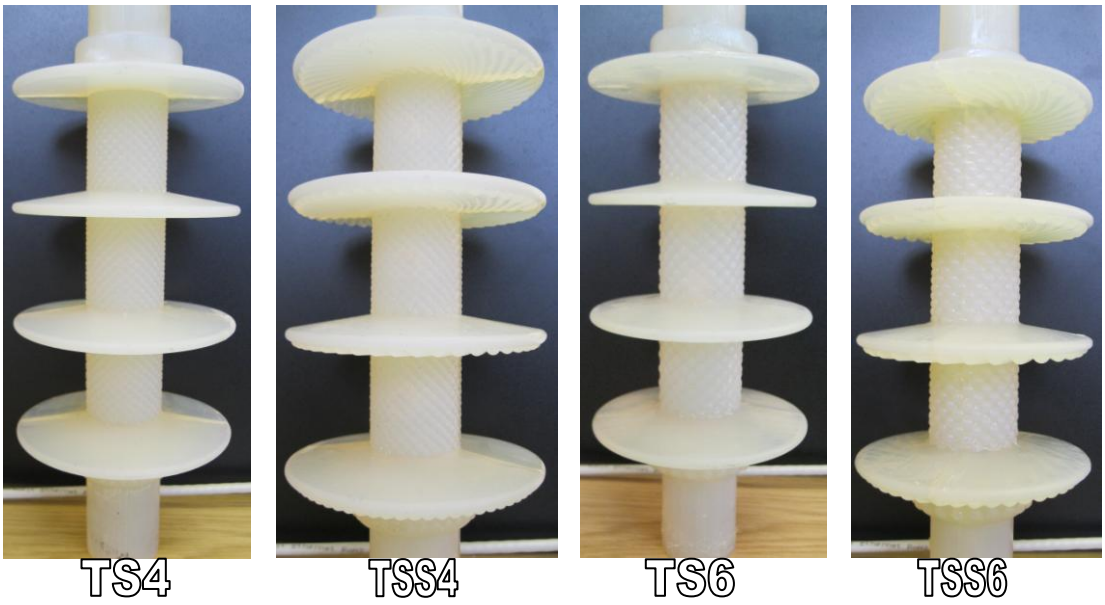

Figure 6-8. The four SLA models for the textured insulators prototypes.

Each model was manufactured in two parts along the axial length. The two parts were later assembled and glued together. Any gap between the two parts was sealed using a glue resin. The model was later cleaned and inspected for any obvious inconsistencies. When it was confirmed that the SLA models passed the quality inspection, they were ready to be used for the manufacturing of the silicone rubber moulds.

6.3 Manufacturing of silicone rubber moulds

The silicone rubber used for the manufacturing of the silicone moulds was MTT VTV 750 transparent silicone rubber with VTV-CAT 750 catalyst with a mixing ratio of 10:1. Table 6-2 shows the specifications of VTV 750.

Table 6-2. Specifications of VTV 750 silicone rubber

TYPE		***VTV 750***
COLOUR		TRANSPARENT
MIXING RATIO	By weight	10:1
VISCOSITY	MPa*s/25^{0}C	1000
POT LIFE	Min at 25^{0}C	120
CURING TIME	h/^{0}C	24h/25^{0}C
HARDNESS	Shore A	40
TENSILE STRENGTH	kp/cm^2	45
ELONGATION	%	300
TEAR STRENGTH	kp/cm	17
SPECIFIC GRAVITY	25^{0}C	1.08

A moulding box made of chipwood parts was designed and constructed to mount the SLA model in a horizontal position. A structure made of bronze rods and a plastic rod was mounted with the help of a glue-gun to reproduce the ventilation channels and the injection gate respectively. The injection gate was positioned at the upper shank section and the rest of the shank sections and sheds had a one ventilation channel each (Figure 6-9).

Figure 6-9. Moulding box with the SLA model in position for the manufacturing of silicone rubber moulds.

For the preparation of the silicone rubber, 3000g of resin and 300g of catalyst were used. The materials were manually mixed in a casting drum for 5 minutes. The casting drum was then placed in the MCP 5/01 vacuum casting machine for degassing. As vacuum is achieved gradually in the casting chamber, the trapped air bubbles start to escape from the mix, giving rise to the silicone mix almost until the top of the drum. Before overflowing the drum, the silicone collapsed back to the bottom of the drum and was left another 10 minutes in vacuum.

After removal from the casting machine, the silicone was poured carefully in the moulding box, making sure that each area of the model was covered with a minimum of 15 mm thick silicone layer. The moulding box was placed in the casting machine for secondary degassing for 25 minutes.

Figure 6-10. Secondary degassing in the vacuum casting machine (left). A mould for cylindrical samples during secondary degassing in vacuum, showing the trapped air escaping the silicone rubber (right).

The mould was then cured at 50^{o}C for 10 hours. After removal from the curing oven, the ventilation and injection gate rods and the chipwood structure were removed. The cured mould was then cut open in two halves. A line was drawn along the axial length of the model to be used as a cut guide. The cut is performed with a sharp scalpel and a pair of special pincers. The cut had a wave-shaped edge to ensure the correct positioning of the two halves during casting.

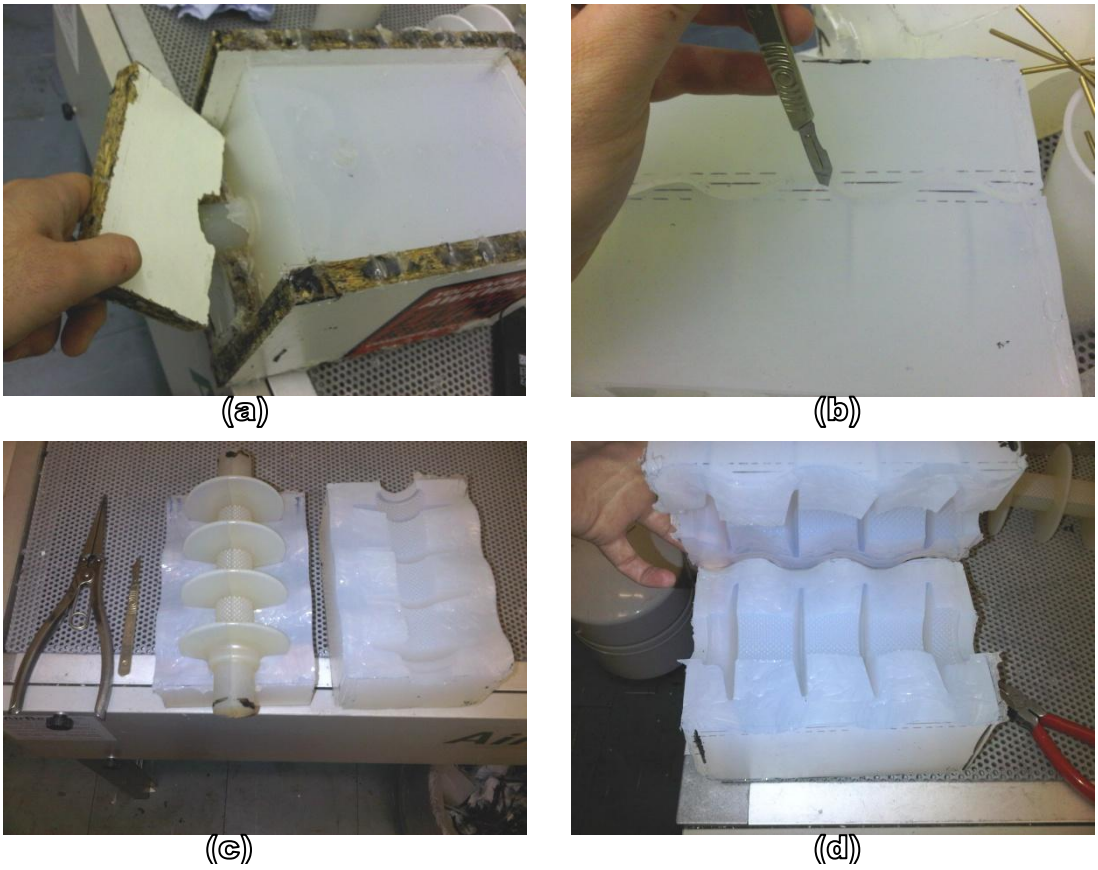

Figure 6-11 .Removing the chipwood box (a), wave-shape cut along the axial length of the model (b), the mould separated in two halves (c & d).

The mould was inspected for any signs of damage and then the ventilation and injection paths were cleared of any silicone. The mould was placed back to the oven at 50^{o}C for 2 hours for post-curing (Figure 6-12). The moulds lifetime depends on the number of castings and can be used to produce 6-10 insulator prototypes if they are well maintained.

Figure 6-12. Clearing the ventilation and injection channels (left) and a completed silicone mould (right).

6.4 Casting of textured insulators using silicone moulds

The silicone rubber preparation and the vacuum casting procedure, described in section 3.2 for a steel mould, was followed for the case of silicone rubber moulds. However, special provisions were taken for the preparation of the silicone rubber mould.

The silicone mould was cleaned thoroughly to remove any material left from previous castings or other contaminants. It is important to verify that the ventilation and injection channels are not blocked. Silicone rubber from previous casts tends to get trapped in these channels, not allowing the air bubbles escaping from the mould cavity during casting.

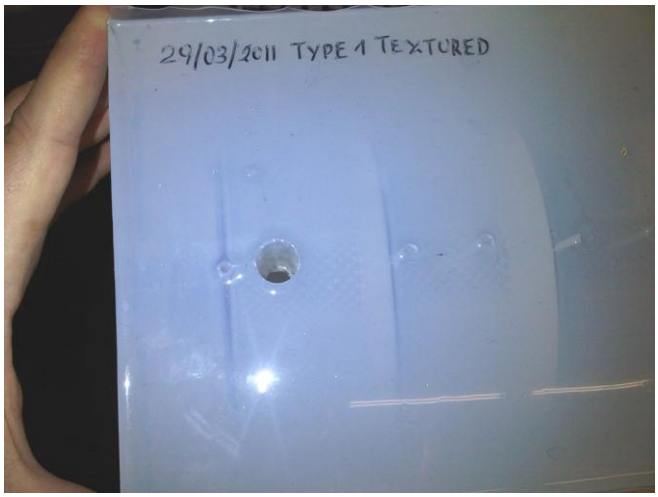

Figure 6-13. Injection gate and ventilation channels of a silicone rubber mould

Silicone rubber for the casting of insulators, unlike the case of metal moulds, tends to adhere to the silicone rubber mould. A thorough lubrication of the silicone mould is crucial for the quality of the cast and the lifetime of the mould. If the mould is not lubricated or regions remain without a lubricant, the silicone rubber injected in the silicone mould will eventually bind with the mould during curing. The retrieval of the cast becomes impossible or the cast is severely damaged and the mould incapacitated (Figure 6-14).

A spray wax release agent, ALCHEMIE R5, was sprayed on the mould cavity to form a very thin layer. The release agent was sprayed from a minimum distance of 50 – 60 cm to ensure a uniform thin layer. For this reason, it is difficult to

lubricate the deep shed regions that are more susceptible to entrap the cast. A thin layer of Vaseline, using a small brush, was used to grease the sheds.

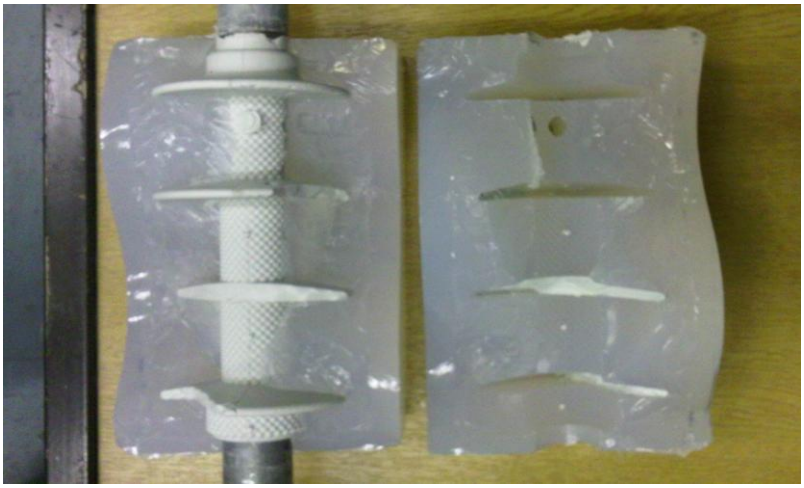

Figure 6-14. Example of damaged cast and mould as a result of poor mould lubrication.

After the mould was lubricated, the core was placed in position and the mould sealed with adhesive tape, leaving the ventilation and injection channels unblocked.

After casting, the adhesive tape was removed and the mould was opened gently to avoid damaging the cast. The insulator was removed from the mould and both were thoroughly cleaned with hot water and a clean wipe cloth to remove any grease.

6.5 Textured insulators prototypes

Figure 6-15 shows the textured insulators that were cast in the high voltage laboratory using vacuum casting techniques. All 4 mm designs (TS4 and TSS4) were cast using material A silicone rubber and all 6 mm designs (TS6 and TSS6) were cast using material B.

The test insulators were constantly inspected after clean-fog tests for any signs of damage on the silicone rubber housing such as material erosion induced by the intense discharge activity. Such a defect could affect the flashover performance of the test sample, hence such a sample was retired, the housing removed and the metal fittings/core reused to cast a new insulator (Figure 6-16).

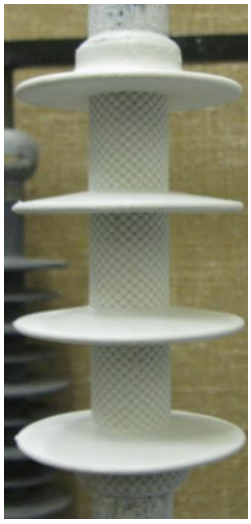			
TS4A	**TSS4A**	**TS6B**	**TSS6B**

Figure 6-15. The textured insulators prototypes.

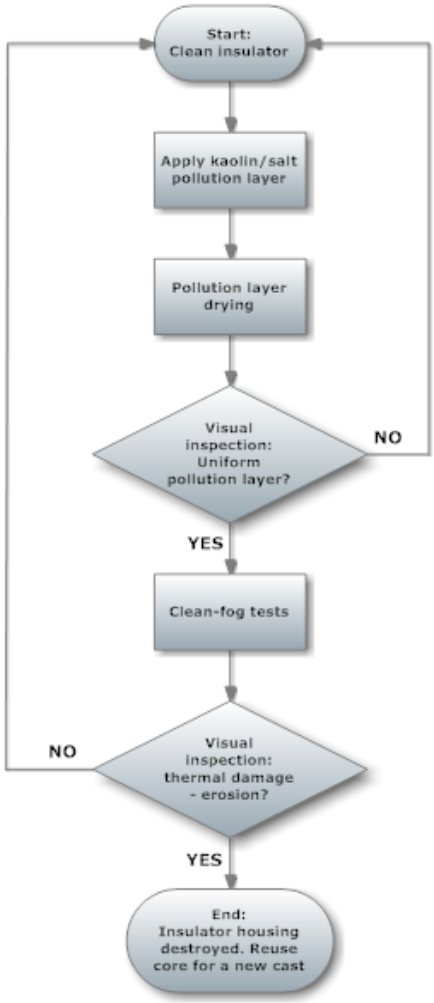

Figure 6-16. Flowchart of test insulator inspection.

6.6 Test methods

The textured insulators were tested in clean-fog to assess any improvement introduced by textured surfaces to the flashover performance compared with the conventional Type 1 silicone rubber insulators. The textured insulators were tested under the same conditions of pollution severity and surface wetting as the conventional insulators to allow the comparison of the flashover voltage levels. The pollution severity was expressed as the volume conductivity of the kaolin/salt/wetting agent pollution suspension used to pollute the test insulators. The Sony Handycam digital camera and the FLIR infrared camera, described in section 3.3, were employed to monitor the discharge activity, the surface heating and to detect any dry-bands that may form on the insulator surface as observed for the conventional insulators.

The data acquisition system described in section 3.1.3 was used to perform current measurements during the clean-fog tests and capture records of the test voltage and current records.

The flashover performance was assessed following the ramp voltage test protocol described in Chapter 3. The test voltage was controlled by the Hipotronics motorised supply and increased steadily with a 4 kV/minute rate following a ramp pattern until flashover occurred.

The ramp voltage tests performed were for:

- High pollution (11.2 S/m) and high fog rate (8 litres/hour)
- High pollution (11.2 S/m) and low fog rate (3 litres/hour)
- Low pollution (4.0 S/m) and high fog rate (8 litres/hour)
- Extremely high pollution (19.9 S/m) and low fog rate (3 litres/hour)

The textured prototypes, like the conventional insulators, were polluted according to the procedure described in sections 3.41 and 3.4.2.

6.7 Test results – Discussion

6.7.1 Flashover performance summary for textured insulators

Table 6-3 shows a summary of the ramp voltage tests results for textured insulators along with the results for conventional insulators and the improvement of flashover voltage introduced by textured surfaces for each case.

Table 6-3. Summary of ramp voltage tests for textured and conventional insulators

	Insulator	Number of ramp voltage test series	Total number of flashovers[1]	Average flashover voltage [kV][1]	Standard deviation[1]	F.O. level improvement compared with CON
High pollution (11.2 S/m) and high fog (8 l/h)	CONA	5	20	28.3	4.4	-----
	TS4A	6	24	34.3	5.6	**21 %**
	TSS4A	6	24	35.6	5.3	**26 %**
High pollution (11.2 S/m) and low fog (3 l/h)	CONA	6	24	28.6	3.3	-----
	TS4A	7	28	33.2	5.1	**16%**
	TSS4A	6	24	34.4	5.9	**20%**
	CONB	5	20	33.3	6.0	-----
	TS6B	7	28	33.8	5.8	**2%**
	TSS6B	6	24	36.2	6.1	**9%**
Low pollution (4.0 S/m) and high fog (8 l/h)	CONA	1	4	41.2	6.8	-----
	TS4A	1	4	44.9	3.6	**9%**
Extremely High pollution (19.9 S/m) and low fog rate (3 l/h)	CONA	2	8	24.9	6.2	-----
	TS4A	1	4	28.6	3.2	**15%**
	TSS4A	1	4	29	6.5	**16%**
	CONB	1	4	29	8.9	-----
	TS6B	1	4	30.7	8.0	**6%**
	TSS6B	1	4	30.7	8.7	**6%**

[1] Only the first 4 flashover events of each ramp voltage tests series.

For all insulators, the results showed that material B exhibits an increased flashover performance compared with insulators manufactured with material B. This was attributed to a higher hydrophobicity of material B.

As can be observed in Table 6-3, textured insulators can offer an increase of the flashover performance up to 26 % in the case of the TSS4A design compared with the average flashover voltage of CONA insulator under conditions of high pollution and high fog rate. The performance in general seemed to be affected by both the housing material and the test conditions.

While TS4 and TSS4 designs made of material A show constantly a significant improvement compared to CONA insulators, TS6 and TSS6 prototypes made of material B show a lesser improvement compared to CONB insulators. Moreover, none of the textured insulators underperformed compared to the conventional design. It could be consistent with the design concept that a textured surface would be more effective under conditions for which hydrophobicity is lost, an event that may be observed for silicone rubber insulators during service.

The maximised performance of TS4A and TSS4A designs under conditions of heavy pollution (11.2 S/m) and heavy wetting (8 litres/hour) in conjunction with the relatively small improvement observed under lighter pollution (4.0 S/m) again indicates the effectiveness of textured designs.

6.7.2 High pollution (11.2 S/m) and high fog rate (8 litres/hour)

Figure 6-17 shows the average curves of the ramp test series of TS4 and TSS4 insulators. Each series consists of 8 flashover events. The average curve for the same tests of conventional insulators is also shown for comparison. The volume conductivity of the pollution suspension was 11.2 S/m while the applied fog rate was set to 8 litres/hour.

The flashover voltage of both TS4 and TSS4 insulators showed a U-shape at the start of the ramp test series. The average flashover for the 2nd flashover event is lower than that for the first flashover. From the 3rd flashover onward, the flashover level recovered and steadily increased. This minor fall was attributed to the complexity of the surface geometry of textured insulators that required more time to get fully wet. It must be noted that a similar U-shape was observed for the conventional insulator at a lower fog rate (section 4.4.3), confirming that the layer wetting is the cause of this temporary depression of flashover voltage. The flashover increased because of the gradual washing of the pollution layer,

resulting in an increase of the layer resistance, and the residual surface heat caused by previous flashovers.

The maximum standard deviation for TS4 was observed for the 1st event, was 6.6 kV and the minimum standard deviation was observed for the 8th event, at 1.8 kV. For the TSS4 design, the maximum standard deviation was observed for the 3rd event and was 7 kV and the minimum for the 8th event, 3.8 kV.

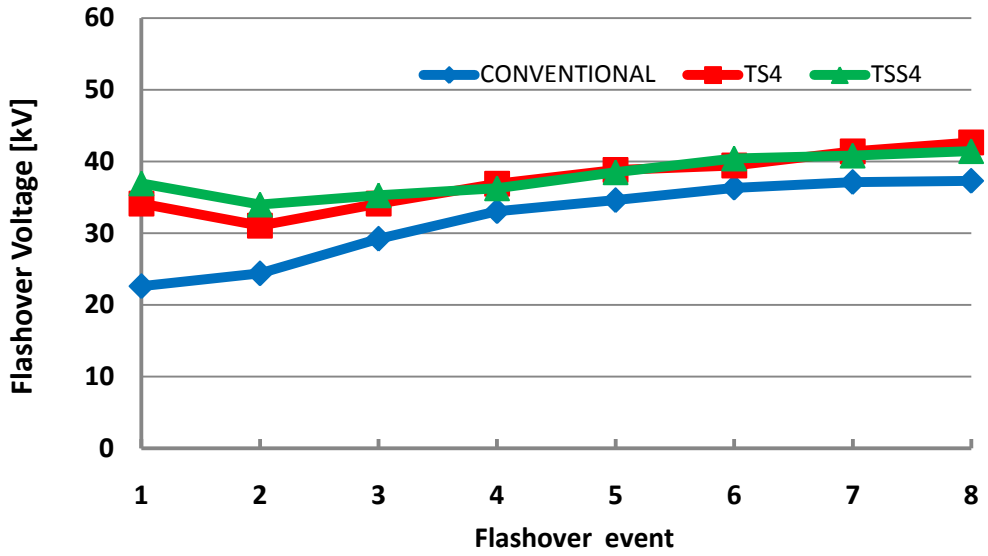

Figure 6-17. Average curves for TS4 and TSS4 insulators. Each ramp voltage test series consists of 8 flashovers. The average curve for CONA insulators is also presented for comparison.

The average flashover curve for the conventional insulator is consistently lower than that of TS4 and TSS4. The first 4 flashover events are very important as they simulate line conditions where a polluted insulator in service is gradually wetted by a morning fog or mist. The average flashover voltage for the first four shots was 34.3 kV for the TS4 insulator, a value 21% higher than the 28.3 kV found for the conventional insulator. For the TSS4 insulator, the average flashover voltage for the first four flashovers was 35.6 kV, 26% higher than the conventional insulator.

6.7.3 High pollution (11.2 S/m) and low fog rate (3 litres/hour)

Figure 6-18 shows the average flashover curves for TS4A and TSS4A insulators under pollution of high pollution, 11.2 S/m, and low fog rate, 3 litres/hour. As all 4mm designs were manufactured using only material A, the results were

compared only with the performance of the conventional insulators made with the same material, CONA.

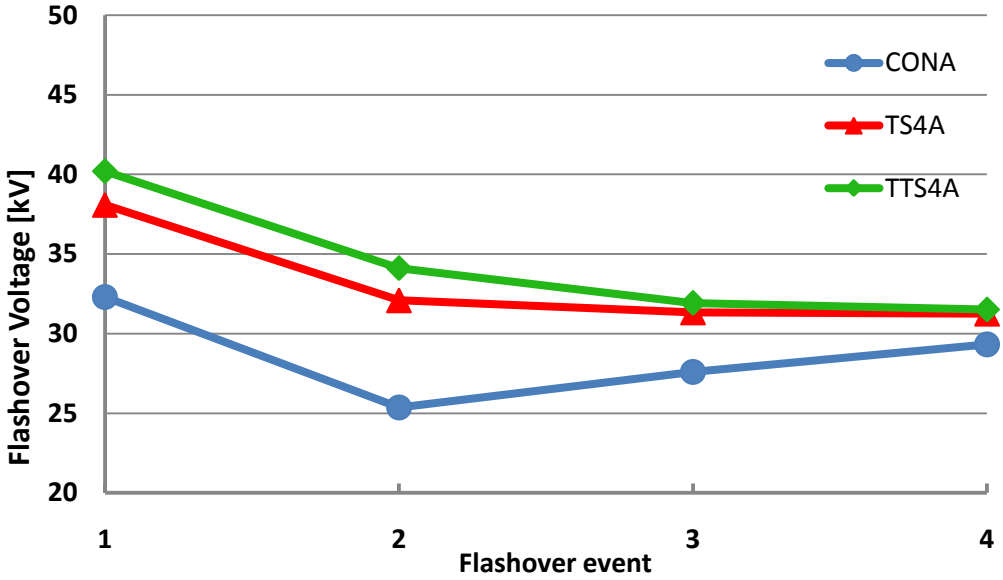

Figure 6-18. Average curves of 7 ramp voltage test series for TS4A insulators and 6 ramp voltage test series for TSS4A insulators under conditions of high pollution, 11.2 S/m, and low fog rate, 3 litres/hour. Each ramp voltage test series consisted of 4 flashovers.

The flashover voltage for both TS4 and TSS4 insulators was reduced for the 2nd flashover event compared to the 1st flashover and it did not recover for flashover events 3 and 4. By the 4th flashover event, the flashover voltage for both textured insulators converged to that of the conventional insulator.

The average flashover voltage for the TS4 design and for all 28 flashovers was 33.2 kV, 16% higher than the respective average flashover voltage for the conventional design. For the TSS4 design the improvement was slightly higher reaching 20% with an average of all 24 flashovers being 34.4 kV.

Figure 6-19 shows the average flashover curves for the TS6B and TSS6B insulators compared with the performance of conventional insulators made of material B.

The average flashover voltage for the TS6 design and for all 28 flashover voltages was 33.8 kV, whereas for the TSS6 design and for all 24 flashovers was 36.2 kV indicating a 2% and 9% improvement compared to the conventional insulator.

This lesser improvement observed for the 6mm designs was attributed to the more hydrophobic material B. As described in Chapter 4, material B was more hydrophobic than material A. Conventional insulators made of material B (CONB) showed a 16% higher average flashover voltage compared to conventional insulators made with material A (CONA). Therefore, it was perhaps not so surprising that texturing did not introduce the evident performance observed for the designs manufactured with silicone A.

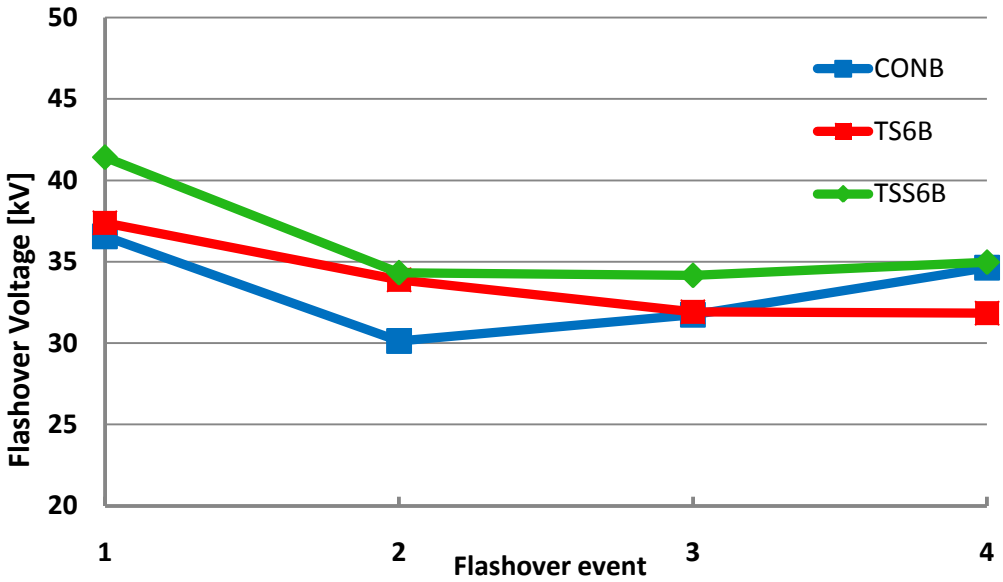

Figure 6-19. Average curves of 7 ramp voltage test series for TS6B insulators and 6 ramp voltage test series for TSS6B insulators under conditions of high pollution, 11.2 S/m, and low fog rate, 3 litres/hour. Each ramp voltage test series consisted of 4 flashovers.

6.7.4 Effect of fog rate on the flashover performance

The effect of fog rate on the flashover voltage was investigated by comparing the flashover performance of the TS4A and TSS4A insulators for high pollution (11.2 S/m) and for both high (8 litres/hour) and low fog rate (3 litres/hour).

Figure 6-20 shows the average flashover curves for CONA, TS4A and TSS4A insulators. The curves with continuous lines correspond to 8 litres/hour while the dashed lines are for 3 litres/hour. The minimum average voltage for TSS4 was 34 kV for high fog which dropped to 31.5 kV for low fog.

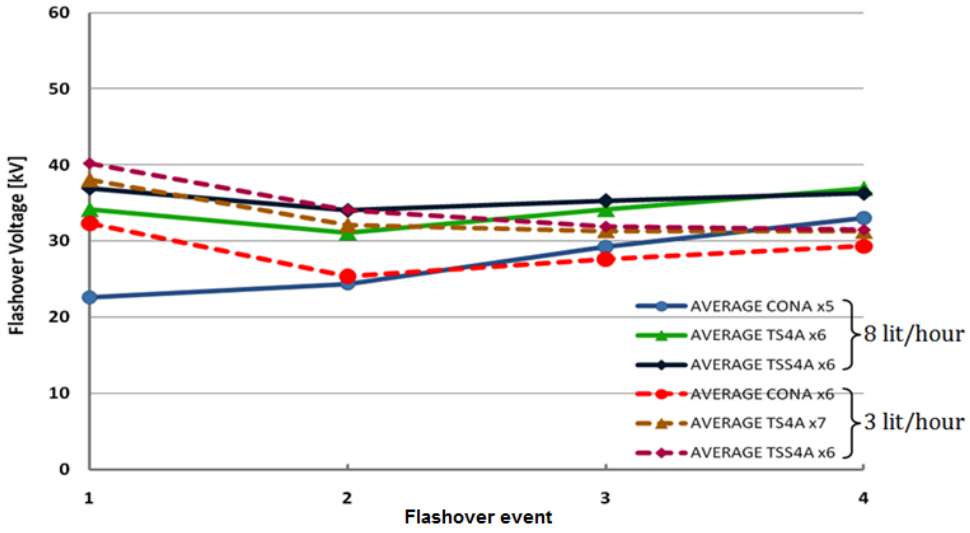

Figure 6-20. The effect of fog rate on the flashover performance of textured insulators.

Figure 6-21 shows the effect of fog rate on the average flashover voltage for each design. While conventional insulators appear to be unaffected by the applied fog rate, the average flashover voltage is depressed for low fog by approximately 1 kV for TS4 and TSS4 insulators suggesting that a slower humidification of the pollution layer makes them more vulnerable to flashover.

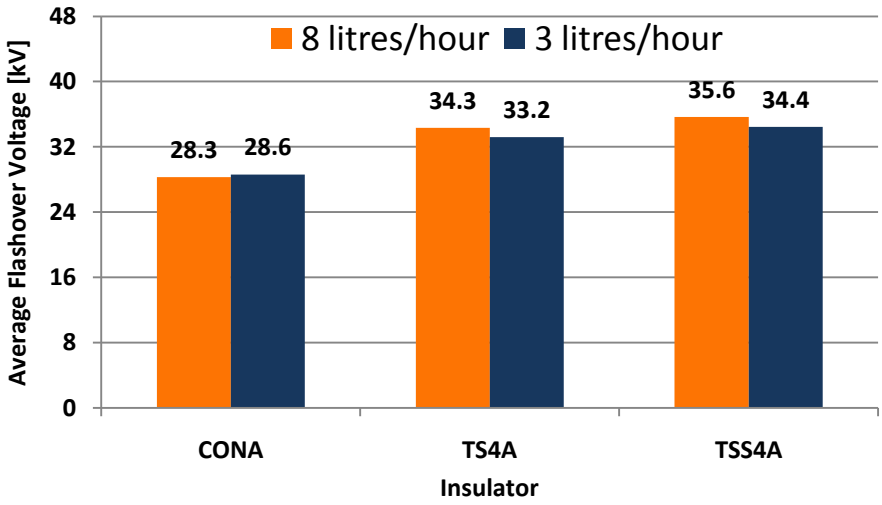

Figure 6-21. Effect of fog rate on the average flashover level for CONA, TS4A and TSS4A for 11.2 S/m pollution level.

6.7.5 Low pollution (4.0 S/m) and high fog rate (8 litres/hour)

A single ramp voltage test series was performed for a TS4A insulator with low pollution salinity where the pollution suspension has a volume conductivity of 4 S/m. The fog rate was 3 litres/hour. Figure 6-22 shows the flashover voltage

curve for TS4A and CONA for low pollution and also the average flashover curve for TS4A for a pollution level of 11.2 S/m.

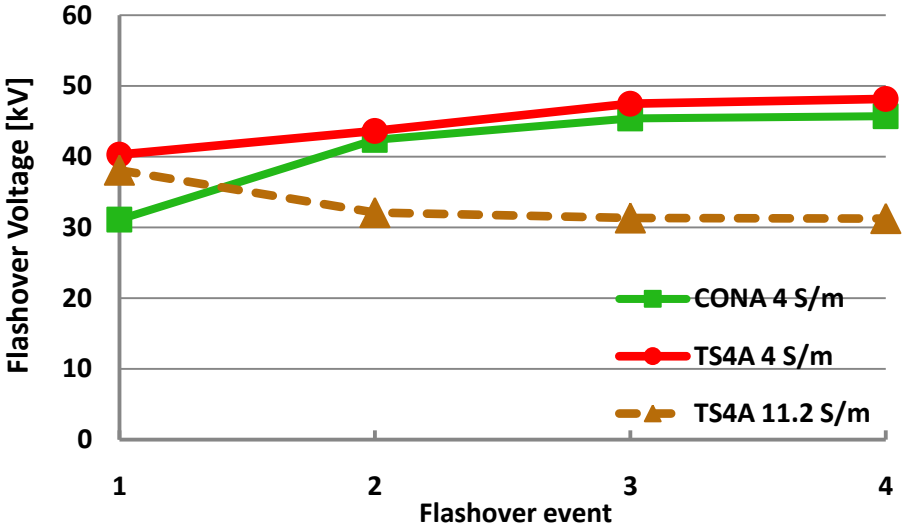

Figure 6-22. Ramp voltage test series for a TS4A and CONA insulator for low pollution salinity (4 S/m).

The flashover voltage of TS4A for low pollution was, as expected, significantly higher that the flashover performance of the same insulator for high pollution. However, the improvement introduced by texturing compared with the CONA insulator for low pollution was not significant as the average flashover voltage of TS4A was only 9 % improved compared with CONA for a low pollution level.

The experimental exploration of the textured insulators' flashover performance made of silicone A under different conditions of pollution severity and fog rate application revealed that the greatest enhancement occurred for conditions of both high pollution and high fog rate. Therefore, it was suggested that a limited number of ramp voltage tests should be performed using saline solution of higher conductivity to investigate the possible improvement introduced by texturing under conditions of extremely heavy pollution.

6.7.6 Extremely high pollution (19.9 S/m) and low fog rate (3 litres/hour)

The pollution suspension volume conductivity was increased to 19.9 S/m to investigate the behaviour of textured insulators for an extremely high pollution. The fog rate was set to 3 litres/hour. A limited number of tests for CONA, CONB, TS4A, TSS4A, TS6B and TSS6B were conducted. The flashover performance was compared for insulators made of the same silicone material. Figure 6-23 and 6-

24 show the flashover curves for the group CONA, TS4A, TSS4A and the group CONB, TS6B, TSS6B respectively.

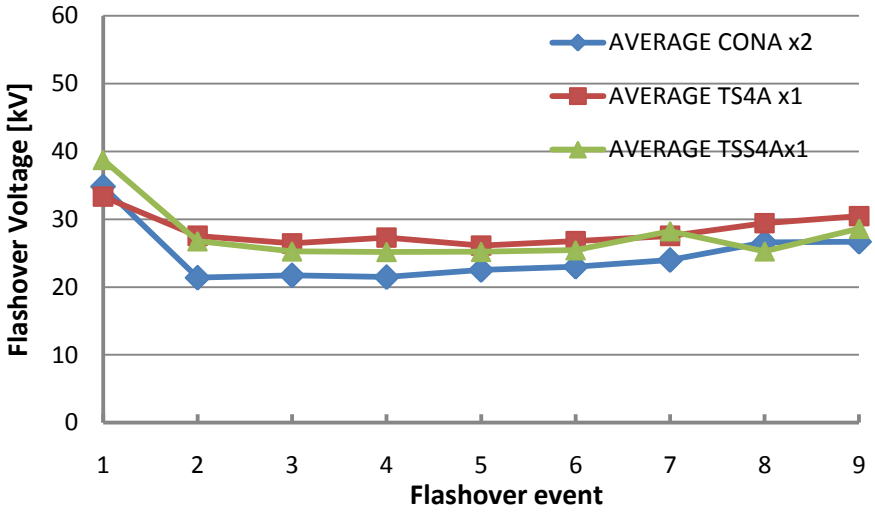

Figure 6-23. Flashover curves for CONA, TS4A and TSS4A for ramp voltage tests under conditions of extremely high pollution, 19.9 S/m, and low fog, 3 litres/hour.

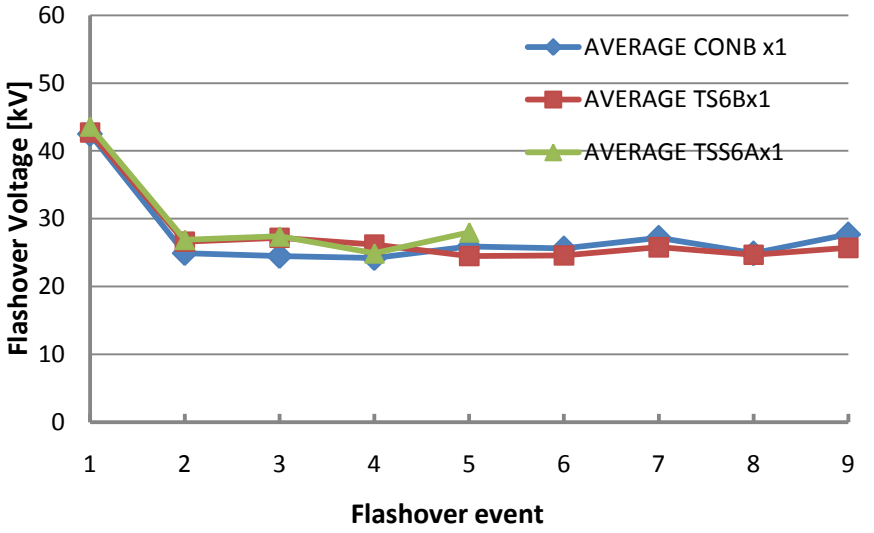

Figure 6-24. Flashover curves for CONB, TS6B and TSS6B for ramp voltage tests under conditions of extremely high pollution, 19.9 S/m, and low fog, 3 litres/hour (for the TSS6B design, the ramp test series consisted of 5 flashover events).

For the CONA, TS4A and TSS4A designs, the average flashover voltage for the first 4 shots was 24.9 kV, 28.6 kV and 29 kV respectively. Therefore, both 4mm textured designs had an average flashover voltage approximately 15 % higher than the conventional insulator made of the same material. Further, the minimum flashover point for TS4A was 26.4 kV, for TSS4A was 25.2 kV and for

CONA was 21.4 kV. From this perspective that takes into account the minimum flashover voltage, thus the worst case scenario, the flashover performance of TS4A was improved by 23% and for TSS4A was improved by 18 %.

For the insulators designs made with material B, i.e. CONB, TS6B and TSS6B, the average flashover voltage for the first 4 flashover shots was 26.9 kV, 30.7 kV and 30.7 kV respectively. The improvement was 14 % for both TS6B and TSS6B compared with CONB. The minimum flashover voltage was 8 % higher than the minimum flashover voltage of CONB, and 4 % for TSS6B.

The extremely high pollution tests confirmed that the best improvement was observed for the TS4A and TSS4A designs. For the TS6B and TSS6B designs, the improvement was higher than the average flashover voltage recorded for the 11.2 S/m ramp voltage tests.

6.8 Current records

The LabVIEW data acquisition system was used to store the waveforms of the applied voltage and the leakage current in files. These files were post-processed to calculate electrical properties. The data were analysed with a time window of 20ms (cycle duration at 50Hz) and 2 sec (the duration of 100 cycles at 50Hz).

(a) 20 ms window

Figure 6-25 shows an example of the calculated electrical properties of root mean square (rms) of the test voltage and leakage current, the average power and energy over one cycle of a typical ramp voltage test for a TS4A insulator. This example is the 12^{th} ramp voltage of a ramp voltage test series.

For each individual flashover of a ramp voltage test series, the leakage current increased along with the constantly increasing ramp voltage until flashover occurred (Figure 6-25).

The average power maximum pre-flashover peaks reached 100 W, and it was not uncommon to reach 1.3 kW, especially upon the inception of spark discharges.

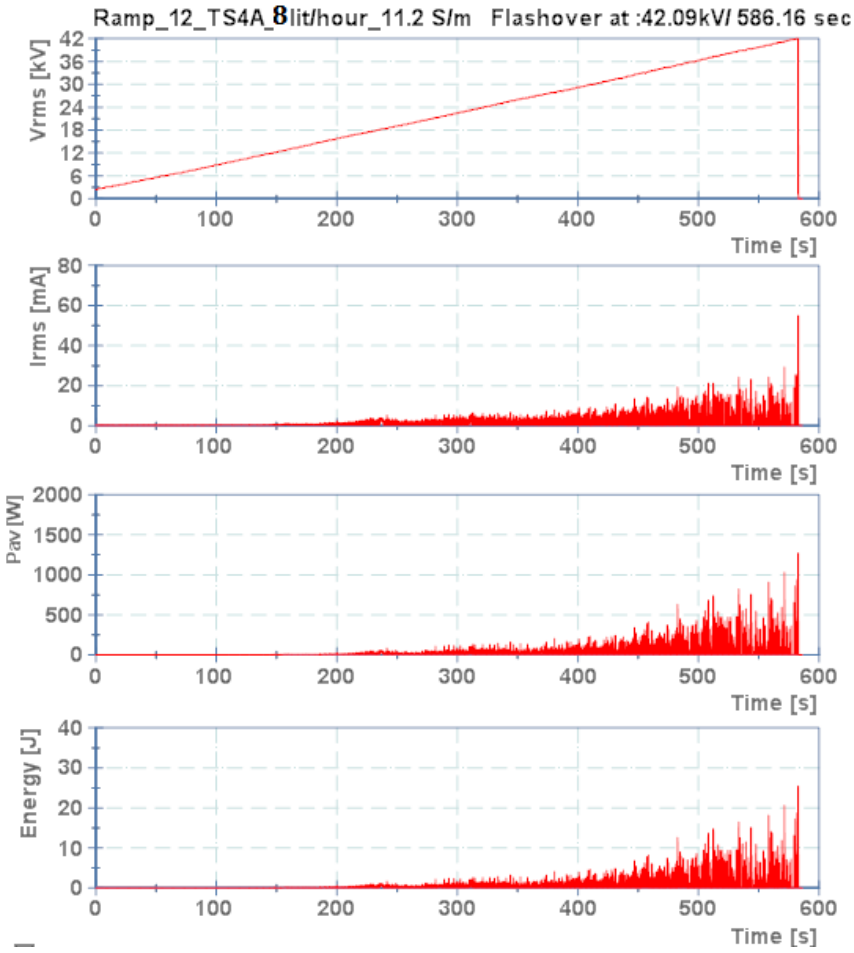

Figure 6-25. Example of current voltage-current records of a ramp voltage test for a TS4A insulator. The calculated average power and energy are also presented.

The measured power confirmed the layer heating and the heating of discharge transients detected by the infrared camera. Energy peaks followed the same trends like average power exceeding 20 Joules before flashover.

The development of current from ramp to ramp however, excluding an initial increase from the 1st to the 3rd ramp, was different as it gradually decreased due to the washing of the pollution layer. The inverse relationship between the flashover voltage and the layer conductance was confirmed once again for the textured insulators clean-fog tests (Figure 6-26).

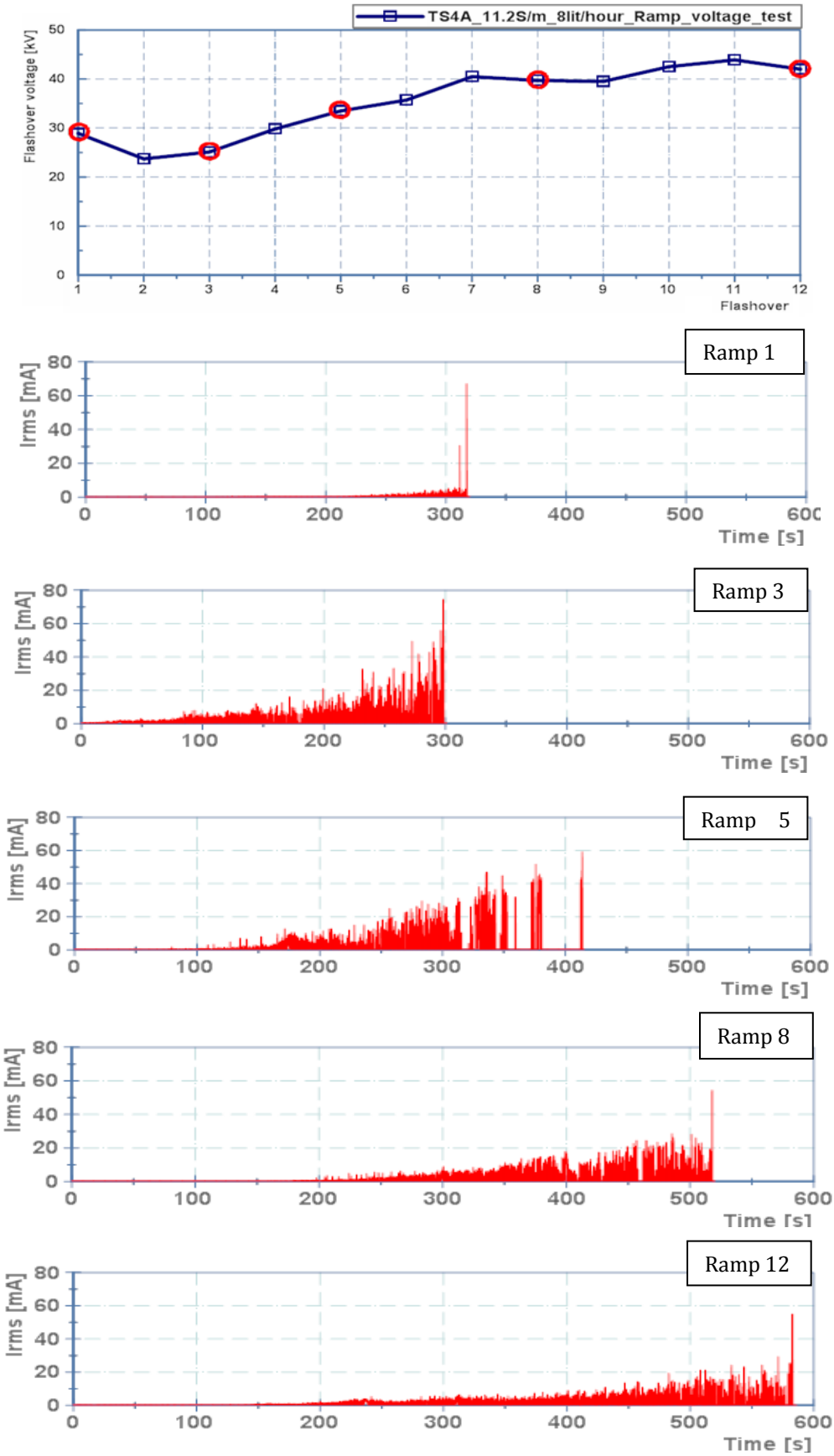

Figure 6-26. Current development for a ramp voltage tests series (TS4A insulator, 11.2 S/m and 8 litres/hour): Ramps 1, 3, 5, 8 and 12.

Figure 6-27 shows a comparison between the 20 highest current peaks for a conventional insulator, CONA, and a TS4A insulator for different ramp voltage test series. The current peaks are presented in a descending order of the current peak magnitude. The figure shows that the textured insulator shows lower current peaks than the conventional insulator for all test series. This could explain the highest flashover performance of the textured design.

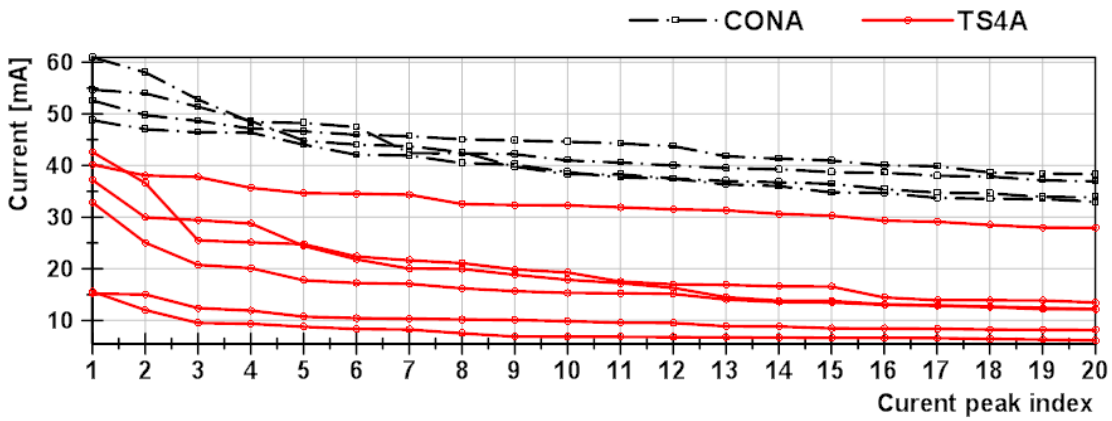

Figure 6-27. 20 highest current peaks in a descending order for the conventional insulator and the 4mm textured shed design. Each curve corresponds to the third ramp of a ramp test series. Pollution level 11.2 S/m and fog rate 3 litres/hour.

(b) 2 sec window

As in the case of conventional insulators, the current data were analysed for a 2 seconds window. Figures 6-27 shows an example of the test voltage, the current, the number of peaks N_p, the ratio $I_{rms}/N_{p,}$ the average power P_{av} and the ratio $P_{av}/N_{p,}$ averaged for a 2 s window for a TSS4 insulator. The data are presented in an inverse order where x=0 corresponds to the instant of the flashover event.

For conventional insulators, a reduction of the discharge activity was observed before flashover occurred. While the same phenomenon is observed for textured insulators, it is not present as consistently as in the case of conventional insulators. This may suggest that surface texturing inhibits the growth of the dry-band width.

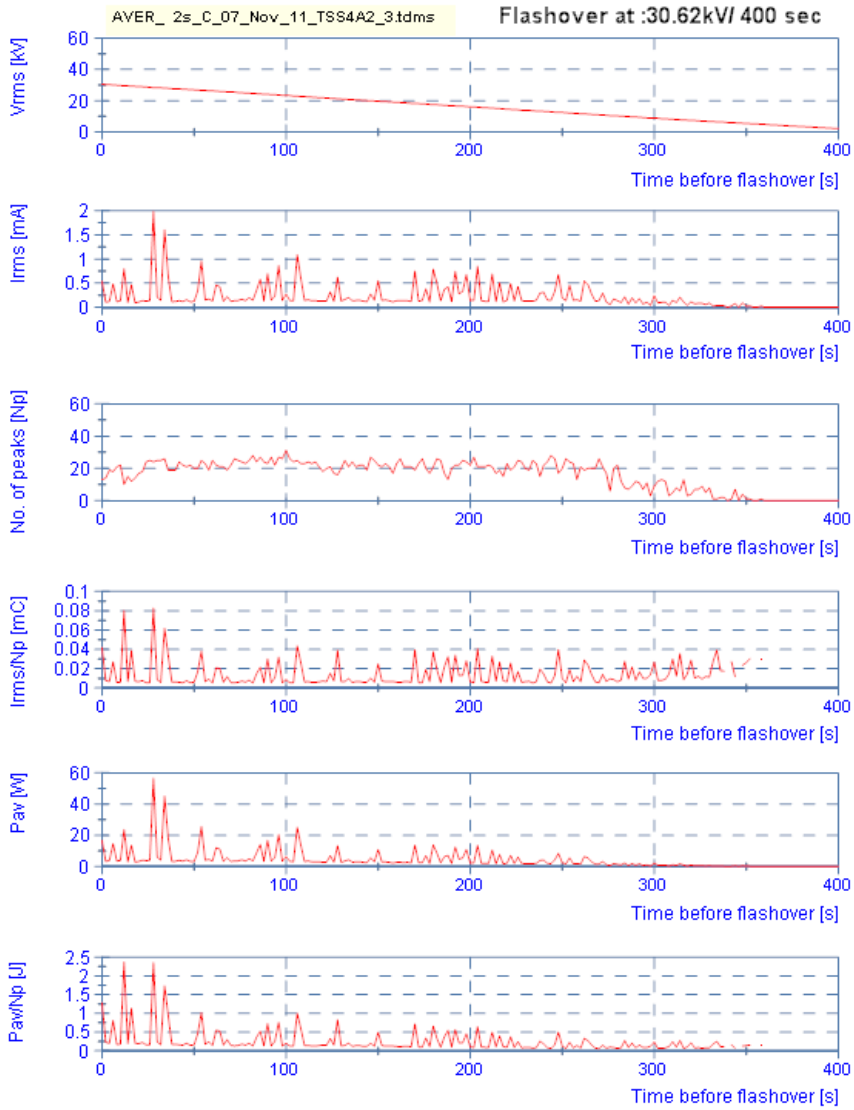

Figure 6-28. 2 seconds analysis of ramp voltage data for a TSS4A insulator, 3rd ramp (11.2 S/m and 3litres/hour).

6.9 Conclusions

The material tests showed that the intersecting square designs with a 4 mm and 6 mm protuberance diameter were the most promising textures for the development of a full insulator prototype.

Textured insulators were designed and manufactured in-house using silicone rubber moulds and vacuum injection casting techniques. The textured shank design (TS) employed a textured surface only at the shank regions. The textured shank and shed design (TSS) additionally included a textured shed underside comprised of a logarithmic spiral pattern. Both designs were developed for a 4mm and 6 mm protuberance size. The addition of the surface texturing resulted

to insulators of increased creepage length: 471 mm for the TS design and 503 mm for the TSS design compared with the 375 mm of the conventional insulator. This was achieved without increasing the overall length of the insulator.

The TS4 and TSS4 designs were cast using material A silicone rubber and TS6 and TSS6 designs were manufactured using material B silicone rubber. These materials were also used for the manufacturing of the conventional silicone rubber insulators described in Chapter 3.

The ramp voltage tests in clean-fog showed that the textured designs had a superior flashover performance compared with the conventional insulators. The TS4 and TSS4 insulators showed the best performance reaching 26 % whereas the prototypes made of material B, TS6 and TSS6, showed a lesser improvement, up to 9%.

The reduced performance of the 6mm designs may be a result of a more hydrophobic material B compared to material A. Material B showed a similar behaviour during the pollution tests for conventional insulators.

The best performance was obtained for conditions of heavy wetting and heavy pollution, thus suggesting that texturing is more effective under adverse conditions. Moreover, by comparing the performance of different materials, it could be suggested that surface texturing may be more effective during conditions of temporary loss of hydrophobicity that is observed for silicone rubber insulators in service.

Current records revealed that the TS4 design shows lower current peaks than the conventional insulator.

A large number of digital camera and infrared camera data have also been acquired during clean-fog tests of textured insulators and are currently being processed and correlated with the current data as part of the ongoing research programme.

Chapter 7. General Discussion – Conclusions – Future Work

The research programme described in the present work was very challenging not only in terms of technical difficulties that needed to be tackled but also for resolving issues related with different scientific disciplines ranging from software programming and vacuum injection casting to high voltage testing and product design.

The results of the experimental exploration of textured patterns to assess their anti-tracking and anti-erosion performance and of the flashover performance of full textured insulators in clean-fog tests were very promising. During the course of characterising textured designs for polymeric insulators, an investigation of the pre-flashover phenomena and the dry-band failure mechanism for silicone rubber insulators during clean-fog tests was conducted. A proposed test procedure, based on the Solid Layer methods of IEC-60507, was developed. For the monitoring of the test object, a data acquisition system was designed and set-up that allowed the screening and storage of leakage current data. Ancillary video and infrared camera recordings provided useful information for the interpretation of the test outcomes and the related physics.

In this chapter, a summary of the research conclusions is presented along with a brief in-depth discussion on the experimental results. Also, suggestions regarding the further development and testing of textured insulators for the future are described.

7.1 Clean-fog tests for conventional silicone rubber insulators

7.1.1 Test objects and test procedures

The test procedures for ceramic insulators are well-defined by international standards and are easily replicated. Unfortunately, this is not the case for polymeric insulators. The hydrophobic nature of the polymer housing does not allow the direct application of the test methods for ceramic insulators.

A proposed test procedure for clean-fog tests of polymeric insulators has been presented which is based on the Solid Layer method for ceramic insulators. It advocates the addition of a non-ionic wetting agent in the kaolin/salt pollution suspension as described in previous proposal from Cardiff University.

Two types of tests were performed depending on the type of the applied test voltage: ramp or constant voltage tests. For the former test, the test voltage followed a ramp pattern, with a steady increase rate of 4 kV / min. The ramp test is terminated when flashover occurs. A ramp test series comprised several individual ramp tests. For the constant voltage tests, the voltage was raised directly to a voltage level closer to the estimated flashover voltage and kept for 30 minutes. If a flashover occurred before the 30 minutes had elapsed, the test voltage would be immediately reapplied, but with a reduced magnitude by 2 kV. A withstand voltage is recorded when the insulator is able to withstand the stress for 30 minutes.

The ramp voltage test method was very replicable with consistent results and with the ability to detect and distinguish between different pollution levels and between different housing materials in terms of hydrophobicity. However, the constant voltage tests series results showed that the flashover level was significantly affected by the residual heat caused by previous flashovers. This 'memory' effect along with the unwelcomed prolonged exposure of the pollution layer to the washing effect of the fog, resulted in a limited number of constant voltage tests.

Recording the leakage current along with the applied voltage for the whole range of the high voltage tests until flashover was an aim of the research programme. For that reason, a data acquisition system was built to monitor and store in files the waveforms of voltage and current. The software was developed using National Instruments LabVIEW and provided high-resolution records of the leakage current and enabled the calculation of further electrical parameters. The correlation of leakage current data with the visual observations and the infrared records provided the evidence to interpret the flashover mechanism observed for clean-fog tests of full insulators, to confirm the different hydrophobic

properties of the housing materials and enabled the comparison with the electrical properties of textured insulators prototypes.

While digital camera recordings provided information for the development of spark discharging on the insulator surface during clean-fog tests, infrared camera photography provided information not visible to the naked-eye by recording the formation, maintenance and growth of dry-bands on silicone rubber insulators and their role in flashover failure. Examples of correlation between the digital camera, the infrared camera and the current records were presented. Such correlations between long exposure photography and infrared records revealed the position and growth of dry-bands on the insulator surface and the presence of small streamer discharges that are responsible for maintaining the dry-band which are normally invisible to the naked-eye.

The test objects were cast in-house using metal moulds and employing vacuum injection casting techniques. Two types of insulators were cast, Type 1 and Type 2 with a creepage length of 375mm and 530mm respectively. The vast majority of tests were performed using Type 1 insulators its shed profile was chosen to work as the blueprint for the development of a textured prototype. Type 2 insulators were used for preliminary tests. Two commercially available silicone rubber materials were used, material A and material B. While Type 1 insulators were manufactured using both materials, Type 2 insulators were exclusively cast using material A. For the purpose of optimising the test protocols and exploring the potential of the infrared camera, simple cylindrical prototypes were also cast and tested in the fog chamber. Manufacturing and testing conventional silicone rubber insulators was an essential stage towards the design and fabrication of textured insulators and understanding the pollution flashover behaviour of silicone rubber insulators in clean-fog tests.

Establishing a test procedure for non-ceramic insulators was of prime importance in order to evaluate the behaviour of conventional silicone rubber insulators before proceeding to testing of textured insulators prototypes.

7.1.2 Clean-fog tests conclusions

The flashover performance of silicone rubber insulators during clean-fog tests was investigated. The flashover voltage was significantly reduced with the increase of the pollution layer conductance that was associated with the controlled wetting of the layer. An inverse relationship between the flashover voltage and the layer conductance is found, and revealed by the U-curve variation of the flashover voltage. The flashover was found to gradually recover due to the pollution layer washing.

Test insulators made of material B showed higher flashover voltages compared with the flashover voltages of insulators made of material A. This was attribute to the superior hydrophobicity properties of material B. Measurements of the leakage current peaks showed higher current peaks for CONA insulators than CONB insulators, an indication which infers that material B is more hydrophobic than material A.

Spark discharge activity was monitored and recorded during clean-fog tests using a digital camera. More importantly, infrared photography provided comprehensive images of dry-band formation and development that is no visible with the naked-eye. Correlation of infrared images and the test voltage revealed that the dry-band width is increasing with increasing voltage.

Long-exposure digital photography revealed small-scale streamer discharges of low luminosity bridging the dry-band. These streamers are of low visibility in fog tests and are responsible for the continuous current flow and the heating of the dry-bands. The streamer discharges may initiate higher current discharges that could span longer sections of the insulator surface. Further increase of the test voltage and the dry-band width is accompanied by longer sparks of higher current magnitude that always precede flashover. It was observed that the spark activity may reduce just before flashover. Current records confirmed this observation.

The waveforms of test voltage and current were stored throughout the test. These data were later analysed for a 20 ms and 2 s time windows and other electrical parameters derived from current and voltage records were calculated.

Current records confirmed the inverse relation between the layer conductance and the flashover voltage. The current gradually decreased along with the longer exposure of the layer to the washing effect of the chamber fog. The 2 s window analysis showed that less discharges are present before flashover and these discharges are characterised by higher current/power peaks. The streamer current is limited by the presence of a high layer resistance. However, as the dry-bands grow in width and discharges span longer sections of the insulator, the overall series resistance is decreased thus allowing higher-current sparks that eventually result in flashover.

7.2 Material tests for textured samples conclusions

Materials that are assigned to manufacture insulators should be assessed for their ability to resist erosion and tracking induced by surface discharges. The IEC-60587 inclined-plane test is a well-established method for the evaluation of the anti-erosion and anti-tracking performance of insulating materials. Textured samples and conventional non-textured samples were experimentally explored to investigate the possible improvement introduced by surface texturing.

Rectangular silicone rubber samples, with dimensions 120 mm x 50 mm x 6 mm were manufactured using a commercial RTV silicone rubber. Samples with a plain surface and samples with a textured surface were cast. Three types of textured samples were manufactured: contiguous hexagonal, intersecting hexagonal and intersecting square. For the intersecting square design, a range of diameters were cast: 2, 4 , 6, 8 and 10 mm. The test voltage was constant and set to 3.5 kV r.m.s. while the contaminant was a water solution with ammonium chloride and a non-ionic wetting agent.

The inclined-plane tests, in accordance to IEC-60587, showed that the performance of textured designs, in terms of resistance against erosion and tracking, was outstanding. All textured samples, regardless the geometry configuration or the protuberance diameter, successfully passed the inclined-plane test whereas none of the conventional non-textured samples passed the test. This represents a 100% success rate for textured samples contrasting a

100% fail rate for non-textured samples which indicates that texturing improves the surface properties of polymeric materials.

From the textured designs, the 4mm and 6mm intersecting square patterns showed the best performance as the loss of material due to erosion was minimal. Therefore, these configurations were selected to be employed for the design and development of full textured insulators.

The superior performance of textured sample is attributed to the unique discharge behaviour associated with these designs compared with plain surface samples. Conventional samples tend to show arc-like discharges that anchor at certain regions near the lower ground electrode, inducing severe erosion and material loss. For textured samples, a stable dry-band formed near the upper electrode that is then bridged by a series of small streamer discharges. The dry-band along with the discharges moved along the sample surface towards the ground electrode. Near the ground electrode, the discharges became more elongated and eventually took the form of metal arc discharges. These arc-like discharges appeared briefly, and were very mobile contrasting the anchored arcs observed for conventional samples that caused severe damage. This pattern of advancing dry-band and discharges was repetitive throughout the inclined-plane test for most textured designs.

Current records showed that the inception of the streamer discharges was associated with a fall rather than an increase of the current. This indicated that the conductance of the pollution layer was higher than the combined conductance of the layer and the streamer discharges.

A modified version of the inclined-plane test was developed and investigated the multi-path current flow in textured insulators. The single ground electrode was replaced by five smaller, adjacent and separate electrodes. The conducting current for each electrode was monitored and stored in files. The data analysis revealed a more uniform distribution of the leakage current for the case of intersecting square samples compared with conventional non-textured samples. This was attributed to the ability of the textured design to provide multiple alternative conduction paths.

The data collected from the investigation of the stable dry-band and the associated streamer discharges allowed the comparison of the partial-arc model and the spark model for dry-band breakdown. This comparison inferred that the spark model fits better the experimental data.

7.3 Clean-fog tests for full textured insulators

Textured insulators were developed that utilised the intersecting square design. This pattern was chosen because it showed the best results during the inclined-plane test series.

A textured shank (TS) design employed the intersecting square pattern only at the insulator shank regions whereas a textured shank and shed (TSS) additionally included a logarithmic spiral texture at the shed underside. 4mm (TS4 and TSS4) and 6mm (TS6 and TSS6) designs were cast in-house using silicone rubber moulds and vacuum injection casting techniques. The 4 mm designs were manufactured using a commercial silicone rubber material A while the 6 mm designs were cast using another silicone, material B. The main reason was the lack of availability for material A. However, the use of two different materials enabled the comparison between housing materials with different hydrophobicity properties.

Textured insulators were tested in clean-fog following the same procedures applied for conventional polymeric insulators testing. Textured showed an improvement of the flashover performance which could reach 26 %. The insulators made of 6mm designs that were made of material B, showed a lower improvement that ranged from 2 to 9 %. This reduced improvement of the 6 mm samples was attributed to the better hydrophobicity of material B compared with material A.

The textured shank and shed (TSS) design showed higher improvement of the flashover voltage compared to the textured shank (TS) design for the insulators made of material A. This was attributed to the longer creepage length achieved by the TSS design. For the textured prototypes made with material B, the texturing of the shed underside introduced little or no further improvement compared with the textured shank design. This was interpreted as the result of

the more hydrophobic material B that generally reduced the advantage introduced by surface texturing.

The test conditions of pollution severity and fog wetting rate were varied during the tests. The higher improvement of the flashover voltage was observed for heavy wetting and heavy pollution. This could suggest that surface texturing could be more beneficial for severe pollution conditions. Moreover, by comparing the performance for two different materials, it could be suggested that texturing may be more effective for conditions of temporary loss of hydrophobicity observed for silicone rubber insulators in service.

7.4 Future work

A large amount of data has been collected throughout the experimental investigations of this research programme. It includes current records, digital camera records and infrared camera records. Correlation of these data, especially for the case of textured insulators need to be performed as part of the ongoing research programme. This task will aim to identify a possible distinct behaviour of dry-bands for textured insulators compared with conventional insulators.

Ramp voltage tests need to be expanded to include a wider range of pollution severities. A modification of the standard ramp test, where the test sample is mounted at a horizontal position to investigate the effect of the insulator attitude, needs to be performed. Moreover, the High Voltage Energy Systems research group is currently investigating the effect of UV degradation to the performance of textured insulators using the weathering testing unit facilities.

Long-term performance of textured insulators will be investigated. The tracking wheel facilities in Cardiff University will be used to assess the ability of textured insulators to resist erosion and tracking. The fog chamber can also be modified to facilitate the 1000 h salt-fog test. Such tests will investigate whether the outstanding anti-erosion and anti-tracking performance of textured designs brought up during inclined-plane tests, will be observed for full textured insulators.

For all artificial testing of outdoor insulators, their ability to fully replicate service conditions is limited. The research programme could be extended to investigate the performance of textured insulators in field tests where the test objects will be subjected to service stresses. The information and results acquired from both the laboratory exploration and the field tests will be the basis of shaping a proposal for the commercial development and release of textured insulators for adverse environmental conditions.

References

[1.1] Looms, J.S.T., 'Insulators for high voltages', IEE Power Engineering Series, vol. 7, Peter Peregrinus Ltd., 1988, ISBN 9780863411168

[1.2] Swift, D.A., Insulators for outdoor applications, in Advances in high voltage engineering, A. Haddad and D. Warne, Editors. 2004, ISBN 0852961588

[1.3] CIGRE Task Force 33.04.01, 'Polluted Insulators: A review of current knowledge', 2000

[1.4] CIGRE C4.303, 'Outdoor insulation in polluted conditions: Guidlines for selection and dimensioning part 1: General principles and the AC case', 2008

[1.5] IEC 60815:2008, 'Selection and dimensioning of high-voltage insulators intended for use in polluted conditions_Part 1: Definitions, information and general principles', 2008

[1.6] IEC 60507:1991, 'Artificial pollution tests on high-voltage insulators to be used on a.c. systems', 1991

[1.7] Williams, D.L., Haddad, A., Rowlands, A.R., Young, H.M., and Waters, R.T., 'Formation and characterization of dry bands in clean fog on polluted insulators', IEEE Trans. Dielectr. Electr. Insul., Vol. 6, (5): pp. 724-731, 1999

[1.8] Haddad, A. and Waters, R.T., Insulating Structures, UK Patent 2406225, 2003

[1.9] Haddad, A., Waters, R., Griffiths, H., Chrzan, K., Harid, N., Sarkar, P., and Charalampidis, P., 'A new approach to anti-fog design for polymeric insulators', IEEE Trans. Dielectr. Electr. Insul., Vol. 17, (2): pp. 343-350, 2010

[1.10] IEC 60587:2007, 'Electrical insulating materials used under severe ambient conditions. Test methods for evaluating resistance to tracking and erosion', 2007

[2.1] Gubanski, S.M., 'Modern outdoor insulation - concerns and challenges', IEEE Electr. Insul. Mag., Vol. 21, (6): pp. 5-11, 2005

[2.2] Lambeth, P.J., 'Effect of pollution on high-voltage outdoor insulators', Proceedings of the Institution of Electrical Engineers, Vol. 118, (9): pp. 1107-1130, 1971

[2.3] Schneider, H.M., Hall, J.F., Karady, G., and Renowden, J., 'Nonceramic insulators for transmission lines', IEEE Trans. Power Del., Vol. 4, (4): pp. 2214-2221, 1989

[2.4] Seifert, J.M. and Stefanini, D., 'High Pollution Resistant Composite Insulators', International Conference on High Voltage Engineering and Application (ICHVE), pp. 32-35, Chongqing, China, 2008

[2.5] Amin, M., Akbar, M., and Khan, M.N., 'Aging Investigations of Polymeric Insulators: Overview and Bibliography', IEEE Electr. Insul. Mag., Vol. 23, (4): pp. 44-50, 2007

[2.6] Spellman, C.A., Young, H.M., Haddad, A., Rowlands, A.R., and Waters, R.T., 'Survey of polymeric insulator ageing factors', XI International Symposium on High Voltage Engineering (ISH), Vol. 4, pp. 160-163 vol.4, London, UK, 1999

[2.7] Reynders, J.P., Jandrell, I.R., and Reynders, S.M., 'Review of aging and recovery of silicone rubber insulation for outdoor use', IEEE Trans. Dielectr. Electr. Insul., Vol. 6, (5): pp. 620-631, 1999

[2.8] Hackam, R., 'Outdoor HV composite polymeric insulators', IEEE Trans. Dielectr. Electr. Insul., Vol. 6, (5): pp. 557-585, 1999

[2.9] Vlastos, A.E. and Gubanski, S.M., 'Surface structural changes of naturally aged silicone and EPDM composite insulators', IEEE Trans. Power Del., Vol. 6, (2): pp. 888-900, 1991

[2.10] Gorur, R.S., Chang, J.W., and Amburgey, O.G., 'Surface hydrophobicity of polymers used for outdoor insulation', IEEE Trans. Power Del., Vol. 5, (4): pp. 1923-1933, 1990

[2.11] Cherney, E.A. and Gorur, R.S., 'RTV silicone rubber coatings for outdoor insulators', IEEE Trans. Dielectr. Electr. Insul., Vol. 6, (5): pp. 605-611, 1999

[2.12] Wang, S., Liang, X., Guan, Z., and Wang, X., 'Hydrophobicity transfer properties of silicone rubber contaminated by different kinds of pollutants', Annual Report Conference on Electrical Insulation and

Dielectric Phenomena (CEIDP), Vol. 1, pp. 373-376 vol.1, Victoria, Canada, 2000

[2.13] Swift, D.A., Spellman, C., and Haddad, A., 'Hydrophobicity transfer from silicone rubber to adhering pollutants and its effect on insulator performance', IEEE Trans. Dielectr. Electr. Insul., Vol. 13, (4): pp. 820-829, 2006

[2.14] Loberg, J.O. and Salthouse, E.C., 'Dry-Band Growth on Polluted Insulation', IEEE Trans. Electr. Insul., Vol. EI-6, (3): pp. 136-141, 1971

[2.15] Salthouse, E.C., 'Initiation of dry bands on polluted insulation', Proceedings of the Institution of Electrical Engineers, Vol. 115, (11): pp. 1707-1712, 1968

[2.16] Hampton, B.F., 'Flashover mechanism of polluted insulation', Electrical Engineers, Proceedings of the Institution of, Vol. 111, (5): pp. 985-990, 1964

[2.17] Texier, C. and Kouadri, B., 'Model of the formation of a dry band on an NaCl-polluted insulation', IEE Proceedings A, Physical Science, Measurement and Instrumentation, Management and Education - Reviews, Vol. 133, (5): pp. 285-290, 1986

[2.18] Williams, D.L., 'Insulation failure mechanisms in artificial pollution tests', School of Engineering, PhD, 1997

[2.19] Williams, D.L., Haddad, A., Rowlands, A.R., Young, H.M., and Waters, R.T., 'Formation and characterization of dry bands in clean fog on polluted insulators', IEEE Trans. Dielectr. Electr. Insul., Vol. 6, (5): pp. 724-731, 1999

[2.20] Waters, R.T., Haddad, A., Griffiths, H., Harid, N., and Sarkar, P., 'Partial-arc and spark models of the flashover of lightly polluted insulators', IEEE Trans. Dielectr. Electr. Insul., Vol. 17, (2): pp. 417-424, 2010

[2.21] Rizk, F.A.M., 'Mathematical models for pollution flashover', Electra, Vol. 28: pp. 71-103, 1981

[2.22] Claverie, P., 'Predetermination of the Behaviour of Polluted Insulators', IEEE Trans. Power App. Syst., Vol. PAS-90, (4): pp. 1902-1908, 1971

[2.23] Waters, R.T., Haddad, A., Griffiths, H., Harid, N., Charalampidis, P., and Sarkar, P., 'Dry-band discharges on polluted silicone rubber insulation: control and characterization', IEEE Trans. Dielectr. Electr. Insul., Vol. 18, (6): pp. 1995-2003, 2011

[2.24] Karady, G.G., 'Flashover mechanism of non-ceramic insulators', IEEE Trans. Dielectr. Electr. Insul., Vol. 6, (5): pp. 718-723, 1999

[2.25] Swift, D.A., 'Flashover of an insulator surface in air due to polluted water droplets', Proceedings of the 4th International Conference on Properties and Applications of Dielectric Materials, Vol. 2, pp. 550-553 vol.2, Brisbane, Australia, 1994

[2.26] Karady, G.G., Shah, M., and Brown, R.L., 'Flashover mechanism of silicone rubber insulators used for outdoor insulation-I', IEEE Trans. Power Del., Vol. 10, (4): pp. 1965-1971, 1995

[2.27] Shah, M., Karady, G.G., and Brown, R.L., 'Flashover mechanism of silicone rubber insulators used for outdoor insulation-II', IEEE Trans. Power Del., Vol. 10, (4): pp. 1972-1978, 1995

[2.28] CIGRE Task Force 33.04.07, 'Natural and artificial ageing and pollution testing of polymeric insulators', 1999

[2.29] Gutman, I. and Dernfalk, A., 'Pollution tests for polymeric insulators made of hydrophobicity transfer materials', IEEE Trans. Dielectr. Electr. Insul., Vol. 17, (2): pp. 384-393, 2010

[2.30] De La O, A., Gorur, R.S., and Chang, J., 'AC clean fog tests on nonceramic insulating materials and a comparison with porcelain', IEEE Trans. Power Del., Vol. 9, (4): pp. 2000-2008, 1994

[2.31] Bingbing, D., Xingliang, J., Jianlin, H., Lichun, S., and Caixin, S., 'Effects of artificial polluting methods on AC flashover voltage of composite insulators', IEEE Trans. Dielectr. Electr. Insul., Vol. 19, (2): pp. 714-722, 2012

[2.32] Gutman, I., Kondo, K., Matsuoka, R., and Garcia, R.W., 'CIGRE round robin pollution test for polymeric insulators: results in four high-voltage laboratories', XVII International Symposium on High Voltage Engineering (ISH), Hannover, Germany, 2011

[2.33] Baharom, M.N.R. and Cotton, I., 'Inclined plane tests of composite, silicone rubber and composite silicone rubber coated materials', XVI International Symposium on High Voltage Engineering (ISH), Johannesburg, South Africa, 2009

[2.34] Meyer, L.H., Jayaram, S.H., and Cherney, E.A., 'Correlation of damage, dry band arcing energy, and temperature in inclined plane testing of silicone rubber for outdoor insulation', IEEE Trans. Dielectr. Electr. Insul., Vol. 11, (3): pp. 424-432, 2004

[2.35] Bruce, G.P., Rowland, S.M., and Krivda, A., 'Performance of silicone rubber in DC inclined plane tracking tests', IEEE Trans. Dielectr. Electr. Insul., Vol. 17, (2): pp. 521-532, 2010

[2.36] Heger, G., Vermeulen, H.J., and Vosloo, W.L., 'Evaluation of the performance of HTV silicone rubber exposed to AC & DC surface discharging using the incline plane test', XVI International Symposium on High Voltage Engineering (ISH), Johannesburg, South Africa, 2009

[2.37] Heger, G., Vermeulen, H.J., Holtzhausen, J.P., and Vosloo, W.L., 'A comparative study of insulator materials exposed to high voltage AC and DC surface discharges', IEEE Trans. Dielectr. Electr. Insul., Vol. 17, (2): pp. 513-520, 2010

[2.38] Crespo-Sandoval, J., 'Condition monitoring of outdoor insulation using artificial intelligence techniques', Cardiff University, PhD, 2005

[2.39] Schmidt, L.E., Kornmann, X., Krivda, A., and Hillborg, H., 'Tracking and erosion resistance of high temperature vulcanizing ATH-free silicone rubber', IEEE Trans. Dielectr. Electr. Insul., Vol. 17, (2): pp. 533-540, 2010

[2.40] Krivda, A., Schmidt, L., Kornmann, X., Ghorbani, H., Ghorbandaeipour, A., Eriksson, M., and Hillborg, H., 'Inclined-plane tracking and erosion test according to the IEC 60587 Standard', IEEE Electr. Insul. Mag., Vol. 25, (6): pp. 14-22, 2009

[2.41] IEC 62217:2006, 'Polymeric insulators for indoor and outdoor use with a nominal voltage > 1000 V - General definitions, test methods and acceptance criteria', 2006

[2.42] Muncivi, A., Sarkar, P., and Haddad, A., 'Tracking wheel test facilities', Proceedings of the 44th International Universities Power Engineering Conference (UPEC), pp. 1-5, Glasgow, UK, 2009

[2.43] Bologna, F., Mahatho, N., and Hoch, D.A., 'Infra-red and ultra-violet imaging techniques applied to the inspection of outdoor transmission voltage insulators', 6th IEEE AFRICON, Vol. 2, pp. 593-598, George, South Africa, 2002

[2.44] Garcia, R.W.S., Mello, D.R., Paiva, O.L.S., E.G., C., and Ferreira, L.F.P., 'Development of methodology for monitoring composite insulators in service', XVI International Confrerence on High Voltage Engineering (ISH), Johannesburg, South Africa, 2009

[2.45] da Costa, E.G., Ferreira, T.V., Neri, M.G.G., Queiroz, I.B., and Germano, A.D., 'Characterization of polymeric insulators using thermal and UV imaging under laboratory conditions', IEEE Trans. Dielectr. Electr. Insul., Vol. 16, (4): pp. 985-992, 2009

[2.46] Ferreira, T.V., Germano, A.D., da Costa, E.G., Angelini, J.M.G., Nallim, F.E., and Mendonca, P., 'Naturally aged polymeric insulators: Washing and its consequences', Proceedings of the International Symposium Modern Electric Power Systems (MEPS), pp. 1-5, Wroclaw, Poland, 2010

[2.47] Cho, H.G., Lee, U.Y., Han, S.W., Cheon, J.U., and Lim, K.J., 'The Performance of Tracking Aging and Surface in Polymer Insulator', International Conference in Electrical Engineering (ICEE), Korea, 2002

[2.48] Sarkar, P., Haddad, A., Waters, R.T., Griffiths, H., Harid, N., and Charalampidis, P., 'Inclined-plane tests of textured silicone rubber Samples', International Conference on High Voltage Engineering and Application (ICHVE), pp. 532-535, New Orleans, U.S.A., 2010

[2.49] Charalampidis, P., Haddad, A., Waters, R.T., Griffiths, H., Harid, N., and Sarkar, P., 'Five-electrode inclined-plane tests of textured silicone rubber samples', 45th Universities Power Engineering Conference (UPEC), pp. 1-5, Cardiff, UK, 2010

[2.50] Charalampidis, P., Albano, M., Waters, R.T., Haddad, A., Griffiths, H., and Harid, N., 'Dry-band discharges on silicone rubber insulation', XVII International Conference on High Voltage Engineering (ISH), Hannover, Germany, 2011

[2.51] IEC 60815:2008, 'Selection and dimensioning of high-voltage insulators intended for use in polluted conditions_Part 3 Polymer insulators for a.c. systems', 2008

Appendix – Supplementary information for silicone rubber samples and insulators casting.

A.1 Preparation of the mould and the insulator cores

The metal moulds were made of steel and machined using electrical discharge machining (EDM) techniques. The mould consisted of two steel plates, each containing slots to receive metal inserts that would form the desired moulding cavity. Each insert and slot is noted with a capital letter or symbol to ensure each insert is mounted on the right position (Figure A-1).

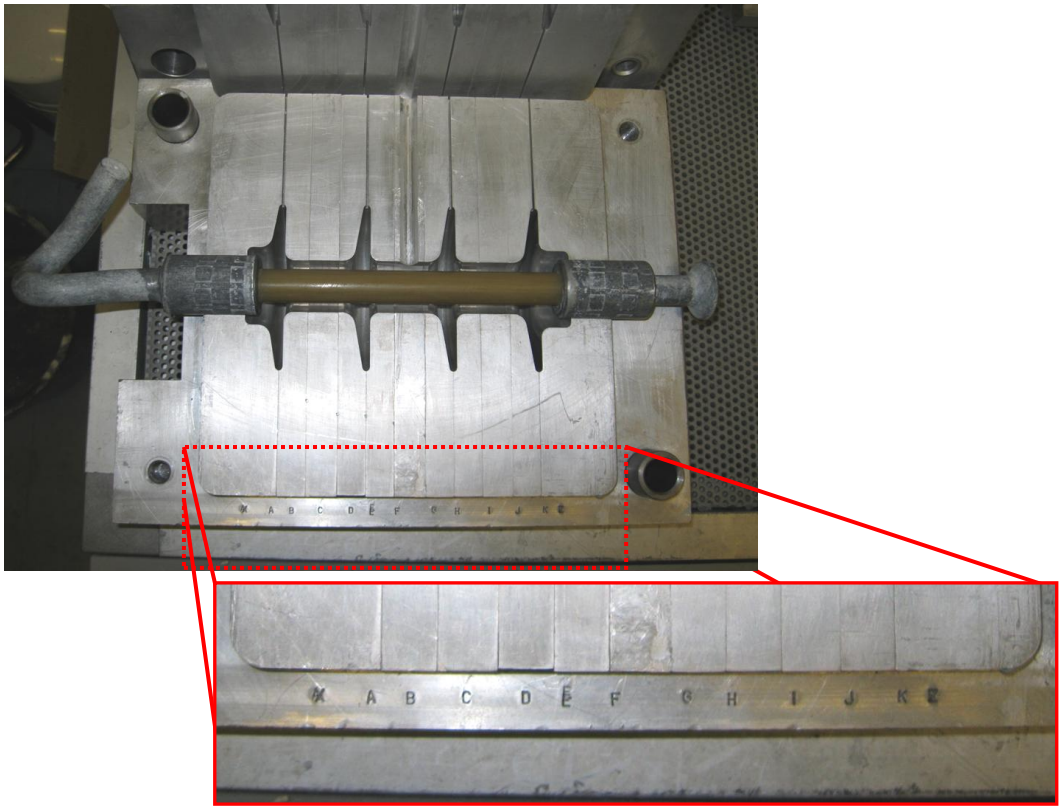

Figure A-1. The steel mould and the metal inserts .

The inserts are placed tightly next to each other with the help of a sledge hammer coated with rubber to avoid damaging the mould. The sides of the

inserts that are in contact are sometimes lubricated with a thin layer of grease to assist mounting.

A set of 'allen' bolts at the back of the mould plates secures the inserts in position. After the mould assembling is completed, it is thoroughly cleaned with propanol to remove any contaminants or grease in the mould cavity.

The core with the metal fittings was also thoroughly cleaned with propanol. Silicone rubber bonding with the core material and the metal terminals is poor. A special chemical primer was required to transform the bonding properties of the substrate surface. A commercial primer was used consisting of siloxanes and silicones resins in a mixture of isoalkanes. A very thin layer of this primer was applied using a brush on the surface where the silicone rubber would be overmoulded. Then it was left in room temperature for 2 hours. Casting should be performed not more than 5 hours from the primer drying. After the core is placed in position in the mould, the two plates are joined and sealed with the help of threaded rods and bolts.

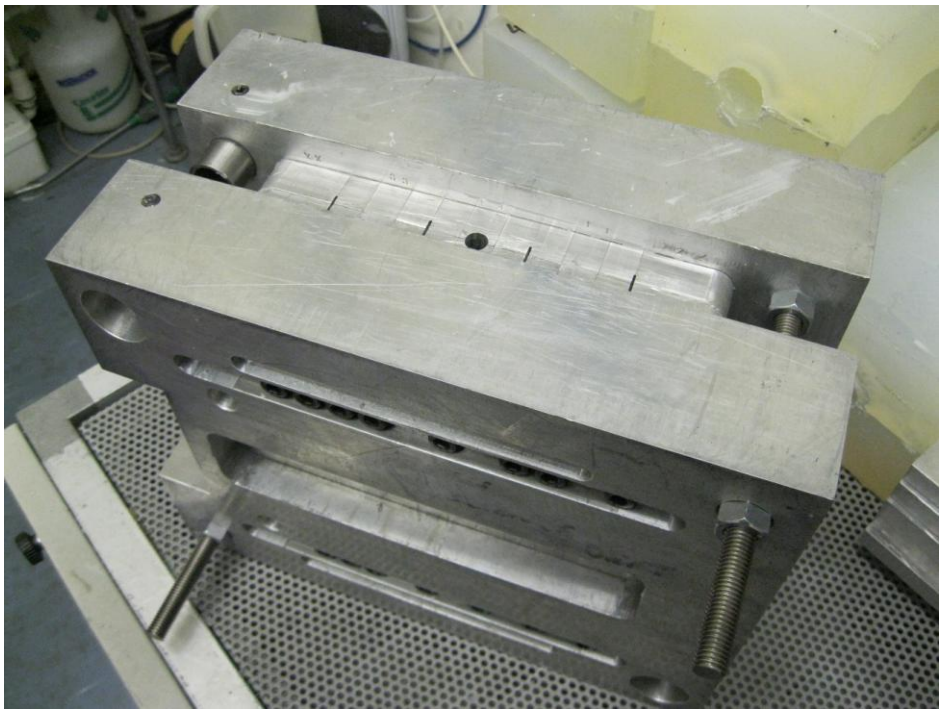

Figure A-2. The mould ready for casting.

A.2 Silicone rubber mixing

Commercial, two-component, silicone rubbers were used. Before using the base component, the material was stirred for 3-4 minutes as a prolonged storage of the base material might result in the fillers settling in the bottom of the storage vessel. Special care should be taken to avoid any contact of the base material in the storage vessel with the curative. For that reason, separate equipment should be used to handle the base and the curative.

The base (component A) and the curative (component B) were mixed at a ratio of 9:1. The mixing quantities should be measured carefully and accurately. Failure to do so might result to a poor-quality mould. The quantities used for each mould were as described below:

- Conventional full insulators and textured prototypes
  - 450g base
  - 50g curative
- Cylindrical prototypes
  - 270g base
  - 30g curative
- Rectangular non-textured and textured silicone rubber samples
  - 90 g base
  - 10 g curative